TECHNISCHE
UNIVERSITÄT
DRESDEN

Leibniz Institute
for Solid State and
Materials Research
Dresden

Symmetry-enriched topological states of matter in insulators and semimetals

Dissertation
zur Erlangung des akademischen Grades
Doctor rerum naturalium
(Dr. rer. nat.)

vorgelegt von

Dipl.-Phys. Alexander Lau

geboren am 17.07.1987
in Bernau bei Berlin, Deutschland

Fachrichtung Physik
Fakultät für Mathematik und Naturwissenschaften
Technische Universität Dresden
2017

Eingereicht am: 17. Oktober 2017
Verteidigt am: 7. März 2018

1. Gutachter: Prof. Dr. Jeroen van den Brink
2. Gutachter: Dr. Carmine Ortix

Contents

1 Background and motivation 1

2 Novel topological states in the dimerized Hofstadter model 4

2.1 Introduction 4

2.1.1 The quantum Hall effect 4

2.1.2 Chern numbers and topological invariants 8

2.1.3 The Hofstadter model 12

2.2 The dimerized Hofstadter model 16

2.3 One-dimensional Hofstadter slices with inversion symmetry 19

2.4 Topological invariant for one-dimensional systems 21

2.5 Dimerized Hofstadter models with rational flux 23

2.5.1 Hofstadter models with half-integer flux 23

2.5.2 Hofstadter models with odd-denominator fluxes 25

2.5.3 Generalization to arbitrary rational flux 29

2.6 Possible experimental realization and detection 30

3 One-dimensional Dirac electrons in weak topological insulators 33

3.1 Introduction 33

3.1.1 The quantum spin-Hall effect 33

3.1.2 The quantum spin-Hall insulator in two dimensions 36

3.1.3 Topological insulators in three dimensions 42

3.2 Dirac line degeneracies in topological insulators 45

3.3 In-plane time-reversal invariance 47

3.4 Stacked Kane-Mele model 49

3.5 Cubic Liu-Qi-Zhang model 53

3.6 Possible experimental detection 59

4 **Topological mirror insulators in one dimensions** **60**
4.1 Introduction 60
4.1.1 Topological crystalline insulators 60
4.1.2 Topological crystalline insulators with rotational symmetry 62
4.1.3 Mirror Chern number for systems with reflection symmetry 65
4.2 One-dimensional topological insulators 67
4.3 Invariant for topological mirror insulators in one dimension 68
4.3.1 Charge polarization and partial polarization 68
4.3.2 Quantization of the partial polarization 70
4.3.3 Topological invariant 71
4.3.4 Bulk-boundary correspondence: quantized end charges 72
4.4 Spin-orbit coupled Aubry-André-Harper models 73
4.4.1 Phase diagram and in-gap end states 74
4.4.2 Bulk-edge correspondence 76
4.4.3 Effect of disorder 78
4.5 Modulated semiconductor nanowires 80

5 **Weyl semimetals with time-reversal symmetry** **82**
5.1 Introduction 82
5.1.1 Weyl fermions as solutions of the Dirac equation 82
5.1.2 Weyl fermions in condensed matter: Weyl semimetals 84
5.1.3 Topological surface states: Fermi arcs 88
5.2 Coexistence of Fermi arcs and Dirac cones in Weyl semimetals 90
5.2.1 Topological invariants for time-reversal invariant Weyl semimetals . 90
5.2.2 Phenomenological quasiparticle-interference patterns 92
5.2.3 The coexistence in a tight-binding model formulation 96
5.2.4 Density-functional theory analysis of strained LaPtBi 101
5.3 Weyl semimetals from novel topological insulator multilayers 105
5.3.1 Balents-Burkov model for strong topological insulator multilayers . 106
5.3.2 Weak topological insulator multilayer 107
5.3.3 Topological crystalline insulator multilayer 113

6 **Outlook and conclusions** **118**

A Smooth gauge for one-dimensional systems 121

B Wannier-center formulation of the topological invariant 123

C Iterative scheme for the calculation of surface Green's functions 127

List of publications 131

Bibliography 135

Acknowledgements 151

Eidesstattliche Erklärung 152

List of abbreviations

1D	one-dimensional/one dimension
2D	two-dimensional/two dimension
2DEG	two-dimensional electron gas
3D	three-dimensional/three dimension
AAH	Aubry-André-Harper
ARPES	angle-resolved photoemission spectroscopy
BZ	Brillouin zone
IPR	inverse participation ratio
JDOS	joint density of states
LDOS	local density of states
OI	ordinary insulator
QAHE	quantum anomalous Hall effect
QHE	quantum Hall effect
QPI	quasiparticle interference
QSHE	quantum spin-Hall effect
QSHI	quantum spin-Hall insulator
SOC	spin-orbit coupling
SSH	Su-Schrieffer-Heeger
STI	strong topological insulator
STS	scanning tunneling spectroscopy
TCI	topological crystalline insulator
TI	topological insulator
TRI	time-reversal invariant
WSM	Weyl semimetal
WTI	weak topological insulator

1 Background and motivation

The study of the electronic and magnetic structure of solid states of matter is one of the driving forces of modern physics. It has led to astonishing discoveries, such as superconductivity or giant magnetoresistance, and has thereby triggered significant technological advances.

Solids are states of matter in which a large number of atoms or molecules are arranged in a regular spatial pattern often described in terms of a discrete lattice. Remarkably, the microscopic interactions between the many particles constituting a solid lead to properties that cannot be explained by considering the constituents individually. This so-called principle of emergence, i.e., the whole is more than the sum of its parts, is at the very basis of the various manifestations of solid phases of matter.

A common theme in solid-state physics is the search for new phases of matter. In this context, the celebrated Landau theory of phase transitions provides a powerful framework to identify and understand states of matter in terms of local order parameters and spontaneous symmetry breaking. However, the discovery of the quantum Hall effect and the Kosterlitz-Thouless phase transition, which were both awarded with the Nobel prize in physics, pushed the well-established theory to its limits. These phases elude Landau's paradigm since they do not spontaneously break any symmetry. Ultimately, these findings opened the door to a vast new realm of exotic phases fundamentally different from everything that was known before: *topological phases of matter*.

It is remarkable that these novel phases can be described using the language of the abstract mathematical field of topology, a field which is concerned with the properties of mathematical spaces that remain invariant under continuous deformations, such as bending and stretching, but not tearing or gluing. Simply speaking, in this sense, a coffee mug with a handle is topologically equivalent to a donut since both feature the same number of holes, where the latter is a so-called topological invariant. How is this connected to exotic phases of quantum matter? In solids, the space of interest is spanned by the large ensemble of electronic wave functions which can lead to a highly nontrivial object with unique mathematical and physical properties. A topological phase is characterized by a nonzero topological invariant associated with this object. In contrast to order parameters of conventional phases, this invariant is a global quantity and assumes only discrete values leading to a characteristic quantization of physical observables.

The study of topological phases of matter has brought to light a myriad of exceptional features and remarkable effects which have not only broadened our knowledge of matter in general but could also potentially lead to a whole new range of technologies and applications. Most notably, these features include topological surface states, giving rise to dissipationless charge transport, and exotic quasiparticles like Majorana modes, relevant for topological quantum computing. Hence, the study of topological states goes beyond pure scientific curiosity. In this light, it is paramount to find novel topological phases and to study their unique properties.

This dissertation aims at uncovering novel manifestations of topological states of matter as they arise when materials are subject to additional symmetries. Even though topological phases do not obey Landau's theory of phase transitions, symmetries can change the topological space of a system or impose restrictions on physical observables. This important insight has led to various classification tables of topological phases classifying systems according to their symmetries and dimensionality in a *general* way. Complementarily, this thesis focuses in more detail on *specific* classes and systems of topological phases to demonstrate how symmetries can enrich the topology of a system profoundly. More specifically, it is demonstrated how symmetries lead to additional nontrivial states in systems which are already topological, drive trivial systems into a topological phase, lead to the quantization of formerly non-quantized observables, and give rise to novel manifestations of topological surface states. In doing so, this work concentrates on weakly interacting systems that can theoretically be described in a single-particle picture. In particular, insulating and semimetalic topological phases in one, two, and three dimensions are discussed using single-particle techniques.

In more detail, the text is organized as follows: each chapter begins with an introductory part which lays the foundation for the main objective of each chapter. In Chapter 2, a brief introduction to the quantum Hall effect, the Chern number and topology in condensed matter physics is given. Furthermore, the famous Hofstadter model is introduced and it is shown that a lattice dimerization in this model leads to novel topological states which arise due to inversion symmetry in lower-dimensional subsystems. Chapter 3 introduces topological insulators with time-reversal symmetry. It is demonstrated that, for weak topological insulators in three dimensions, the presence of in-plane time-reversal symmetry leads to the emergence of topologically protected Dirac lines on the surface of the material.

Chapter 4 ventures into the realm of crystalline topological insulators. In particular, one-dimensional nanowires with both time-reversal and mirror symmetry are identified as a platform for novel topological states, dubbed topological mirror insulators, for which a new topological invariant is defined. In Chapter 5, Weyl semimetals are introduced as the most prominent example of topological semimetals. It is shown that time-reversal symmetry gives rise to a generic coexistence of Dirac states and Fermi arcs on the surface of Weyl semimetals. Moreover, a novel multilayer design for Weyl semimetals is presented based on layers of topological insulating materials with symmetries. Finally, Chapter 6 concludes the discussion of symmetry-enriched topological phases and offers an outlook towards promising prospects.

2 Topological edge states with zero Hall conductivity in a dimerized Hofstadter model

2.1 Introduction

2.1.1 The quantum Hall effect

The experimental discovery of the quantum Hall effect (QHE) by Klaus von Klitzing *et al.* in 1980 [1] represents the starting point of the very successful story of topology in condensed matter physics [2–4]. To understand the significance and the underlying physics of this effect let us first briefly review the *ordinary* Hall effect, which was discovered more than a century before by Edwin Hall [5].

The Hall effect describes the presence of a voltage, the so-called Hall voltage V_H, transverse to an electrical current in a thin-film conductor in the presence of a perpendicular magnetic field (see Fig. 2.1). The effect can be explained in the framework of classical electrodynamics [6]: due to the magnetic field $\mathbf{B} = B_z \mathbf{e}_z$, the charge carriers of the current with current density $\mathbf{j} = j_x \mathbf{e}_x$, which could be electrons, holes, or a combination of both, are deflected by the Lorentz force $\mathbf{F}_L = q(\mathbf{v} \times \mathbf{B})$. This leads to a buildup of charges and, hence, to an electric field $\mathbf{E} = E_y \mathbf{e}_y$ transverse to the current. In equilibrium, the force $\mathbf{F}_E = q\mathbf{E}$ corresponding to this field compensates the Lorentz force $\mathbf{F}_L$. For simplicity, let us assume that the current comprises purely electrons with $j_x = -env_x$, where n is the charge carrier density, and that the sample is a Hall bar of length l, width w, and height h (see Fig. 2.1). With these assumptions, we immediately see that the Hall resistance, which is defined as the Hall voltage $V_H = -E_y w$ divided by the current $I_x = j_x hw$, is related *linearly* to the applied magnetic field,

$$R_H \equiv R_{xy} = \frac{V_H}{I_x} = -\frac{1}{neh} B_z \equiv \frac{\mathcal{R}_H}{h} B_z, \tag{2.1}$$

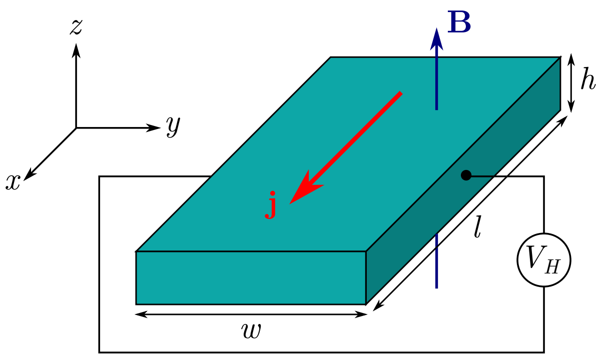

Figure 2.1: Hall bar with an electrical current **j** in the presence of a perpendicular magnetic field **B**.

where the Hall coefficient $\mathcal{R}_H = -1/ne$ is a material parameter. For hole currents the sign of $\mathcal{R}_H$ is simply reversed. For currents consisting of both electrons and holes, as is typically the case in semiconductors, a more complex expression, namely

$$\mathcal{R}_H = \frac{1}{e} \frac{p\mu_h^2 - n\mu_e^2}{(p\mu_h + n\mu_e)^2}, \tag{2.2}$$

can be derived [7], where p and n are the charge carrier densities of holes and electrons, respectively, and μ_h and μ_e are the corresponding charge carrier mobilities. These properties have made the ordinary Hall effect a widely used tool to access transport properties of conductors and to probe magnetic fields with high accuracy.

The classically derived formula for the Hall resistance reaches its limits once the quantum-mechanical nature of the charge carriers becomes relevant. This is the case for quasi two-dimensional Hall systems in the presence of a large magnetic field at sufficiently low temperatures [6,8]. This was first observed by Klaus von Klitzing *et al.* [1] in Hall measurements of two dimensional electron gases (2DEGs) formed at the interfaces of semiconductor heterostructures. For this discovery he was later awarded with the Nobel prize in physics. Klitzing found out that at large magnetic fields the linear field dependence of the Hall resistance evolves into steps with well-defined plateaus (see Fig. 2.2). Most remarkably, at these plateaus the Hall resistance is precisely quantized with

$$R_H = \frac{1}{\nu} \frac{h}{e^2}, \tag{2.3}$$

while the longitudinal resistance R_{xx} vanishes indicating dissipationless charge transport in the longitudinal direction. Moreover, the constant ν is an integer, which is why this

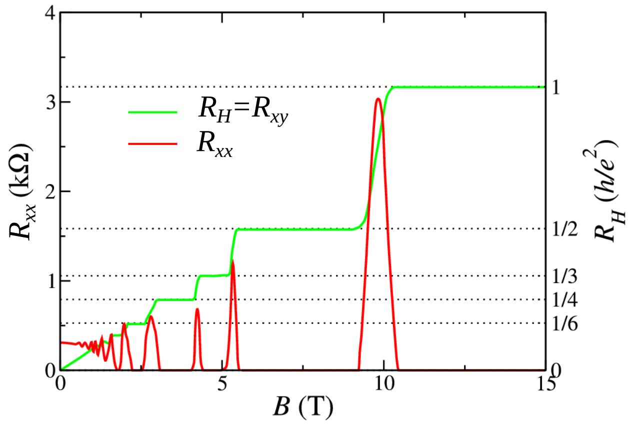

Figure 2.2: Hall resistance R_H and longitudinal resistance R_{xx} of a two-dimensional electron gas (2DEG) as a function of the magnetic field B [12]. Note that R_H features discrete plateaus at which the longitudinal resistance vanishes.

type of Hall effect is dubbed *integer* quantum Hall effect[1].

The origin of the QHE can be understood by treating the 2DEG in a magnetic field quantum-mechanically [6]. The electronic bands of typical semiconductors have a parabolic dispersion near the Fermi level. Thus, we can approximate our system of interest by a free non-relativistic electron gas with renormalized effective mass[2] m^*. Let us further assume a magnetic field $\mathbf{B} = B\mathbf{e}_z$ perpendicular to the 2DEG in the xy plane, and let us choose a gauge in which the electromagnetic vector potential[3] is $\mathbf{A} = Bx\mathbf{e}_y$. By coupling the electromagnetic field minimally to the momentum of the electrons, the one-particle Hamiltonian of our 2DEG becomes

$$\hat{H} = \frac{\hbar}{2m^*}\,(\hat{\mathbf{p}} - q\hat{\mathbf{A}})^2 = \frac{\hbar}{2m^*}\,\hat{p}_x^2 + \frac{\hbar}{2m^*}\,(\hat{p}_y - qB\hat{x})^2. \tag{2.4}$$

Obviously, the Hamiltonian commutes with $\hat{p}_y$. Therefore, energy eigenstates can be chosen to be eigenstates of $\hat{p}_y$, and we can replace $\hat{p}_y$ in $\hat{H}$ by its eigenvalues $\hbar k_y$ in this gauge. Furthermore, we introduce the cyclotron frequency $\omega_c = q\hbar B/m^*$. With this, our

---

[1] Note that there exists also a *fractional* variant of the QHE for which ν can assume certain values in a sequence of rational numbers. The discovery of the fractional QHE was also awarded with the Nobel prize in physics and is still subject of intense research [9, 10]. In particular, the fractional-QHE phase gives rise to anyonic quasi-particle excitations with non-Abelian statistics which could potentially be used to perform quantum computations [11].

[2] An important exception is for instance graphene whose electrons obey an effective *massless* Dirac equation [13]. A careful treatment of this case leads to other interesting features such as the zeroth Landau level.

[3] We could of course take any other gauge choice for $\mathbf{A}$ as $\mathbf{B} = \nabla \times \mathbf{A}$.

Hamiltonian becomes

$$\hat{H} = \frac{\hbar}{2m^*}\hat{p}_x^2 + \frac{1}{2}m\omega_c\left(\hat{x} - \frac{\hbar^2 k_y}{m^*\omega_c}\right)^2. \tag{2.5}$$

This is the Hamiltonian of a quantum harmonic oscillator with a potential shifted by $\hbar^2 k_y/m^*\omega_c$. The eigenvalues of this Hamiltonian are well-known. Hence, the energies of our system are

$$E_{nk_y} = \hbar\omega_c\left(n + \frac{1}{2}\right), \quad n \in \mathbb{N}_0. \tag{2.6}$$

As we can easily see, for fixed n each so-called Landau level is highly degenerate because the quantum number k_y does not appear in the expression for the energies. More specifically, the number of states per Landau level depends, among others[4], on the magnetic field

For small magnetic fields, the degeneracy per Landau level is small and many levels will be occupied. Furthermore, depending on the field, the occupation of the highest Landau level n_{max} can range from completely filled to entirely empty. This gives rise to characteristic quantum oscillations, such as the de Haas-van Alphen effect.

With increasing magnetic field, each Landau level can accommodate more and more electrons thereby reducing n_{max} step-wise until all electrons fit in only a few highly degenerate Landau levels. This is the regime where the QHE is observed. A plateau in the Hall resistance corresponds to a situation in which the Fermi level of the quantum-Hall system lies in between two neighboring Landau levels. A step in the Hall resistance occurs whenever the Fermi level crosses one of the Landau levels and the number of occupied Landau levels, thus, changes by one.

The sharp quantization was finally explained theoretically by Thouless *et al.* who where able to connect the Hall conductance in the QHE, which is the inverse of the Hall resistance, to the *topology* of the occupied Landau levels [14, 15]. In particular, they proved that the Hall conductance is equal to the sum of the *Chern numbers* of all occupied bands in units of e^2/h. The Chern number, as we will elaborate in the next section, is a topological invariant characterizing the electronic band structure of a band insulator and can only assume integer values [16]. If the Fermi level is in between two Landau levels, the corresponding quantum-Hall system can indeed be considered as a band insulator. In particular, each Landau level has a nontrivial Chern number of $\nu_n = 1$. This immediately explains the quantization of the Hall resistance. Hence, the integer in Eq. (2.3) is simply $\nu = \sum_{n=1}^{n_{\text{max}}} \nu_n$.

Another consequence of the nontrivial topology of the Landau levels is the presence of topologically protected chiral edge states propagating along the boundary of the quantum-

---

[4] For a 2DEG sample of area A the degeneracy of each Landau level can be approximated by BAe/h [6].

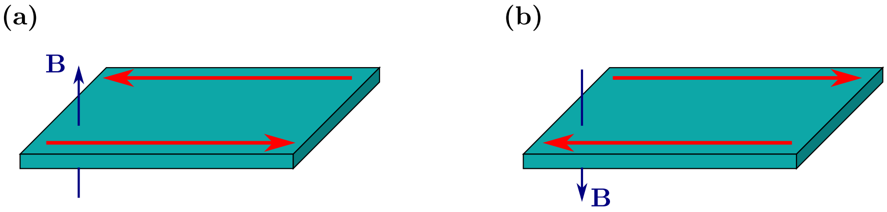

Figure 2.3: Chiral edge states propagating along the boundary of a QHE sample. The direction of propagation is indicated by red arrows. Note how the chirality depends on the direction of the magnetic field **B**.

Hall sample [8](see Fig. 2.3). The chirality of the edge channels depends on the direction of the magnetic field. Moreover, for a Hall conductance of ν (in units of e^2/h) there are ν quasi-1D edge channels confined to each edge of the sample. Remarkably, these states are immune to backscattering because the backward-scattering channels are always confined to the opposite edge. In this way, electrons can propagate along the edges of the sample without dissipation. The topological edge states are also at the basis of the vanishing longitudinal resistance R_{xx} [17, 18].

The presence of dissipationless chiral edge states makes quantum-Hall systems promising candidates for novel electronic devices with low power consumption. However, their existence is bound to the presence of well-defined and well-separated Landau levels, which typically[5], requires low temperatures large magnetic fields, and samples with high charge carrier mobility[6] [8]. A possible way out is provided by the quantum anomalous Hall effect (QAHE), which describes a QHE in the absence of a magnetic field. A theoretical model realizing this effect was first introduced by Haldane [21]. Experimentally, the QAHE has been realized at the interface between a ferromagnet and a strong topological insulator [8, 22–24].

2.1.2 Chern numbers and topological invariants

Let us now have a closer look into the topological invariant that characterizes the QHE. As we have seen in the previous section, each Landau level can be assigned a quantized number, which naturally leads to the quantization of the Hall conductance. This number is known as the first Chern number of the electronic band.

---

[5] The conditions of the QHE can be relaxed in some materials. In graphene, for instance, the QHE has been observed at room temperature [19] and at magnetic fields below 1 T [20], owing to the unusual nature of its charge carriers which behave as massless relativistic particles.

[6] At finite temperatures, thermal fluctuations broaden the Landau levels and eventually lead to an overlap of neighboring levels and a break-down of the energy gap. Therefore, the temperature T needs to be sufficiently low such that all Landau levels are well separated. Therefore, the Landau level spacing should be as large as possible. Since their spacing $\hbar\omega_c$ is proportional to B/m^*, the magnetic field and the charge carrier mobility $\mu \sim 1/m^*$ should be high.

The Chern number is a quantity borrowed from the abstract mathematical field of topology, which is concerned with the properties of topological spaces that are invariant under continuous deformations [25]. A prototypical example is the famous dichotomy of a torus and a sphere in two dimensions: it is impossible to find a continuous deformation that transforms one into the other.

For illustrational purposes, let us however have a look at a different example: let us consider closed curves, or loops, in the two dimensional plane without the origin [25], i.e., loops in the space $\mathbb{R}^2\backslash\{0\}$. From the viewpoint of continuous deformations, it is obvious that not all loops can be transformed into each other. In particular, a loop surrounding the origin cannot be deformed into a loop that does not contain the origin. In this way, the set of all loops decomposes into a set of equivalence classes according to how many times the loops "wind" around the origin [see Fig. 2.4(a)]. Interestingly, it is even possible to define a group operation on these equivalence classes. With this operation, the group of equivalence classes of loops defines the *first homotopy group* of the space $\mathbb{R}^2\backslash\{0\}$. Moreover, this group is homomorphically equivalent to the integer numbers, which is typically denoted by $\pi_1(\mathbb{R}^2\backslash\{0\}) = \mathbb{Z}$. The winding number of a loop, which is a $\mathbb{Z}$ number, is the natural topological invariant that characterizes a loop in a given equivalence class.

A loop is typically parameterized by a periodic parameter, say k. In this way, a loop can be viewed as a mapping from the circle $\mathcal{S}^1$ to the considered space $\mathcal{M}$, and the homotopy group $\pi_1(\mathcal{M})$ tells us what the nature of the corresponding topological invariant is. In general, the space $\mathcal{M}$ does not need to be a geometrical object. In particular, we could take the space of all single-particle Hamiltonians in one dimension with certain symmetries, and exclude all the Hamiltonians with a degeneracy (or gap closing point) in their energy spectrum. This is where we are going to build the bridge from abstract mathematics to physics [3, 26–28]: a lattice-periodic condensed matter system is typically described in terms of its Bloch Hamiltonian $H(k)$. Since the Brillouin zone (BZ) in one dimension is equivalent to a circle $\mathcal{S}^1$, any such system with an energy gap represents a loop in the space of Hamiltonians $\mathcal{M}_H$ as defined above. In this way, all the notions of topology, such as winding numbers or homotopy groups, can directly be carried over to physical systems. Furthermore, note that this scheme can be generalized to arbitrary dimensions [25–28].

Two topologically distinct systems can only be connected by "leaving" the underlying space, i.e., by crossing a gap closing point or by breaking the symmetry. This property is at the basis of the so-called bulk-boundary correspondence of topological systems [3]: at the

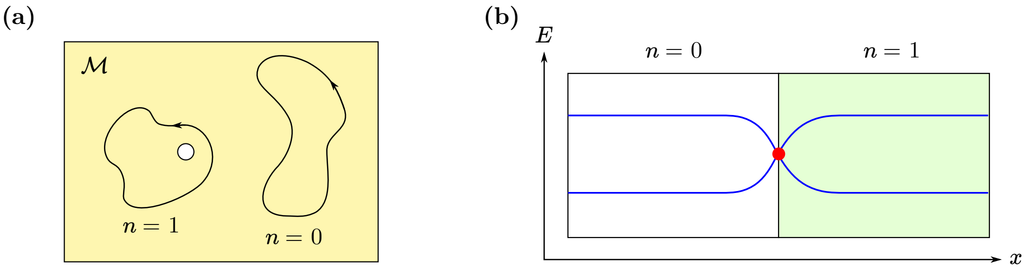

Figure 2.4: (a) Two distinct loops in a topological space $\mathcal{M}$ with a hole (e.g. $\mathbb{R}^2 \backslash \{0\}$ or a space of Hamiltonians $\mathcal{M}_H$): the loops are characterized by their winding number n which defines a topological invariant. (b) Bulk-boundary correspondence for two physical systems with different topology: the topological invariant n can only change if the energy gap (blue lines) is closed. This leads to a state (red dot) bound to the interface of the two phases.

boundary between two phases with different topology the bulk energy gap must close. In general, this leads to bound states crossing the Fermi level that are exponentially confined to the interface between the two phases (see Fig. 2.4). In particular, since the vacuum is topologically trivial, materials with nontrival topology will generically have conducting surface states whose presence is *topologically* protected.

With this in mind, let us go back to the quantum-Hall systems. Each Landau level represents a fully filled energy band of a two-dimensional system. In general, the (magnetic) BZ of such a system is equivalent to a two-dimensional torus $\mathbb{T}^2$, i.e., the set of all $H(\mathbf{k})$ parameterized by $\mathbf{k} \in \mathbb{T}^2$ forms a closed two-dimensional manifold in the space of gapped Hamiltonians $\mathcal{M}_H$ [6]. As before, this gives rise to equivalence classes of gapped systems. Systems in different classes have different topology and can only be connected by closing the energy gap. In this particular case, the topological invariant characterizing these systems is the *first Chern number* ν [6]. For a single band, it is defined as

$$\nu = \frac{1}{2\pi} \int_{\mathrm{BZ}} d^2k \, F_{xy}(\mathbf{k}), \tag{2.7}$$

with the Berry curvature

$$F_{xy}(\mathbf{k}) = [\nabla \times \mathbf{A}]_z = \partial_{k_x} A_y(\mathbf{k}) - \partial_{k_y} A_x(\mathbf{k}), \tag{2.8}$$

and the Berry vector potential $\mathbf{A} = (A_x, A_y, 0)$ defined as

$$A_j(\mathbf{k}) = i\langle u_{\mathbf{k}} | \partial_{k_j} | u_{\mathbf{k}} \rangle. \tag{2.9}$$

In the last equation, $u_{\mathbf{k}}(\mathbf{r})$ is the lattice-periodic part of a Bloch eigenstate $\psi_{\mathbf{k}}(\mathbf{r}) = e^{i\mathbf{k}\cdot\mathbf{r}}u_{\mathbf{k}}(\mathbf{r})$. Note that $\mathbf{A}(\mathbf{k})$ has an additional gauge freedom because a transformation of the form $\mathbf{A} \to \mathbf{A} + \nabla\chi$ does not change the value of the Chern number ν. For several isolated bands the net Chern number is simply the sum of the individual Chern numbers. If there are band crossings between the occupied bands, one can apply a weak perturbation to lift the band crossings. By continuity, the sum of the Chern numbers of the resulting bands must be equal to the net Chern number of the original system. Alternatively, one can use the non-Abelian Berry-curvature formulation of the Chern number to treat the multiplets [29].

The integral in Eq. (2.7) can only assume integer values [16]. Moreover, note that its value is always equal to zero if F_{xy} is a continuous function. In that case, we can apply Stokes' theorem and obtain

$$\int_{\mathrm{BZ}} d^2k\, F_{xy} = \int_{\mathrm{BZ}} d\mathbf{S}\cdot(\nabla\times\mathbf{A}) = \int_{\partial(\mathrm{BZ})} d\mathbf{r}\cdot\mathbf{A} = 0, \tag{2.10}$$

because the BZ does not have a boundary. A nontrivial value of the Chern number therefore indicates that it is impossible to find a gauge in which the Berry potential $\mathbf{A}(\mathbf{k})$ is a continuous function in the entire BZ [16]. In such a case, $\mathbf{A}$ can only be defined continuously “piecewiese”, i.e., in subsets or patches of the BZ. These patches define a covering of the BZ, where the definitions of $\mathbf{A}$ differ from patch to patch. Since $\mathbf{A}$ is continuous in each patch, Stokes' theorem can be applied to each patch separately and the integral in Eq. (2.7) becomes a sum of line integrals over the boundaries between the patches. Finally, the nonvanishing line integrals give rise to a nontrivial Chern number.

For numerical calculations, which typically yield eigenstates with random phases, it is helpful to find a gauge-invariant formulation of the Chern number. For a system described by a Bloch Hamiltonian $H(\mathbf{k})$ with energies $E_{n\mathbf{k}}$ and eigenstates $u_{n\mathbf{k}}$, the Chern number of the nth band can be computed as [16],

$$\nu_n = -\frac{i}{2\pi}\int_{\mathrm{BZ}} d^2k \sum_{m\neq n} \frac{\langle u_{n\mathbf{k}}|\partial_{k_x}H(\mathbf{k})|u_{m\mathbf{k}}\rangle\langle u_{m\mathbf{k}}|\partial_{k_y}H(\mathbf{k})|u_{n\mathbf{k}}\rangle - (n \longleftrightarrow m)}{(E_{n\mathbf{k}} - E_{m\mathbf{k}})^2} \tag{2.11}$$

This formula is apparently gauge-independent and can be applied to any isolated band of the system.

As we will later see, the concepts used in this section can be applied to a whole range of physical systems. In particular, depending on the dimensionality and the symmetries of the systems under consideration, different topological classes and invariants are possi-

AZ class	Θ^2	C^2	S^2	$d=0$	$d=1$	$d=2$	$d=3$	$d=4$
A	0	0	0	$\mathbb{Z}$	0	$\mathbb{Z}$	0	$\mathbb{Z}$
AIII	0	0	1	0	$\mathbb{Z}$	0	$\mathbb{Z}$	0
AI	+1	0	0	$\mathbb{Z}$	0	0	0	$2\mathbb{Z}$
BDI	+1	+1	1	$\mathbb{Z}_2$	$\mathbb{Z}$	0	0	0
D	0	+1	0	$\mathbb{Z}_2$	$\mathbb{Z}_2$	$\mathbb{Z}$	0	0
DIII	-1	+1	1	0	$\mathbb{Z}_2$	$\mathbb{Z}_2$	$\mathbb{Z}$	0
AII	-1	0	0	$2\mathbb{Z}$	0	$\mathbb{Z}_2$	$\mathbb{Z}_2$	$\mathbb{Z}$
CII	-1	-1	1	0	$2\mathbb{Z}$	0	$\mathbb{Z}_2$	$\mathbb{Z}_2$
C	0	-1	0	0	0	$2\mathbb{Z}$	0	$\mathbb{Z}_2$
CI	+1	-1	1	0	0	0	$2\mathbb{Z}$	0

Figure 2.5: Altland-Zirnbauer classification of topological insulators and topological superconductors: the table lists all symmetry classes of gapped fermionic single-particle systems and the nature of their topological invariant (0, $\mathbb{Z}$, $2\mathbb{Z}$, or $\mathbb{Z}_2$) subject to their symmetries and their dimension d. The considered symmetries are time-reversal symmetry Θ, particle-hole symmetry C, and chiral symmetry S.

ble. This led to the famous Altland-Zirnbauer classification of topological insulators and superconductors[7] [26–28, 30–34], which is shown in Fig. 2.5. Taking into account only the generic, non-spatial symmetries, which are time-reversal, particle-hole and chiral symmetry, there are in total ten different classes differing in whether a symmetry is present and whether the corresponding operator squares to $+1$ or -1. It was found that in each dimension there are five symmetry classes which allow for topologically nontrivial systems characterized by topological invariants in $\mathbb{Z}$, $2\mathbb{Z}$, and $\mathbb{Z}_2 = \{0, 1\}$. In the other classes, all systems are topologically equivalent and therefore trivial by definition. For instance, the two-dimensional (2D) quantum-Hall systems are in class A without any symmetries. They are characterized by a $\mathbb{Z}$ invariant, which is, as we have seen, the Chern number. However, for other classes it is not always obvious how to define a suitable topological invariant.

2.1.3 The Hofstadter model

After having introduced the QHE and its topological origin, let us now have a look at a simple model that captures the physics of the QHE. More specifically, let us consider a system of non-interacting electrons in a 2D periodic potential with rectangular symmetry in the presence of a perpendicular magnetic field $\mathbf{B}$. This situation can be described in a nearest-neighbor tight-binding model of spinless fermions in a rectangular lattice. The

---

[7] At the mean-field level, also superconductors can be considered as systems with an excitation gap described by a single-particle Bogoliubov-de Gennes Hamiltonian.

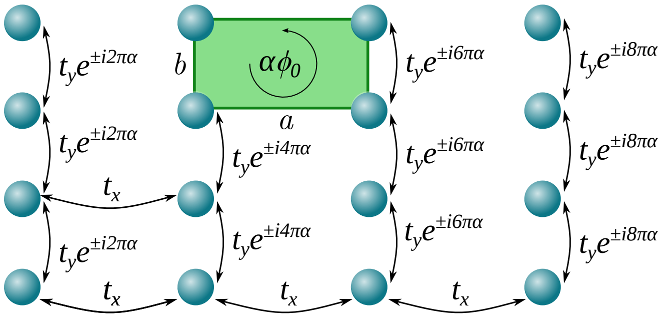
$t_y e^{\pm i2\pi\alpha}$
$t_y e^{\pm i4\pi\alpha}$
$t_y e^{\pm i6\pi\alpha}$
$t_y e^{\pm i8\pi\alpha}$
t_x
b
a
$\alpha\phi_0$

Figure 2.6: Hopping scheme of the Hofstadter model on a rectangular lattice in the Landau gauge. All lattice plaquettes of size $a \times b$ are penetrated by a magnetic flux of $\phi = \alpha\phi_0$ (green rectangle), where $\phi_0 = h/e$ is a magnetic flux quantum.

fermions are effectively spinless because we expect the magnetic field to fully spin-polarize the electrons of the system.

Let us first write down the model in the absence of the magnetic field:

$$\mathcal{H} = \sum_{j_x, j_y} t_x \, c^\dagger_{j_x+1, j_y} c_{j_x j_y} + \sum_{j_x, j_y} t_y \, c^\dagger_{j_x, j_y+1} c_{j_x j_y}. \tag{2.12}$$

Here, $c^\dagger_{j_x j_y}$ and $c_{j_x j_y}$ are electron creation and annihilation operators, t_x is the matrix element for nearest-neighbor hopping in the x direction, and t_y is the corresponding matrix element for the y direction. If we turn on a magnetic field $\mathbf{B} = B\mathbf{e}_z$ perpendicular to the lattice, each plaquette of the lattice will be penetrated by a magnetic flux

$$\phi = \int_\square d\mathbf{S} \cdot \mathbf{B} = \int_\square d\mathbf{S} \cdot (\nabla \times \mathbf{A}) = \int_{\partial\square} d\mathbf{l} \cdot \mathbf{A}, \tag{2.13}$$

where $\mathbf{A}$ is the electromagnetic vector potential. Thus, whenever an electron encircles one of the plaquettes, it picks up an Aharonov-Bohm phase factor of $e^{2\pi i\phi/\phi_0}$, with the magnetic flux quantum $\phi_0 = h/e$ [35]. This has to be incorporated in the tight-binding model and is typically done via the so-called Peierls substitution [16]: it corresponds to replacing all hopping matrix elements t_{ij} by $t_{ij} e^{2\pi i \int_i^j d\mathbf{l} \cdot \mathbf{A}(\mathbf{l})/\phi_0}$. In this way, the hopping phases around a plaquette add up correctly to the Aharonov-Bohm phase.

Without loss of generality, we choose the Landau gauge in which $\mathbf{A} = Bx\mathbf{e}_y$. By applying the corresponding Peierls substitution, our tight-binding model becomes

$$\mathcal{H} = \sum_{j_x, j_y} t_x \, c^\dagger_{j_x+1, j_y} c_{j_x j_y} + \sum_{j_x, j_y} t_y e^{-i2\pi j_x \alpha} \, c^\dagger_{j_x, j_y+1} c_{j_x j_y}, \tag{2.14}$$

where $\alpha \equiv \phi/\phi_0$ is the magnetic flux per plaquette in units of the magnetic flux quantum (see Fig. 2.6). This is the famous Hofstadter model which was studied in detail by Douglas Hofstadter in 1976 [36].

For irrational values of the magnetic flux α Hofstadter showed that the energy spectrum of the model can be mapped to the Cantor set: an uncountable set of real numbers in the unit interval of measure zero constructed by systematically removing the middle thirds in an infinite sequence of trisections. More specifically, the spectrum consists of uncountably many points which are *all* separated by finite energy gaps.

For rational values with $\alpha = p/q$, where p and q are integers and coprime, the situation is different. In this case, the model has translational symmetry with a periodicity of one lattice site in the y direction and q lattice sites in the x direction. This makes it possible to define a magnetic unit cell and to transform the model into momentum space [6]. The Hamiltonian reads

$$\begin{aligned}\mathcal{H} &= \sum_{k_x,k_y}\sum_{n=1}^{q-1} t_x e^{iak_x} d^\dagger_{k_x,k_y,n+1} d_{k_x k_y n} + \text{h.c.} \\ &\quad + \sum_{k_x,k_y}\sum_{n=1}^{q} 2t_y \cos\left(bk_y + \frac{2\pi p}{q} n\right) d^\dagger_{k_x k_y n} d_{k_x k_y n},\end{aligned} \tag{2.15}$$

where a and b are the lattice parameters of our rectangular lattice, and $d^{(\dagger)}_{k_x k_y n}$ are new creation/annihilation operators in momentum space. For fixed α, this Hamiltonian can be diagonalized easily to obtain the energy levels of the model. The spectrum has several key properties [36]: (i) the spectra for α and $\alpha + N$, where $N \in \mathbb{Z}$, are identical. For this reason, it is sufficient to consider only the interval $0 \leq \alpha < 1$. (ii) The Bloch bands break up into q distinct energy bands. (iii) For q odd, all energy bands are separated by a finite energy gap. There are $q-1$ energy gaps in total. (iv) For q even, all energy bands except the central two are separated by finite energy gaps. The two central bands touch at $E = 0$. In total, there are $q-2$ energy gaps while the half-filling gap is closed.

The Hofstadter spectrum is most beautifully illustrated as a function of the magnetic flux $\alpha = \phi/\phi_0$, as is demonstrated in Fig. 2.7(a). As we can see, the graph resembles a butterfly. This is why the spectrum is usually referred to as the “Hofstadter butterfly”. Most remarkably, the spectrum has a *fractal* structure. Particularly, Hofstadter showed that the graph is similar to itself, i.e., by zooming into certain parts of the spectrum, the spectrum is mapped onto itself up to a distortion.

Moreover, the Hofstadter bands are topologically nontrivial, i.e., each Hofstadter band

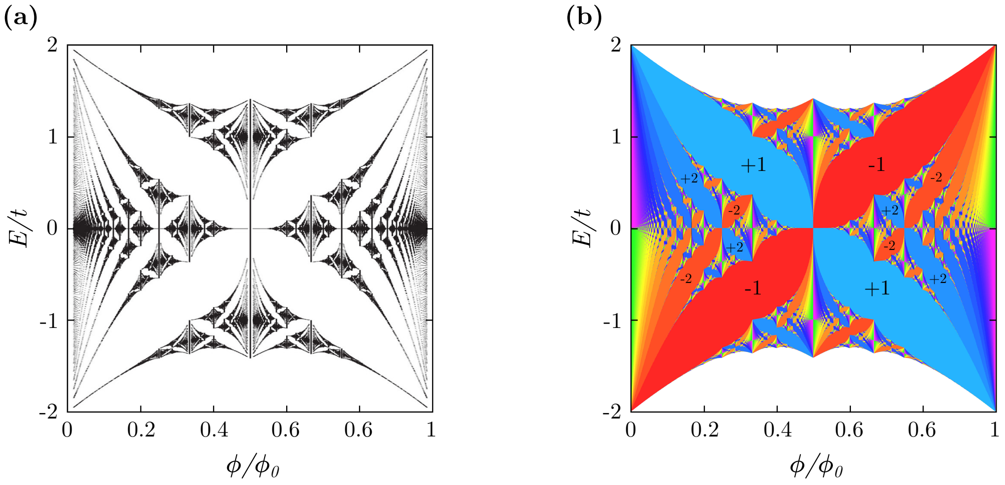

Figure 2.7: (a) The energy spectrum of the Hofstadter model as a function of the magnetic flux $\alpha = \phi/\phi_0$ [37] shows a pattern reminiscent of a butterfly. (b) The energy gaps of the Hofstadter butterfly can be colored according to their Hall conductivity σ in units of e^2/h [38]. Hall conductivities between -2 and $+2$ are indicated.

has a nontrivial Chern number ν [14, 15]. In this way, we can assign a nonzero Hall conductance σ to each energy gap in the Hofstadter spectrum corresponding to the sum of Chern numbers of all occupied bands up to the Fermi energy inside the considered energy gap. In fact, it has been shown that for q and p coprime the Hall conductances of the Hofstadter model take all nonzero values in the open interval $(-q/2, q/2)$ once and only once [38].

This is also in agreement with the so-called Diophantine equation [16],

$$r = q\mu + p\sigma, \tag{2.16}$$

an equation from the mathematical field of number theory, which must always hold for three positive integers r, q, p, where $|\sigma| \leq q/2$, $0 \leq r \leq q$, and μ and σ are integers. For fixed magnetic flux p/q, it can be shown that such an equation must be satisfied by the Hofstadter model, with r denoting the r-th gap such that r bands are occupied, and σ is the associated Hall conductivity in units of e^2/h. The Hall conductances of the Hofstadter energy gaps are illustrated in Fig. 2.7(b). This shows that the Hofstadter model is indeed a lattice realization of the integer quantum Hall effect.

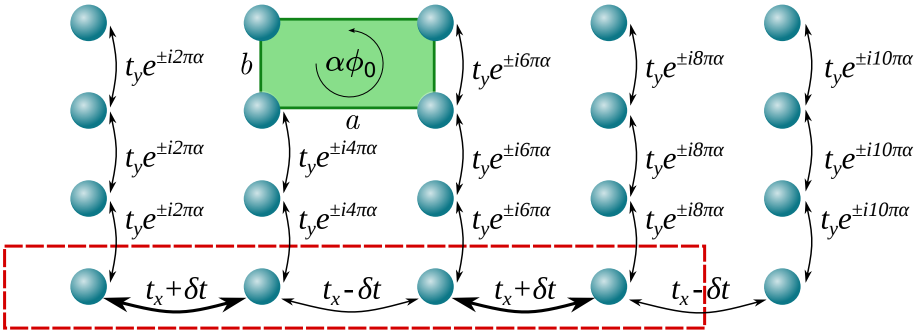
$t_y e^{\pm i2\pi\alpha}$
b
$\alpha\phi_0$
a
$t_y e^{\pm i4\pi\alpha}$
$t_y e^{\pm i6\pi\alpha}$
$t_y e^{\pm i8\pi\alpha}$
$t_y e^{\pm i10\pi\alpha}$
$t_x+\delta t$
$t_x-\delta t$

Figure 2.8: Hopping scheme in the Hofstadter model with a period-2 modulation of the hopping amplitudes in the x direction (dimerization). A magnetic unit cell for the case $\alpha = 1/4$ is also shown (red dashed rectangle).

2.2 The dimerized Hofstadter model

After having introduced the standard Hofstadter model as a platform for the QHE, we are now going to show that the topology of the Hofstadter model can be enriched by manipulating the underlying lattice. In particular, we will demonstrate that a moderate lattice dimerization causes a topological phase transition. The resulting topological phase is fundamentally different from the QHE phases since it features counter-propagating edge states not contributing to the Hall conductivity which have yet a topological origin. The work presented in the following sections is based on Ref. [39].

Recall the tight-binding model of the Hofstadter model introduced in the previous section. In addition, we consider the possibility of a lattice dimerization along one direction which leads to a modulation of hopping amplitudes as indicated in Fig. 2.8. For simplicity, we neglect a modulation of the magnetic fluxes, which would be present in a realistic system due to the change of the lattice parameter a. However, it can be verified that such a modulation leads to the same general results [39].

After performing a Fourier transformation only along the “undimerized” direction y, the new tight-binding Hamiltonian in mixed momentum-position space reads:

$$\begin{aligned}\mathcal{H} \;&=\; \sum_{j_x,k_y}[t_x-(-1)^{j_x}\delta t]\,(c^\dagger_{j_x+1,k_y}c_{j_xk_y}+c^\dagger_{j_xk_y}c_{j_x+1,k_y})\\ &\quad+\sum_{j_x,k_y}2t_y\cos(bk_y+2\pi\alpha j_x)\,c^\dagger_{j_xk_y}c_{j_xk_y},\end{aligned}\tag{2.17}$$

where α is, as before, the magnetic flux in units of the magnetic flux quantum ϕ_0, a and b are the lattice parameters of the rectangular lattice, $t_{x,y}$ are the average nearest-neighbor hopping amplitudes, while δt parametrizes the dimerization strength. In the previous section, we have seen that the standard Hofstadter model can be easily studied and diagonalized for rational values of the magnetic flux $\alpha = p/q$. To demonstrate the key consequences of a lattice dimerization, let us for the moment focus on a particular value of the magnetic flux, namely $\alpha = 1/4$. Later on, we will generalize our observations to arbitrary rational α values.

The magnetic unit cell of the $\alpha = 1/4$ dimerized Hofstadter model contains four inequivalent lattice sites (see Fig. 2.8). Therefore, the corresponding Bloch Hamiltonian in full momentum space can be written in terms of the Dirac matrices Γ_i and their commutators Γ_{ij} [40]. For a unit cell going from $j_x = 1$ to $j_x = 4$, the Hamiltonian reads

$$\begin{aligned} H(\mathbf{k}) \quad = \quad & t_y(\cos bk_y - \sin bk_y)\,\Gamma_5 + t_y(\cos bk_y + \sin bk_y)\,\Gamma_{21} + (t_x + \delta t)\,\Gamma_{45} \\ & + \frac{1}{2}(t_x - \delta t)(1 - \cos 4ak_x)\,\Gamma_{41} + \frac{1}{2}(t_x - \delta t)(1 + \cos 4ak_x)\,\Gamma_{23} \\ & - \frac{1}{2}(t_x - \delta t)\sin 4ak_x(\Gamma_{24} + \Gamma_{31}). \end{aligned} \tag{2.18}$$

Since the prime physical consequence of non-trivial topological states is the existence of chiral edge states, we study the dimerized Hofstadter model in a ribbon geometry with periodic boundary conditions in the y direction and open boundary conditions with a finite number of magnetic unit cells N_x in the x direction. Thus, the ribbon with $\alpha = 1/4$ is of width $W = 4N_x a$ and terminated by two boundaries perpendicular to the dimerization direction. The band structure of the ribbon is then determined via exact diagonalization of the first-quantized $4L \times 4L$ Hamiltonian corresponding to Eq. (2.17). The eigenstate weights at different lattice sites are used to identify possible edge states. Fig. 2.9 shows the ensuing band structure for $t_y = t_x/2$.

In the absence of dimerization, the bulk spectrum is gapped for filling fractions 1/4 and 3/4, but gapless at half filling with four bulk Dirac points. This is in agreement with the properties of the standard Hofstadter spectrum with magnetic flux ratio $\alpha = p/q$ with $p, q \in \mathbb{N}$ and $q = 2r$ even [36,38]. Recall that there are $q-2$ bulk energy gaps whereas the two central bands have q touching points at $E = 0$. Furthermore, within each bulk energy gap we observe one pair of counterpropagating edge states traversing the bulk gap localized at the edges of the system. Those can be attributed to the nontrivial bulk topology for the corresponding filling levels by bulk-boundary correspondence. Indeed, a calculation of the Chern number ν_n [14,15] for each energy band n yields Hall conductivities of $\sigma(1/4) = -1$ and $\sigma(3/4) = +1$. This gives rise to one topologically protected state per edge.

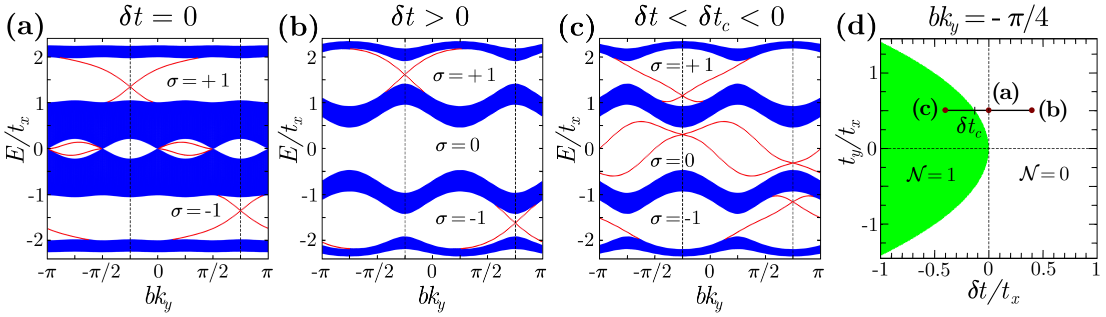

Figure 2.9: Band structures for the dimerized Hofstadter model in a ribbon geometry of width $W = 4N_x a$: $\alpha = 1/4$, $N_x = 100$. Parameters are (in units of t_x): (a) $t_y = 0.5$, $\delta t = 0$ (no dimerization). (b) $t_y = 0.5$, $\delta t = 0.4$ (trivial dimerization). (c) $t_y = 0.5$, $\delta t = -0.4$ (nontrivial dimerization). States localized at the edges of the system are highlighted in red. Hall conductivities σ for Fermi levels inside the bulk energy gaps are displayed in units of e^2/h. Relevant inversion-symmetric Aubry-André-Harper (AAH) cuts are indicated by dashed vertical lines. Note that in panel (c) there are nontrivial edge states at half filling although the corresponding Hall conductivity is zero. To explain this, a half-filling t_y-δt phase diagram is shown in panel (d) for the inversion-symmetric AAH model with $k_y b = -\pi/4$ and with respect to the 1D invariant $\mathcal{N}$ of Eq. (2.22). Points corresponding to panels (a)–(c) are indicated by red circles, including a possible path connecting them.

Interestingly, we also find two additional bands of edge states in between the four gap-touching points around $E = 0$. This already indicates that an opening of the half-filling gap might lead to a new topological phase with characteristic edge states. Indeed, for a finite dimerization mass $\delta t > 0$, the modulated hopping amplitude acts as a gap-opening perturbation yielding an additional insulating phase. However, the two additional bands of edge states between the touching points of the two central bands of Fig. 2.9(a) are pushed into the bulk continuum and localized in-gap states are absent [see Fig. 2.9(b)]. This is not surprising since we calculate a trivial Hall conductivity of $\sigma(1/2) = 0$ for the new half-filling gap. Hence, topological edge states are not expected for this phase. Besides, the edge states of the non-trivial insulating states in the 1/4 and 3/4 filling gaps are only slightly deformed signaling that the dimerization mass does not interfere with the bulk topological properties of the system.

The situation for $\delta t < 0$ turns out to be much richer. For small values of the dimerization mass, one again observes the opening of a bulk gap at half filling. However, at a critical value $\delta t = \delta t_c < 0$ [see Fig. 2.9(d) for a phase diagram] another gap closing and reopening occurs at $bk_y = -\pi/4$ and $bk_y = 3\pi/4$. Furthermore, in close proximity to these points a pair of counter-propagating chiral edge states [Fig. 2.9(c)] are revealed. Most notably, the half-filling Hall conductivity still vanishes. This is because the edge states' contributions to the Hall current is exactly opposite. By further increasing the dimerization, the corresponding edge bands are deformed. However, the doublets of in-gap edge states remain pinned at the momenta $bk_y = -\pi/4, 3\pi/4$ and remain inside the bulk energy gap *independent* of the value of δt and t_y.

2.3 One-dimensional Hofstadter slices with inversion symmetry: an analogy with the Aubry-André-Harper model

We now show that the presence of such doublets of half-filling in-gap edge states has a topological origin. In the form of Eq. 2.17, the dimerized Hofstadter model can be viewed as a collection of 1D chains parameterized by the momentum k_y. They are described by the following Hamiltonian,

$$\begin{aligned}\mathcal{H}_{k_y} \;=\; & \sum_{j_x}[t_x - (-1)^{j_x}\delta t]\,(c^\dagger_{j_x+1}c_{j_x} + c^\dagger_{j_x}c_{j_x+1}) \\ & + \sum_{j_x} 2t_y\cos(bk_y + 2\pi\alpha\, j_x)\, c^\dagger_{j_x}c_{j_x}. \end{aligned} \tag{2.19}$$

Just as the Hofstadter model, these chains are dimerized with a dimerization mass δt. Moreover, the magnetic field has been translated into a periodically modulated on-site potential of periodicity $1/\alpha$, amplitude $2t_y$, and phase bk_y. Intriguingly, these chains are equivalent to a specific combination of diagonal and off-diagonal Aubry-André-Harper (AAH) models [41–44]. AAH models have been the subject of intensive research because of their correspondence to a number of fundamental models, such as 2D lattice models with magnetic flux [44], the Kitaev model [45], or the Su-Schrieffer-Heeger (SSH) model [46]. For any value of k_y the AAH models possess time-reversal symmetry with $\Theta = K$, $k_x \to -k_x$, and $\Theta^2 = +1$, where K is complex conjugation. Furthermore, we are now going to show that all dimerized Hofstadter models with rational $\alpha = p/q$, with $p, q \in \mathbb{N}$ and coprime, possess at least two distinct AAH cuts with *inversion symmetry*.

Let us start with the undimerized case, where the hopping amplitudes t_x are constant throughout the lattice. The kinetic term of the Hamiltonian always preserves inversion symmetry, which is the reason why we have to focus on the on-site potentials. For given $\alpha = p/q$, one period of the on-site potential modulation is q lattice spacings. Without loss of generality, let us pick a unit cell that goes from $j = 1$ to $j = q$. To have an inversion center in the unit cell, the on-site potentials need to satisfy the following condition,

$$\cos\left(2\pi \frac{p}{q} j + bk_y\right) \overset{!}{=} \cos\left(2\pi \frac{p}{q} (q - j + 1) + bk_y\right). \tag{2.20}$$

This is always true, if we choose $bk_y = -\frac{p\pi}{q}$ as is straight-forward to verify. In addition, there is always a second point with $bk_y = -\frac{p\pi}{q} + \pi = \frac{q-p}{q}\pi$ at which the system obeys inversion symmetry. This case corresponds to substituting $t_y \to -t_y$.

Let us now check whether this statement also holds for the dimerized Hofstadter model. If q is even, a dimerization does not change the size of the magnetic unit cell, which consists of an even number of sites. The inversion center is exactly in the middle between the two central sites. Thus, an alternating hopping amplitude does not break inversion symmetry.

If q is odd, a dimerization doubles the unit cell. Thus, the unit cell comprises $2q$ lattice sites, which is an even number. Before adding the dimerization, the inversion center is exactly at the central lattice site of the undoubled unit cell. With the dimerization, it is between the two central sites of the doubled unit cell. Hence, we readily see that if the old unit cell preserves inversion symmetry, so does the new dimerized unit cell.

Therefore, the values of k_y for which the corresponding AAH chains have inversion symmetry are

$$bk_y = -\frac{p\pi}{q} \quad \text{and} \quad bk_y = \frac{q-p}{q}\pi. \tag{2.21}$$

Note that, in the case of periodic boundary conditions, these are not the only chains with inversion symmetry. The missing chains are those for which the chosen unit cell itself does not have inversion symmetry but the overall system does. The inversion center could, for instance, be exactly in between two adjacent unit cells. In such a system, however, the insertion of boundaries, i.e, taking a finite number of unit cells with open boundary conditions, would inevitably break inversion symmetry. Hence, any implications based on bulk-boundary correspondence would no longer hold and we, therefore, exclude these cases from our discussion. On the contrary, inversion symmetry is preserved also in the finite chain if the corresponding unit cells are themselves inversion-symmetric, i.e., for the k_y values in Eq. (2.21) above.

More generally, it can also be seen straight-forwardly that for any finite dimerized Hofstadter model with an *even* number of lattice sites in the direction of dimerization, there are at least two k_y cuts with inversion symmetry. In this case, the system consists of a certain number of complete unit cells plus an even number $2m$ of additional lattice sites. Let us choose the unit cells such that there are m of the additional sites at both ends of the chain. We already know that there must be two k_y values for which the chosen unit cells are inversion symmetric. From this, we immediately see that our arrangement of unit cells plus additional lattice sites is inversion symmetric for the same values of k_y. On the contrary, if the chain consists of an *odd* number of sites, the additional lattice sites cannot be arranged symmetrically around the unit cells. Thus, inversion symmetry is *always* broken.

In conclusion, we have shown that any dimerized Hofstadter model has *two* inversion-symmetric cuts in momentum space as long as the system has an *even* number of lattice sites in the direction of dimerization. Going back to our example of $\alpha = 1/4$, the inversion-symmetric 1D cuts are at $k_y b = -\pi/4$ or $3\pi/4$, with the 1D parity operator described by $P = \sigma^x \otimes \tau^x$, σ^i and τ^i being Pauli matrices.

2.4 Topological invariant for one-dimensional systems with inversion symmetry

We have seen that for momenta at which the dimerized Hofstadter ribbon exhibits pairs of degenerate mid-gap edge states at half filling the corresponding AAH chains have inversion symmetry. However, by going away from these points inversion symmetry is broken and the edge-state degeneracy is lifted. This indicates that the edge states might have a topological origin related to the presence of inversion symmetry.

In Sec. 2.1.2, we introduced the standard Altland-Zirnbauer table of topological insulators [26,30–34] which lists all possible topological phases based on the presence or absence of generic *non-spatial* symmetries and based on the dimension of the systems under consideration. Later, it was realized that the presence of additional *spatial* symmetries, such as point-group symmetries, can enrich the topology of a system. This led to the discovery of the so-called topological crystalline insulators (see Chapter 4) and various extensions of the standard Altland-Zirnbauer table. For these systems, the bulk-boundary correspondence is more restrictive: only the boundaries not breaking the defining spatial symmetries exhibit topological states!

In this light, the effective 1D inversion-symmetric AAH Hamiltonians fall into the orthogonal class AI with inversion symmetry of topological insulators with additional inver-

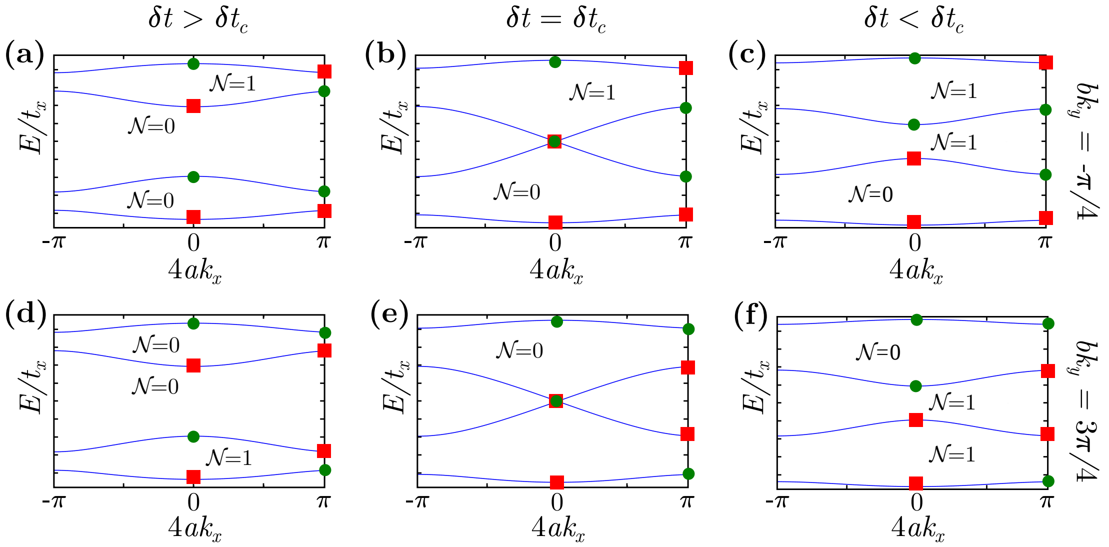

Figure 2.10: Bulk band structures for inversion-symmetric AAH models with and without dimerization: $\alpha = 1/4$, $t_y = 0.5t_x$; $\delta t = 0.4t_x$ in (a) and (d), $\delta t = \delta t_c = -1/8t_x$ in (b) and (e), $\delta t = -0.4t_x$ in (c) and (f). The parities at the inversion-invariant momenta $k_x = 0$ and $\pi/4a$ are indicated by green circles ($\zeta = +1$) and red squares ($\zeta = -1$). The topological invariants $\mathcal{N}$, corresponding to Fermi levels inside the respective bulk energy gaps, are also displayed.

sion symmetry introduced by Lu *et al.* [47]. Note that class AI of the original Altland-Zirnbauer table is trivial in 1D. With inversion symmetry, since inversion operator P ($P^2 = +1$) and time-reversal operator Θ ($\Theta^2 = +1$) commute, the 1D Hamiltonians now allow for a $\mathbb{Z}$ topological invariant. Such an integer invariant can be defined as follows [48]. Let us consider a 1D system on a chain with inversion symmetry described by the Bloch Hamiltonian $H(k)$, $k \in (-\pi/a, \pi/a]$. Inversion symmetry implies $P^{-1}H(k)P = H(-k)$ where P is a matrix representation of inversion. In particular, $H(k)$ commutes with P at the inversion-invariant momenta 0 and π/a. Thus, eigenstates of $H(k)$ have a well-defined parity $\zeta_i(k_{\text{inv}}) = \pm 1$ at those points. The eigenvalues of an operator cannot be changed by continuous deformations of the Hamiltonian, up to the order. However, a change of the order is only possible by closing and reopening the energy gap between two states. For a 1D inversion-symmetric system, an integer invariant is therefore defined by [48],

$$\mathcal{N} := |n_1 - n_2|, \tag{2.22}$$

where n_1 and n_2 are the number of negative parities at $k = 0$ and $k = \pi/a$, respectively.

Let us now apply this to the inversion-symmetric AAH cuts of our exemplary Hofstadter model with $\alpha = 1/4$. Fig. 2.10 shows 1D bulk spectra of the inversion-symmetric cuts corresponding to Fig. 2.9 for different values of the dimerization mass. Furthermore, the parities of the bulk states at the inversion-invariant momenta $k_x = 0$ and $k_x = \pi/4a$ are displayed. This enables us to calculate the topological invariant $\mathcal{N}$.

As an example, we discuss the results for $bk_y = -\pi/4$ and $t_y > 0$ [see Fig. 2.10(a)–(c)]. Independent of the dimerization mass, we find $\mathcal{N} = 1$ for 3/4 filling, and $\mathcal{N} = 0$ for 1/4 filling. This means the system is topologically nontrivial with one pair of degenerate end modes if the Fermi level is in the upper gap. On the contrary, we have a trivial system without end modes for 1/4 filling. Going back to the full Hofstadter model, this explains why the crossing of the 3/4 filling quantum Hall edge states are pinned to the point $bk_y = -\pi/4$.

At half filling, the situation is more subtle. For $\delta t > \delta t_c$, our calculations yield $\mathcal{N} = 0$, rendering the system topologically trivial. Indeed, we do not observe end modes in this case. In contrast to that, for $\delta t < \delta t_c$ the system is topologically nontrivial with $\mathcal{N} = 1$ and we find a pair of degenerate end modes in the finite system. The reason for this is that the $k_x = 0$ parities of the two central bands are switched while going from $\delta t > \delta t_c$ to $\delta t < t_c$: a band inversion takes place.

This explicitly explains the observed pinning of the degenerate edge states of the dimerized Hofstadter model at half filling. They originate from specific 1D cuts of the Hofstadter BZ corresponding to topologically nontrival inversion-symmetric AAH models. Notably, the corresponding Hall conductivity is zero.

2.5 Dimerized Hofstadter models with rational flux

In the following, we are going to explore other dimerized Hofstadter models with different rational values of the magnetic flux $\alpha = p/q$. In particular, we will discuss models with odd q which require a separate treatment. Finally, this will lead us to a generalization of our findings to arbitrary rational α.

2.5.1 Hofstadter models with half-integer flux: an analogy with the Su-Schrieffer-Heeger model

First of all, let us have a look at another interesting special case with even q, namely the dimerized Hofstadter model with $\alpha = 1/2$. It is worth a separate discussion since it can be mapped to the famous Su-Schrieffer-Heeger (SSH) model [46] with an additional mass

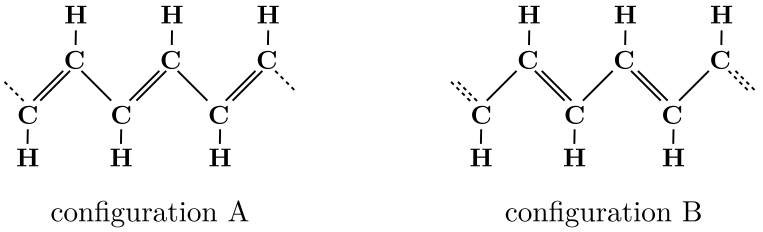

Figure 2.11: Two different configurations of polyacetylene. The two configurations are topologically distinct which gives rise to a topological state bound to any interface between them.

term. More specifically, in this case the Hofstadter model can be viewed as a collection of SSH models parameterized by k_y, in analogy with the general correspondence between Hofstadter and AAH model.

The SSH model is a simple model to describe the π electrons of a polyacetylene chain (see Fig. 2.11). Polyacetylene is an organic polymer consisting of long zigzag-shaped carbon chains with alternating single and double bonds in between them. In addition, one hydrogen atom is bonded to each carbon atom. This structure gives rise to two distinct configurations of polyacetylene, shown in Fig. 2.11, which can be transformed into each other by interchanging single and double bonds. Early electron spin resonance studies of polyacetylene suggested the presence of single unpaired electrons bound to domain walls of these two configurations. This was first explained in terms of domain-wall solitons, but was later revisited and understood in the language of topology. More specifically, the two polyacetylene configurations are topologically distinct such that an interface between them inevitably leads to a topological boundary state.

The physics of polyacetylene is captured by the SSH model, which is a nearest-neighbor tight-binding model for spinless fermions on a 1D chain subject to a dimerization, where the dimerization models the alternating single and double bonds of the carbon atoms. The 1D chains of our dimerized Hofstadter model with $\alpha = 1/2$ have an additional on-site potential term. The corresponding Bloch Hamiltonian is[8]

$$\begin{aligned} H_{k_y}(k_x) &= [(t_x+\delta t)+(t_x-\delta t)\cos(2ak_x)]\,\sigma^x-(t_x-\delta t)\sin(2ak_x)\,\sigma^y \\ &\quad -2t_y\cos(bk_y)\,\sigma^z, \end{aligned} \tag{2.23}$$

where $\sigma^{x,y,z}$ are Pauli matrices. The 1D inversion operator is $P = \sigma^x$ with $k_x \to -k_x$. It is easily checked that the system preserves inversion symmetry for $bk_y = \pm\pi/2$, in agreement with Eq. (2.21).

---

[8] The SSH model with an additional staggered on-site potential is also known as the Rice-Mele model [49].

Fig. 2.12 shows band structures of the dimerized Hofstadter model with $\alpha = 1/2$ in a ribbon geometry, similar to the one considered above for the case $\alpha = 1/4$. As expected from the general properties of the standard Hofstadter model, without dimerization the system is gapless with two bulk Dirac points [see Fig. 2.12(a)]. Furthermore, the Dirac points coincide with the inversion-symmetric cuts of the Hofstadter model.

For $\delta t > 0$, the Dirac points are gapped out without revealing any edge states [see Fig. 2.12(b)]. This is readily explained by a topological analysis: the Hall conductivity at half filling is $\sigma(1/2) = 0$, and also the 1D invariants for the inversion-symmetric cuts at $bk_y = \pm\pi/2$ are trivial with $\mathcal{N} = 0$. Hence, no topological edge states are expected by bulk-boundary correspondence.

On the contrary, for $\delta t < 0$ the topological analysis yields $\mathcal{N} = 1$ for both inversion-symmetric cuts, giving rise to one pair of end modes each, as can be seen in Fig. 2.12(c). However, the corresponding Hall conductivity is still zero.

This is in perfect agreement with the results presented above for $\alpha = 1/4$. It also reflects what is known for the SSH model [50]: at the inversion-symmetric cuts, the symmetry-breaking mass term associated with σ^z vanishes. In this case, the SSH model features topological end modes for a negative dimerization mass. However, away from those points the SSH model contains a σ^z term that gaps out the end modes. This is exactly what happens in Fig. 2.12(c).

2.5.2 Hofstadter models with odd-denominator fluxes

The dimerized Hofstadter model with $\alpha = p/q$ and q odd requires a separate analysis. This is primarily due to the doubling of the magnetic unit cell in the presence of a dimerization. We will first start with a general discussion based on an analysis of numerous Hofstadter models with different α. After that, we will discuss the case $\alpha = 1/3$ in more detail.

In the Hofstadter model, hopping amplitudes with respect to the y direction are modulated along the x direction with a period of q lattice sites, giving rise to a magnetic unit cell of exactly this size. However, if q is odd, such a period is no longer reconcilable with the periodicity of the hopping amplitudes with respect to the x direction once a dimerization has been turned on. The greatest common divisor of the two periods is 2, which is the reason why the magnetic unit cell must be doubled in the dimerized case.

Without dimerization, the bulk band structure of the Hofstadter model with odd q consists of q bands with $q-1$ full energy gaps separating them. In particular, the Fermi

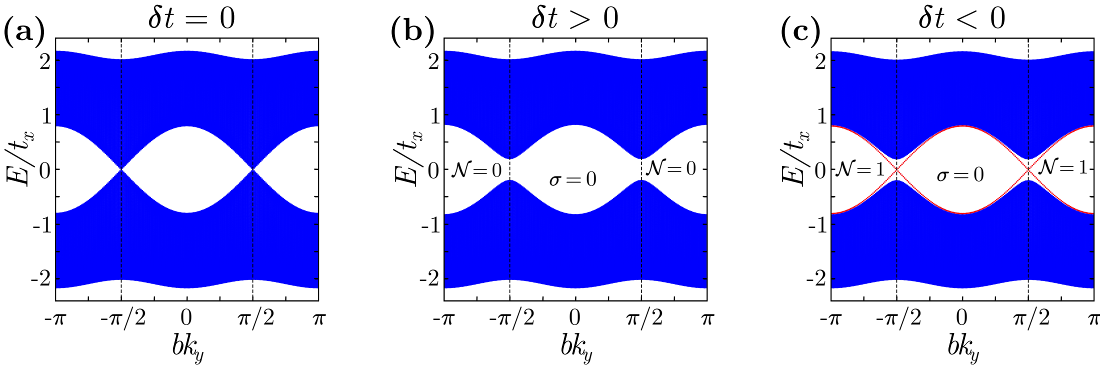

Figure 2.12: Band structures for the dimerized Hofstadter model in a ribbon geometry of width $W = 2N_x a$: $\alpha = 1/2$, $N_x = 200$. Parameters are (in units of t_x): (a) $t_y = 0.4$, $\delta t = 0$ (no dimerization). (b) $t_y = 0.4$, $\delta t = 0.1$ (trivial dimerization). (c) $t_y = 0.4$, $\delta t = -0.1$ (nontrivial dimerization). States localized at the edges of the system are highlighted in red. Hall conductivities σ for Fermi levels inside the bulk energy gaps are displayed in units of e^2/h. The inversion-symmetric AAH cuts are indicated by dashed vertical lines. The 1D invariants $\mathcal{N}$ for the inversion-symmetric cuts are also shown. Note that the latter is only nontrivial for $\delta t < 0$.

level of a half-filled system can never be inside one of the gaps. Furthermore, as for the case with even q, a Diophantine equation can be used to infer that the Hall conductivities σ, associated with Fermi levels inside the various gaps, assume every value in the open interval $(-\frac{q}{2}, \frac{q}{2})$ once and only once [38].

Due to the doubling of the magnetic unit cell in the presence of a dimerization, the magnetic BZ is folded in the direction of k_x. This leads to a doubling of the energy bands in the new magnetic BZ, which now features $2q$ bulk energy bands. A closer inspection shows that related bands touch along the $k_x = \pm\pi/2qa$ edges of the new BZ, if we artificially set the dimerization mass to zero. In this case, we have q pairs of bands separated by $q - 1$ bulk energy gaps, while the associated Hall conductivities must be the same as before.

By turning on the dimerization, the touching points within the pairs of bands are gapped out, revealing q additional bulk energy gaps. In total, we thus have $2q - 1$ bulk energy gaps. In particular, there is now also a half-filling gap. We again find that the half-filling gap is associated with a Hall conductivity of $\sigma = 0$.

Independent of the sign of the dimerization mass δt the Hall conductivity vanishes at half filling. Nevertheless, the gap closing at $\delta t = 0$ switches the parities at $k_x = \pm\pi/2qa$ in the inversion-symmetric cuts, giving rise to two different topological sectors with respect to the 1D invariant $\mathcal{N}$. Consequently, there are topological edge states for $\delta t < 0$ with zero Hall conductivity solely due to inversion symmetry in the 1D cuts.

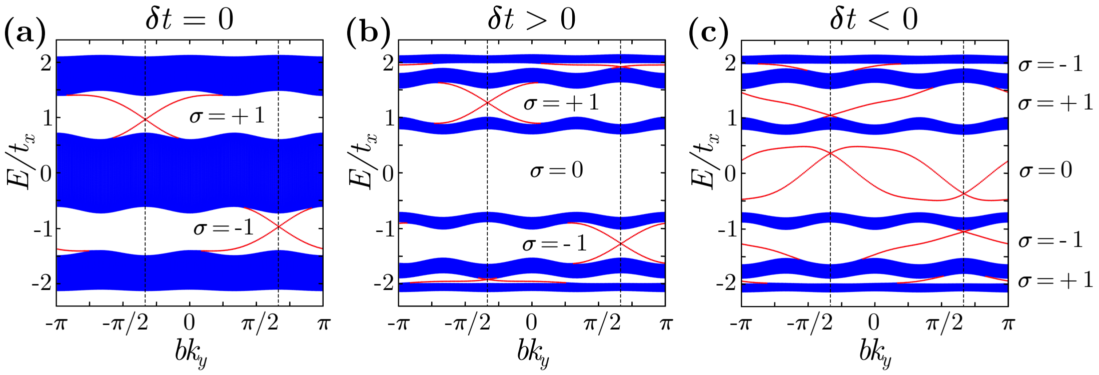

Figure 2.13: Band structures for the dimerized Hofstadter model in a ribbon geometry of width $W = 6N_x a$: $\alpha = 1/3$, $N_x = 60$. Parameters are (in units of t_x): (a) $t_y = 0.4$, $\delta t = 0$ (no dimerization). (b) $t_y = 0.4$, $\delta t = 0.4$ (trivial dimerization). (c) $t_y = 0.4$, $\delta t = -0.4$ (nontrivial dimerization). States localized at the edges of the system are highlighted in red. Hall conductivities σ for Fermi levels inside the bulk energy gaps are displayed in units of e^2/h for (c) (equivalent gaps in (b) and (c) have the same Hall conductivity). The relevant inversion-symmetric AAH cuts are indicated by dashed vertical lines.

Let us now demonstrate the general results for a specific system, namely the dimerized Hofstadter model with $\alpha = 1/3$. The 6×6 Bloch Hamiltonian $H(k_x, k_y)$ has the following components,

$$\begin{aligned} H_{nn} &= 2t_y \cos(\frac{2\pi}{3} n + bk_y), \quad n = 1, \ldots, 6 && (2.24)\\ H_{n,n+1} &= H_{n+1,n} = t_x - (-1)^n \delta t, \quad n = 1, \ldots, 5 && (2.25)\\ H_{1,6} &= H^*_{6,1} = (t_x - \delta t) e^{i6ak_x}, && (2.26) \end{aligned}$$

while all other components are zero. The relevant 1D inversion operator P for this representation is simply the matrix with ones along the anti-diagonal and zeros elsewhere.

In Fig. 2.13, band structures of this Hofstadter model in a ribbon geometry are shown. Furthermore, 1D bulk band structures for the corresponding AAH models are plotted in Fig. 2.14 to explain the 1D topology of the relevant inversion-symmetric cuts.

As expected, without dimerization we see two bulk energy gaps with nontrivial Hall conductivities of $\sigma = \pm 1$, giving rise to the pairs of counterpropagating edge states we observe in Fig. 2.13(a). Moreover, they are pinned to the inversion-symmetric cuts. This is in agreement with the topological analysis in Fig. 2.14.

For nonzero δt, the gaps attributed to the folding of the magnetic BZ open. Looking at the behavior of the inversion-symmetric cuts in Fig. 2.14, we observe that the $k_x = \pi/6a$

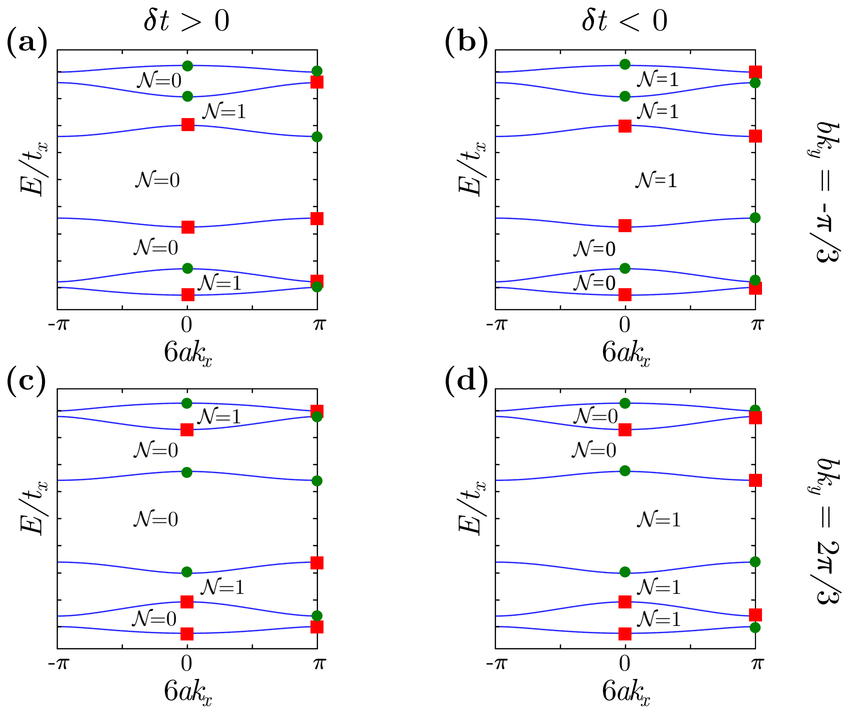

Figure 2.14: Bulk band structures for inversion-symmetric AAH models with and without dimerization: $\alpha = 1/3$, $t_y = 0.4t_x$; $\delta t = 0.4t_x$ in (a) and (c), $\delta t = -0.4t_x$ in (b) and (d). The parities at the inversion-invariant momenta $k_x = 0$ and $\pi/6a$ are indicated by green circles ($\zeta = +1$) and red squares ($\zeta = -1$). The topological invariants $\mathcal{N}$, corresponding to Fermi levels inside the respective bulk energy gaps, are also displayed.

parities of three pairs of bands, including the two central bands, switch by going from $\delta t > 0$ to $\delta t < 0$. This is a characteristic feature of Hofstadter models with odd q. For even q, this generically happens only for the two central bands. At half filling, this leads to topological edge states with zero Hall conductivity, but nontrivial $\mathcal{N} = 1$, for $\delta t < 0$.

The Hall conductivities at 1/6 and 5/6 filling are nontrivial with $\sigma = \pm 1$, independent of δt. However, due to the change of the 1D topology at $\delta t = 0$ their behavior is different for negative and positive δt. For instance, the crossing of the 1/6-filling edge states is at $bk_y = -\pi/3$ for $\delta t > 0$, where it is forced to stay inside the bulk energy gap due to the nontrivial 1D invariant $\mathcal{N} = 1$. On the contrary, for $\delta t < 0$ the crossing is expected at $bk_y = 2\pi/3$, but it can disappear into the bulk since the 1D invariant $\mathcal{N}$ is trivial.

2.5.3 Generalization to arbitrary rational flux

The results presented above, and the analysis of dimerized Hofstadter models with other rational values of the magnetic flux $\alpha = p/q$, suggest a generalization of the observed features.

For even q, the situation is very similar to the cases $\alpha = 1/4$ and $1/2$: without dimerization, the corresponding Hofstadter models are gapless at half filling because the two central gaps touch at zero energy. These bulk Dirac points are gapped out by a mass induced by the dimerization and a bulk energy gap with zero Hall conductivity opens. Furthermore, the system always possesses two inversion-symmetric 1D cuts. Generically, we find two situations: either two of the Dirac points coincide with the inversion-symmetric cuts, or the inversion-symmetric cuts are between two Dirac points. In the former case, the system exhibits one pair of topological edge states for $\delta t < 0$, whereas the system is trivial for $\delta t > 0$ (c.f. the model with $\alpha = 1/2$). In the other case, for instance $\alpha = 1/4$, the bulk gap closes and reopens a second time at some t_y-dependent $\delta t_c < 0$. This is the point where the phase transition from $\mathcal{N} = 0$ to $\mathcal{N} = 1$ takes place. Apart from the shifted transition point, the observations are qualitatively the same for both cases.

For odd q, the situation is more subtle, as we have discussed in the previous section. First of all, the magnetic unit cell is doubled due to the dimerization, giving rise to an even number of bands in the folded magnetic BZ. In this BZ, the nonzero dimerization mass opens a full half-filling gap with zero Hall conductivity as in the case with even q. For $\delta t < 0$, we again find topological edge states pinned to the inversion-symmetric cuts of the BZ which are characterized by a nontrivial 1D invariant $\mathcal{N}$. In contrast to that, there are no edge states for $\delta t > 0$. This can be attributed to both the zero Hall conductivity and the trivial value for $\mathcal{N}$.

We conclude that a dimerization in the Hofstadter model with *rational* magnetic flux α opens an energy gap at half filling (see Fig. 2.15). The Hall conductivity associated with this energy gap is zero. However, topological mid-gap edge states appear, if the dimerization mass δt is negative and its magnitude is sufficiently large. The topological states originate from 1D inversion-symmetric momentum-space cuts for two specific momenta k_y. The values of these momenta depend on α and on the way the system is terminated.

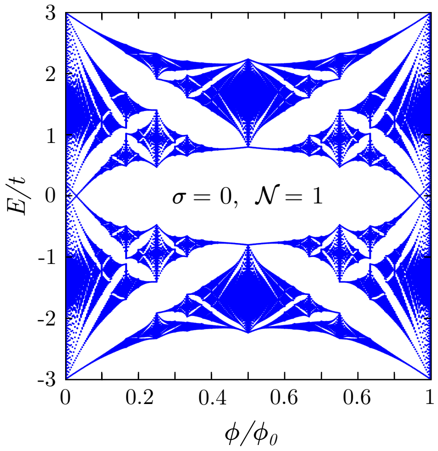

Figure 2.15: The Hofstadter butterfly with $t_y = t_x/2$ in the presence of an additional dimerization with $\delta t = -0.4$. A large half-filling gap with Hall conductivity $\sigma = 0$ is opened while the corresponding 1D invariant $\mathcal{N} = 1$ is nontrivial.

2.6 Possible experimental realization and detection

In order to detect the topological edge states discussed in this chapter, it would be desirable to realize one of the simpler Hofstadter models with magnetic fluxes 1/2, 1/3 or 1/4, simply because the total number of bands is small and the energy gaps are large. However, it was already pointed out by Hofstadter for his original model that this would require an enormous magnetic field [36]. To understand that, recall the definition of α as the ratio of magnetic flux per plaquette to magnetic flux quantum, i.e.,

$$\alpha = \frac{\phi}{\phi_0} = \frac{Bab\,e}{h}. \tag{2.27}$$

In real crystals, typical lattice spacings are of the order of several Å. In order to reach, for instance, a magnetic flux of $\phi_0/4$ per lattice plaquette, we would need an enormous magnetic field of the order of 10^5 T. Therefore, the experimental realization of the Hofstadter model and its remarkable features seem to be out of reach. Nevertheless, significant technological advances in the last decades have revived the experimental and theoretical research on the Hofstadter model and other related models.

One approach to realizing the Hofstadter model is the preparation of moiré superlattices [37]. This was first realized for the Hofstadter model on a honeycomb lattice [51–53]. For that, bilayer graphene was placed on top of hexagonal boron nitride (hBN) under a relative angle θ. The lattice constants of graphene and hBN also differ by approximately

2%. This creates a lattice mismatch and the ensuing superstructure forms a periodic pattern with a much larger lattice constant of the order of 10 nm, which can be tuned by the misalignment angle θ. Thus, the required magnetic field for sizable flux values per unit cell shrinks down to several Tesla, which can be reached easily in the lab. Following the same line of thought, two different rectangular lattices could be used to realize the Hofstadter model on a rectangular lattice. Edge states could than be detected by performing tunneling probe measurements at the edges with a bias voltage tuned to one of the Hofstader energy gaps.

Another promising experimental platform for the realization of the dimerized Hofstadter model is an ultracold-atom setup [54–56]. In such a system, a neutral bosonic or fermionic quantum gas is cooled down close to abolsute zero and then loaded into an optical trap. In addition, the gas is subjected to two overlapping counterpropagating laser beams. In this way, the laser beams form an optical standing wave and the particles of the quantum gas condensate to the minima of the resulting periodic potential: a 1D optical lattice is formed. By adding more pairs of mutually orthogonal laser beams, also two-dimensional and three-dimensional lattices can be realized. Furthermore, additional lasers can be used to induce tunneling of atoms between lattice sites with an arbitrary phase. Effectively, this realizes a system of quantum particles hopping in an optical lattice. In particular, by tuning the lasers to implement nonzero phases for the hopping processes of the particles also effective magnetic fluxes, as required for the Hofstadter model, can be simulated. Besides, experimentalists have come up with even more sophisticated setups to realize effective interactions, artificial gauge fields, and artificial spin-orbit coupling in ultra-cold atom setups [54, 55, 57, 58]. In this way, systems of ultracold atoms in optical lattices have become a very rich playground for the realization of various theoretical models. In particular, these systems feature an exceptional tunability which brings a much wider range of accessible model parameters into reach.

Also the Hofstadter model and its topological features have been studied in such a setup [59–61]. Starting from there, a dimerization of the hopping parameters can be easily implemented by using additional lasers. The topological edge states studied in this chapter could then be detected with optical diagnostics or with time-of-flight measurements [55]. For the former, the atomic cloud is illuminated with a laser beam and images of the shadow cast by the atoms are used to infer the spatial distribution of the atomic cloud. For the latter, the confining trap potential and the additional lasers are switched off abruptly, such that the atomic cloud can expand freely subject to its initial momentum distribution. In this way, the edge states can be identified directly.

We have seen that the Hofstadter model can also be viewed as a collection of one-dimensional AAH models. Therefore, a promising route towards the experimental detection of the pinned degenerate topological states would be the realization of the inversion-symmetric AAH models. This could be done in an ultracold-atom setup with a 1D optical lattice, similar to the Hofstadter experiment described above. Alternatively, AAH models can be realized in another, highly tunable experimental platform: photonic crystals [62,63]. For that, a periodic lattice of coupled single-mode waveguides can be prepared on a 2D substrate, where each waveguide corresponds to a lattice site of the finite 1D AAH model [43, 63]. The small spacing between waveguides allows a light wave, propagating through one of the guides, to tunnel between neighboring waveguides thereby simulating a hopping process. Furthermore, the width of a waveguide determines the propagation properties of a light wave, which is used to simulate and vary the on-site potentials for different lattice sites. In this way, all the model parameters of Eq. (2.17) could be implemented and adjusted. By injecting light into one of the outermost (boundary) waveguides and by measuring the outgoing intensity distribution, the localized topological end states could then be detected directly.

3 One-dimensional Dirac electrons on the surface of weak topological insulators

3.1 Introduction

3.1.1 The quantum spin-Hall effect

The discovery of the QHE, with its potential applications for new electronic devices and its importance for quantum metrology[9], spawned the search for other related physical effects [3, 4, 8]. One of these effects, namely the quantum spin-Hall effect (QSHE), is at the basis of the family of time-reversal invariant (TRI) topological insulators (TIs), which are the focus of this chapter.

Before introducing the QSHE, let us recall the main features of the "charge" QHE. The hallmark of the QHE is the presence of a quantized current transverse to an electric field, i.e., $j_x = \sigma_H E_y$. Furthermore, the Hall conductance σ_H is directly related to the topology of the occupied electronic states via the Chern number[10] n. A consequence of this nontrivial topology is the existence of chiral edge states, which give rise to dissipationless charge transport. In conventional semiconducting materials, the QHE typically requires a strong external magnetic field[11] that limits its potential for technical applications. However, as

---

[9] Quantum metrology is the study of quantum techniques and quantum effects that allow to perform measurements of physical parameters with much higher precision as compared to purely classical approaches [64]. In particular, the precise quantization of the quantum-Hall resistance in multiples of e^2/h to almost one part in a billion has led to a definition of a new practical standard for electrical resistance [65, 66]. Furthermore, the QHE can be used to determine the fundamental fine structure constant with an extremely high precision [1].

[10] From now on, we are going to denote the Chern number by n instead of ν. This is to avoid confusion with the $\mathbb{Z}_2$ invariants introduced in this chapter, which are typically denoted by ν in the literature.

[11] We note again that graphene represents an important exception. In graphene, the QHE has been observed at magnetic fields far below 1 T, which can be reached with permanent magnets at low temperatures [20].

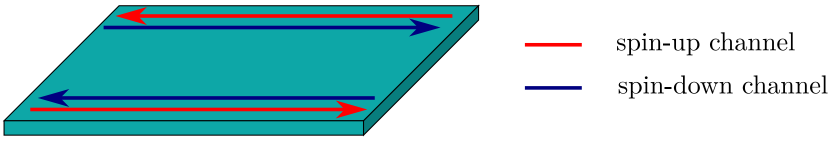

Figure 3.1: Illustration of the helical edge states in the QSHE.

we have mentioned in the previous chapter, it is also possible to realize the QHE in the absence of an external magnetic field, an effect which is called the quantum anomalous Hall effect (QAHE). Note that such systems still break time-reversal symmetry due to nonvanishing local magnetic fluxes.

It can be shown that the Chern number n of an isolated band reverses its sign under the operation of time reversal Θ, i.e., $\Theta n = -n$ [67]. For insulating systems with time-reversal symmetry, the Chern number must therefore be zero. Hence, materials with nonzero net Chern number, such as QAHE systems, necessarily break time-reversal symmetry.

The theoretical prediction [68–71] and subsequent experimental discovery [72] of the quantum spin-Hall effect showed that quantized topological features are not only restricted to magnetic systems with broken time-reversal symmetry. In the QSHE, a pair of spin-polarized edge states counterpropagate at each edge of a 2D sample. In this way, the direction of propagation is locked to the spin of the edge states, which is why they are usually referred to as *helical*[12] edge states [8] (see Fig. 3.1). Similar to the "charge" QHE, the edge states give rise to a quantized current transverse to an external electric field. However, there is an important qualitative difference: the helical nature of the edge states leads to a quantized *spin* accumulation at the two edges transverse to the current direction[13]. This property makes the QSHE particularly interesting for novel devices in spintronics, a branch of electronics that seeks to exploit the electron's spin degree of freedom for data storage and transfer. Besides, there is no charge accumulation at the edges, as opposed to the QHE.

To understand the features of the QSHE, let us use the following thought experiment: consider a insulating system of spin-up electrons in two dimensions which realizes a QAHE with net Chern number $n_\uparrow$. Next, we add a time-reversed copy of the same system. We already know that time-reversal flips the spin and reverses the Chern number. Hence, our copy satisfies $n_\downarrow = -n_\uparrow$. In this way, the two subsystems correspond to two different spin species subject to opposite "internal" magnetic fields. The two systems individually break time-reversal symmetry but taken together the overall system is invariant under time reversal. Its net Chern number $n = n_\uparrow + n_\downarrow = 0$ vanishes. Moreover, the subsystems give rise to chiral edge states with opposite chirality, i.e., the two spin channels form a pair of helical edge states. Hence, we have constructed a system realizing the QSHE. It is characterized by the so-called *spin Chern number* [3, 70, 73],

---

[12] The helicity of a state is the normalized projection of its spin onto its momentum.

[13] Note that the spin accumulation is only quantized if the system has spin-rotation symmetry about one spin axis, for instance S^z. The presence of helical edge states, however, is a generic *topological* feature of these systems as we will see in the next section.

$$n_S = n_\uparrow - n_\downarrow, \tag{3.1}$$

which is a number in $2\mathbb{Z}$, i.e., it only assumes even integer values. The corresponding spin-Hall conductivity is then given by $\sigma_S = n_S\, e^2/h$.

From the construction above, we can easily explain the observed features of the QSHE: the transverse conductance assumes *even* multiples of e^2/h because *both* edges now contribute to the current. The charge accumulation at the edges vanishes because both spin channels contribute quantum-Hall charge accumulations of the same magnitude but opposite sign. However, since the spin of the two channels is different, spin is accumulated at the two edges.

A few remarks are in order. We have seen that in the QSHE both spin species effectively see opposite magnetic fields leading to opposite Chern numbers. Without breaking time-reversal symmetry, such a situation can only be achieved in systems with strong spin-orbit coupling (SOC), where the SOC acts like a momentum-dependent orbital magnetic field [69]. Therefore, strong SOC is a necessity for the QSHE. This is the case, for instance, in hole-doped semiconductors such as Si, Ge, or GaAs [68]. Indeed, the QSHE was first experimentally observed in HgTe/CdTe semiconductor quantum wells [72].

So far, we have assumed the system to have spin-rotation symmetry about one spin axis, for instance S^z. In fact, if we relax this assumption, the spin Chern number n_S is no longer well-defined. Does this lead to a break-down of the QSHE? Not quite! It turns out that a QSHE system still has a robust quantized transverse *charge* conductivity even if spin-rotation symmetry is completely broken. Also, it still gives rise to a spin transfer between the edges which is, however, no longer quantized [70]. In fact, as we will see in the next section, the QSHE with spin-rotation symmetry is a special case of the so-called *quantum spin-Hall insulator* [74]. These systems are protected solely by time-reversal symmetry and characterized by a $\mathbb{Z}_2$ topological invariant. For the QSHE with spin-rotation symmetry, this invariant is simply given by [3]

$$\nu = n_S \bmod 4. \tag{3.2}$$

If spin-rotation symmetry is broken (but time-reversal symmetry is not), this invariant retains its value even though $n_\uparrow$ and $n_\downarrow$ are no longer well-defined. Moreover, the $2\mathbb{Z}$ classification reduces to a $\mathbb{Z}_2$ classification because the two spin channels can now mix. In this way, pairs of helical edge channels can always be gapped out such that only the evenness or oddness of the number of helical states is a protected topological feature.

3.1.2 The quantum spin-Hall insulator in two dimensions

The quantum spin-Hall insulator (QSHI) is a 2D topological system of spin-1/2 fermions protected by time-reversal symmetry. For a system of fermions with spin 1/2, the time-reversal operator Θ typically has the form [75]

$$\Theta = e^{i\pi\frac{1}{2}s^y} K = is^y K \tag{3.3}$$

where s^y is a Pauli matrix acting on spin, and K is complex conjugation. We readily see that $\Theta^2 = -1$. Hence, the QSHI is in the symplectic Altland-Zirnbauer symmetry class AII [34]. In two dimensions, this class allows for a $\mathbb{Z}_2$ topological invariant (see Sec. 2.1.2) with the QSHI being associated with the nontrivial phase. There are several equivalent formulations of this invariant [16, 74, 75]. In the following, we are going to introduce the formulation developed by Fu and Kane [75].

Fu-Kane invariant for $\mathbb{Z}_2$ insulators in two dimensions

When spin-rotation symmetry is completely broken, it is no longer possible to decompose the system into two separate spin channels. Nonetheless, a time-reversal invariant system with $\Theta^2 = -1$ must obey Kramers' theorem which tells us that every state of the system comes with a time-reversed partner of the same energy. For a lattice-periodic system this means that for every Bloch state with momentum $\mathbf{k}$ there must be a degenerate state at momentum $-\mathbf{k}$. Thus, a time-reversal invariant system with $\Theta^2 = -1$ has an even number of energy bands that are always decomposable into two time-reversed channels. This is at the basis of the Fu-Kane invariant.

Let us view the 2D BZ of a time-reversal invariant system as a collection of 1D slices. Furthermore, let two of the slices go through the time-reversal invariant points $(0, 0)$,

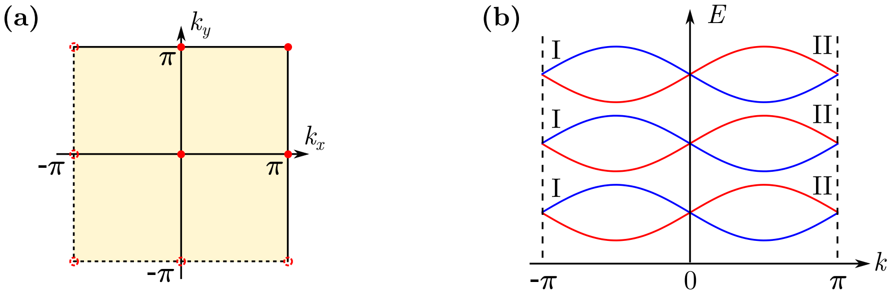

Figure 3.2: (a) BZ of a 2D system with time-reversal symmetry. Time-reversal invariant lines and momenta are indicated by black lines and red dots, respectively. Dashed lines and dots are connected to their solid counterparts by a reciprocal lattice vector $\mathbf{G}$. (b) Schematic band structure of a 1D system with time-reversal symmetry. The occupied bands decompose into two time-reversed channels I (blue bands) and II (red bands) which form Kramers doublets at the time-reversal invariant momenta $k = 0$ and π.

$(\pi, 0)$, $(0, \pi)$, and (π, π) [see Fig. 3.2(a)], which satisfy $-\mathbf{k} = \mathbf{k} + \mathbf{G}$, where $\mathbf{G}$ is a reciprocal lattice vector[14]. These two slices represent time-reversal invariant 1D systems. Let us have a closer look into those. Due to Kramers' theorem, the energy bands must come in pairs which are degenerate at the time-reversal invariant 1D momenta $k = 0$ and $k = \pi$ [see Fig. 3.2(b)]. We can then divide the $2N$ occupied bands into N pairs subject to

$$|u^{\mathrm{I}}_{-k,\alpha}\rangle = -e^{i\chi_\alpha(k)}\,\Theta|u^{\mathrm{II}}_{k,\alpha}\rangle, \tag{3.4}$$

where the labels I and II refer to the two time-reversed channels, $\alpha = 1, \ldots, N$ labels the pairs, and $\chi_\alpha(k)$ are smooth functions[15]. This decomposition allows us to analyze the two time-reversed channels separately. In particular, let us have a look at the charge polarization of each channel, the so-called *partial polarization*,

$$P^s = \frac{1}{2\pi}\int_{-\pi}^{\pi} dk\, A^s(k), \tag{3.5}$$

---

[14] For clarity, all lattice constants have been set to unity.

[15] We have assumed that there are no other band crossings except those required by Kramers' theorem. This is not a restriction, since any time-reversal invariant system with $2N$ fully occupied bands can be continuously connected to this case. Furthermore, we will see that the Fu-Kane invariant is not affected by additional degeneracies within the occupied bands as long as the bands are defined continuously.

which is expressed in terms of the Berry potential

$$A^s(k) = i \sum_{\alpha=1}^{N} \langle u^s_{k,\alpha} | \partial_k | u^s_{k,\alpha} \rangle, \tag{3.6}$$

with $s = \mathrm{I}, \mathrm{II}$. It is important to note that the polarizations are not gauge-invariant. More specifically, the polarizations can change by an integer multiple of a lattice constant under $U(2N)$ gauge transformations of the states $|u_{k,n}\rangle$. To proceed further, Fu and Kane introduced the *time-reversal polarization*, which is defined as the difference

$$P_\theta = P^I - P^{II}. \tag{3.7}$$

They found that P_θ is an integer which is only defined modulo 2. Moreover, using Eqs. (3.4) and (3.5), they found the relation

$$(-1)^{P_\theta} = \frac{\sqrt{\det[w(0)]}}{\mathrm{Pf}[w(0)]} \frac{\sqrt{\det[w(\pi)]}}{\mathrm{Pf}[w(\pi)]}, \tag{3.8}$$

where $\mathrm{Pf}(A)$ denotes the Pfaffian of an antisymmetric matrix A, a quantity whose square is equal to the determinant of the matrix[16]. The matrix $w(k)$ is a unitary $2N \times 2N$ matrix, defined as

$$w_{mn}(k) = \langle u_{-k,m} | \Theta | u_{kn} \rangle, \tag{3.9}$$

which relates time-reversed wave functions. In particular, it is antisymmetric at the time-reversal invariant momenta $k = 0$ and $k = \pi$.

Eq. (3.8) already looks very promising. However, P_θ alone is not a gauge-invariant quantity because its value can be changed by an integer under a gauge transformation of the states $|u^I_{k\alpha}\rangle$ in one of the time-reversed channels. This issue is resolved by going back to the original two-dimensional system. Let us look again at the collection of one-dimensional BZ slices, which we parameterize by q, and let us keep track of the evolution of $P_\theta(q)$ from $q = 0$ to π. At the end points of this path, the corresponding 1D systems are time-reversal invariant. Thus, $P_\theta(0)$ and $P_\theta(\pi)$ are integers. In between, 1D time-reversal symmetry is broken and $P_\theta(q)$ can assume *any* value. If we choose a continuous gauge throughout the 2D BZ, also $P_\theta(q)$ changes continuously from 0 to π. The change of $P_\theta(q)$, namely $\Delta = P_\theta(\pi) - P_\theta(0)$, is gauge-invariant modulo 2 and therefore defines a $\mathbb{Z}_2$ topological invariant $\nu = \Delta \bmod 2$. This is the Fu-Kane invariant characterizing a 2D insulator with

---

[16] Note that Eq. (3.8) is only valid in a gauge in which $w(k)$ is a continuous function.

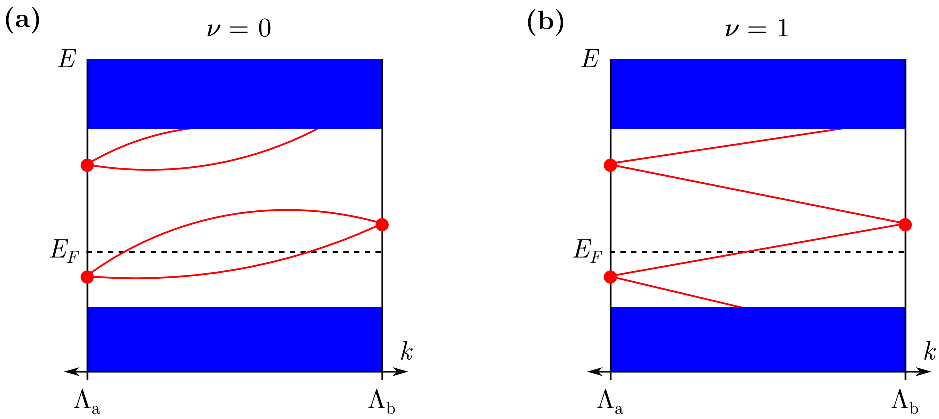

Figure 3.3: Schematic edge state spectra between the time-reversal invariant momenta Λ_a and Λ_b of the edge BZ. The blue regions represent the two bulk continua which are separated by an energy gap. Possible allowed edge state dispersions are shown in red. Kramers doublets at the time-reversal invariant momenta are highlighted by red dots. Note that for the topologically nontrivial phase in (b) the edge band traverses the bulk energy gap whereas this is not the case for the trivial phase in (a).

time-reversal symmetry. Particularly, the QSHI is characterized by the nontrivial value $\nu = 1$. Using Eq. (3.8), it can be written more elegantly as

$$(-1)^{\nu} = \prod_{i=1}^{4} \frac{\sqrt{\det[w(\Gamma_i)]}}{\mathrm{Pf}[w(\Gamma_i)]}, \tag{3.10}$$

where Γ_i are the four time-reversal invariant points $(0,0)$, $(\pi,0)$, $(0,\pi)$, and (π,π). Remember that this formula is only valid if the $|u_{kn}\rangle$ are chosen to be continuous throughout the entire BZ. This is always possible for a system with time-reversal symmetry since its Chern number must be zero, as we have seen in the previous section. If the system has also inversion symmetry, Eq. (3.10) can be simplified and expressed in terms of the parities $\xi_{2m}(\Gamma_i)$ of the N occupied Kramers pairs[17] at the time-reversal invariant points [40]

$$(-1)^{\nu} = \prod_{i=1}^{4} \prod_{m=1}^{N} \xi_{2m}(\Gamma_i). \tag{3.11}$$

Moreover, Fu and Kane established a connection between the value of the $\mathbb{Z}_2$ invariant and the spectrum of edge states for the considered time-reversal invariant system [40]. The edge BZ of a time-reversal invariant system has two inequivalent time-reversal invariant

---

[17] Note that two Kramers-degenerate states have the same parity.

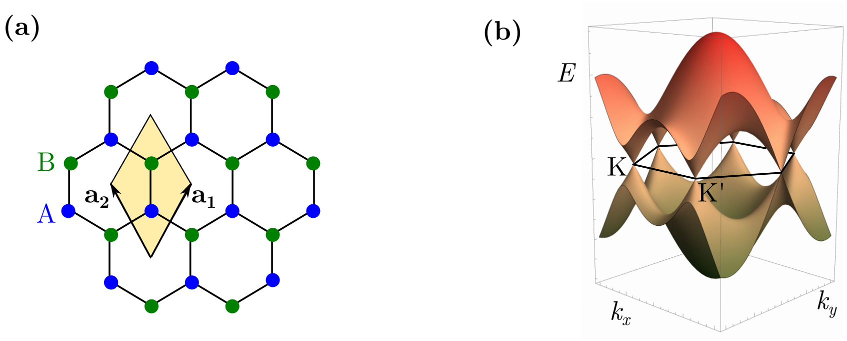

Figure 3.4: (a) Graphene honeycomb lattice: the unit cell (beige) is spanned by the two primitive lattice vectors $\mathbf{a}_1$ and $\mathbf{a}_2$, and consists of two lattice sites A (blue sites) and B (green sites). (b) Bulk band structure of graphene in the hexagonal BZ: the two bulk bands touch at momenta K and K′ around which the dispersion is given by a 2D Dirac cone.

momenta Λ_a and Λ_b. Any edge state at these momenta must be part of a degenerate Kramers doublet. In between Λ_a and Λ_b, the doublet degeneracy is lifted since the time-reversed partner is at the opposite momentum in the edge BZ. It is easy to imagine that there are numerous ways to connect the Kramers doublets to each other and/or with the bulk continuum. However, there are only two qualitatively distinct spectra of edge states, which are illustrated in Fig. 3.3. In particular, if we place the Fermi level inside the bulk energy gap, there are either an *odd* or an *even* number of edge states crossing the Fermi level between Λ_a and Λ_b. An even number of crossings can always be removed leading to an insulating edge. This corresponds to a trivial insulator with $\nu = 0$. On the other hand, if there is an odd number of crossings, all crossings can be gapped except one. Therefore, the existence of at least *one* edge state in half of the edge BZ is a topologically protected feature. Obviously, this case corresponds to the QSHI phase with $\nu = 1$. Note that with each edge state at the Fermi level between Λ_a and Λ_b there is another time-reversed Kramers partner in the other half of the edge BZ. Hence, ν distinguishes between an even and an odd number of edge Kramers pairs at the Fermi level.

Kane-Mele model for quantum spin-Hall insulators

In the previous section, we discussed how two construct a QSHI model by taking two time-reversed copies of a quantum anomalous Hall insulator. We also mentioned that, in realistic systems, the requirements on the internal magnetic fluxes seen by the two spin channels can only be met by strong SOC. Kane and Mele predicted that these ingredients are naturally provided in graphene [76].

Graphene is a single layer of graphite in which carbon atoms are arranged on a 2D honeycomb lattice with a two-site unit cell [13] (sublattices A and B) as is illustrated in Fig. 3.4(a). If SOC is neglected, the system can effectively be described by a two-band nearest-neighbor tight-binding model for the π electrons. The two bulk energy bands only touch at two isolated points, namely at K and K', in the hexagonal BZ rendering graphene a zero-gap semiconducting material [see Fig. 3.4(b)]. Moreover, the low-energy theory of graphene around the two band touching points is given by a relativistic 2D Dirac equation.

Kane and Mele found that the only symmetry-allowed SOC terms in graphene open a small bulk energy gap which is topologically nontrivial. The SOC in graphene preserves spin-rotation symmetry around the z axis. Thus, S^z is a good quantum number and the system decomposes into two independent spin channels. Remarkably, each spin channel realizes a QAHE on its own with nontrivial but opposite Chern numbers $n_{\uparrow,\downarrow} = \pm 1$ [76]. Hence, graphene with SOC is a QSHI with $\nu = 1$. Kane and Mele also considered a spin-symmetry breaking Rashba term, which can arise due to a perpendicular electric field or interaction with a substrate. In this case, $n_{\uparrow,\downarrow}$ are no longer well defined but ν retains its nontrivial value as long as the Rashba term is sufficiently small.

The full Kane-Mele model reads [74, 76]

$$\begin{aligned}\mathcal{H}_{\mathrm{KM}} &= t \sum_{\langle \mathbf{i},\mathbf{j}\rangle,\sigma} c^\dagger_{\mathbf{i}\sigma} c_{\mathbf{j}\sigma} + i\lambda_{\mathrm{SO}} \sum_{\langle\langle \mathbf{i},\mathbf{j}\rangle\rangle,\sigma\sigma'} \nu_{\mathbf{ij}}\, c^\dagger_{\mathbf{i}\sigma} s^z_{\sigma\sigma'} c_{\mathbf{j}\sigma'} \\ &+ i\lambda_{\mathrm{R}} \sum_{\langle \mathbf{i},\mathbf{j}\rangle,\sigma\sigma'} c^\dagger_{\mathbf{i}\sigma} (\mathbf{s}\times\hat{\mathbf{d}}_{\mathbf{ij}})^z_{\sigma\sigma'} c_{\mathbf{j}\sigma'} + \lambda_\nu \sum_{\mathbf{i}\sigma} \xi_{\mathbf{i}}\, c^\dagger_{\mathbf{i}\sigma} c_{\mathbf{i}\sigma}. \end{aligned} \tag{3.12}$$

The first term describes nearest-neighbor hopping. The second term is S^z-preserving spin-dependent second-neighbor hopping with $\nu_{\mathbf{ij}} = (2/\sqrt{3})(\hat{\mathbf{d}}_1 \times \hat{\mathbf{d}}_2)^z = \pm 1$, where $\hat{\mathbf{d}}_1$ and $\hat{\mathbf{d}}_2$ are unit vectors along the two bonds the electron traverses while going from site $\mathbf{j}$ to $\mathbf{i}$. $\hat{\mathbf{d}}_{\mathbf{ij}}$ is a unit vector pointing from lattice site $\mathbf{j}$ to $\mathbf{i}$. λ_R parameterizes the S^z-breaking Rashba term, which also breaks $z \to -z$ mirror symmetry. Finally, the model also takes into account a staggered sublattice potential parameterized by λ_ν which breaks inversion symmetry in the plane. Note that the s^i with $i = x, y, z$ are Pauli matrices associated with the spin degree of freedom of the electrons.

Unfortunately, it turned out that the SOC in graphene is too small to create a sizable gap[18]. Hence, the predicted QSHE in pristine graphene has never been observed. Nonetheless, recent experimental progress in the preparation of other graphene-like materials has brought the Kane-Mele model back into focus. In particular, single layers of materials like silicon, germanium or tin are promising candidates to realize the QSHE [78–82]. They are in the same group of the periodic table as carbon and are therefore expected to have similar structural properties. Furthermore, since the SOC strength scales like Z^4, where Z is the atomic number, their SOC-induced energy gap is much larger, such that their QSHE could potentially be observed. In particular, stanene, a monolayer of tin, has a SOC gap of approximately 0.3 eV, which is, in principle, sufficiently large for practical applications at room temperature [83].

---

[18] First-principles calculations compute a spin-orbit gap of the order of 10^{-3} meV [77].

3.1.3 Topological insulators in three dimensions

The concept of the QSHI in 2D can be extended also to three dimensions (3D). This is already apparent from the Altland-Zirnbauer table (see Sec. 2.1.2), which tells us that 3D insulators in symmetry class AII are subject to a $\mathbb{Z}_2$ classification. However, as we will see in this section, the family of $\mathbb{Z}_2$ insulators in three dimensions is much more diverse than their relatives in two dimension.

Topological invariants for three-dimensional insulators with time-reversal symmetry

The BZ of a 3D system has eight time-reversal invariant points, as compared to four in two dimensions. These points can be expressed in terms of primitive reciprocal lattice vectors $\mathbf{b}_i$ as [84]

$$\Gamma_{i=(n_1 n_2 n_3)} = \frac{1}{2}(n_1\mathbf{b}_1 + n_2\mathbf{b}_2 + n_3\mathbf{b}_3), \tag{3.13}$$

where $n_j = 0, 1$. We can visualize these points as the vertices of a cube as shown in Fig. 3.5(a). Moreover, by continuously transforming the reciprocal lattice vectors $(\mathbf{b}_1, \mathbf{b}_2, \mathbf{b}_3)$ into the orthonormal basis $(\mathbf{e}_1, \mathbf{e}_2, \mathbf{e}_3)$ we can always map any 3D BZ to a unit cube without changing the topology of the system. To simplify the discussion, we therefore present the following arguments based on a cubic BZ only [84].

We readily see that any plane going through any four of the time-reversal invariant points represents a time-reversal invariant 2D system. Thus, each of these planes is characterized by a $\mathbb{Z}_2$ invariant ν given by

$$(-1)^{\nu} = \prod_{i=1}^{4} \delta_i, \quad \text{with } \delta_i = \frac{\sqrt{\det[w(\Gamma_i)]}}{\mathrm{Pf}[w(\Gamma_i)]}. \tag{3.14}$$

These invariants characterize the topology of the 3D system because they give restrictions on the number of surface Kramers pairs in the surface-BZ projections of these planes.

Obviously, there are plenty of possibilities to connect four time-reversal invariant points using planes. However, their associated $\mathbb{Z}_2$ invariants are not independent [67,84,85]. One way of choosing an independent set of planes is to first consider the six faces of the cube shown in Fig. 3.5(a). Since the system is gapped throughout the 3D BZ, a homotopy argument can be used to show that all opposing faces have either the same or different invariants[19] [67,85]. Hence, there are *four* independent $\mathbb{Z}_2$ invariants that characterize a time-reversal invariant insulator in three dimensions. The common choice of invariants goes back to Fu, Kane and Mele [84]. They are typically denoted as $\nu_0;(\nu_1\nu_2\nu_3)$ and defined as follows

$$(-1)^{\nu_0} = \prod_{n_j=0,1} \delta_{n_1 n_2 n_3}, \tag{3.15}$$

$$(-1)^{\nu_{i=1,2,3}} = \prod_{\substack{n_{j\neq i}=0,1\\ n_i=1}} \delta_{n_1 n_2 n_3}. \tag{3.16}$$

The so-called *weak* invariants [40,84] ν_1, ν_2, and ν_3 correspond to the two-dimensional $\mathbb{Z}_2$ invariants of the faces with $k_x = 1$, $k_y = 1$, and $k_z = 1$, respectively. Apparently, their values depend on the choice of the primitive reciprocal lattice vectors. Nevertheless, the corresponding phase can be uniquely identified with a modulo 2 reciprocal-lattice vector

$$\mathbf{G}_\nu = \nu_1\mathbf{b}_1 + \nu_2\mathbf{b}_2 + \nu_3\mathbf{b}_3. \tag{3.17}$$

The so-called *strong* invariant [40,84] ν_0 is the product of the δ_i at all time-reversal invariant points Γ_i. Thus, ν_0 does not depend on the choice of the reciprocal lattice vectors. Furthermore, we readily see from its definition that the value of ν_0 is equal to the difference of $\mathbb{Z}_2$ invariants of any pair of opposing time-reversal invariant planes.

Strong and weak topological insulators

In total, there are 16 topologically distinct phases. The phases with $\nu_0 = 1$ are called *strong topological insulators* [84], whereas phases with $\nu_0 = 0$ but $\nu_i \neq 0$ for at least one $i \in \{1, 2, 3\}$ are called *weak topological insulators* [84]. The latter are dubbed "weak" because the weak invariants $(\nu_1\nu_2\nu_3)$ are not robust against translational-symmetry breaking perturbations. In particular, a weak topological insulator (TI) can be turned into a trivial insulator in this way. This, on the other hand, is not possible for a strong TI since ν_0 is

---

[19] This is no longer the case if there are gapless points in the BZ as we will discuss in Chapter 5.

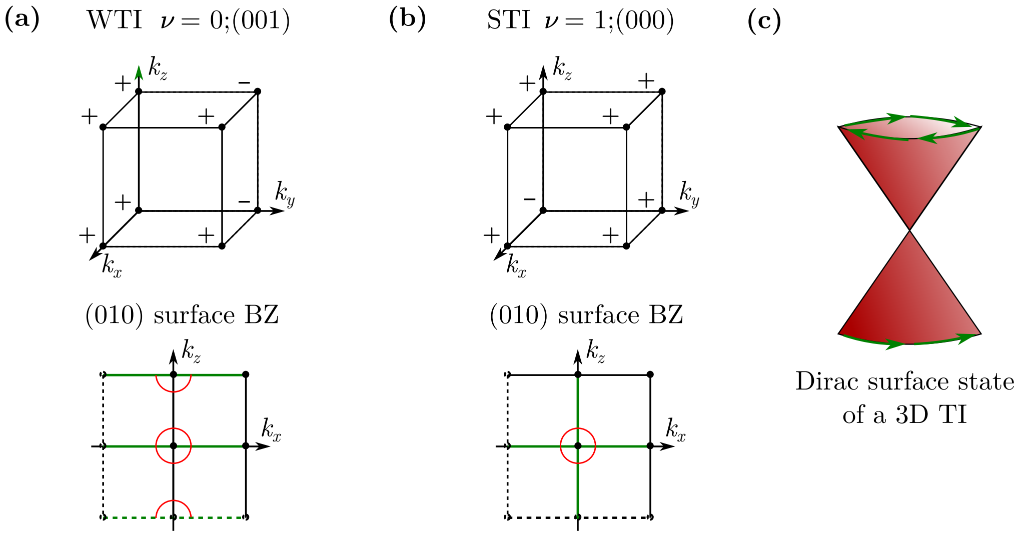

Figure 3.5: Panels (a) and (b) show the cube formed by the eight time-reversal invariant momenta, indicated by black dots, in a 3D BZ. Exemplary values (+1 or −1) of δ_i at those points are shown for a weak topological insulator in (a), and for a strong topological insulator in (b). Also shown are the corresponding surface BZs for systems with (010) terminations. Projections of nontrivial time-reversal invariant planes are highlighted in green. Exemplary surface Fermi surfaces, compatible with the topological invariants, are shown in red. Typically, the Fermi surface consists of Fermi pockets associated with a surface Dirac cone. A surface Dirac cone dispersion is pictorially shown in panel (c). The green arrows indicate the spin direction which is locked to the momentum of the states.

robust against any time-reversal preserving perturbation that does not close the energy gap.

The values of the $\mathbb{Z}_2$ invariants have important implications on the structure of surface states [40, 84]. The surface BZ of a time-reversal invariant system in three dimensions has four inequivalent time-reversal invariant points. Due to Kramers theorem, any generic band crossing of surface states at these points is a 2D Dirac point with a Dirac-cone dispersion [see Fig. 3.5(c)]. Remarkably, in the vicinity of the Dirac point, the spin of the electronic surface states is locked to their momentum, which is commonly referred to as *spin-momentum locking* [3, 86]. The $\mathbb{Z}_2$ invariants determine how the Dirac points at different time-reversal invariant points are connected to each other or to the bulk continuum. More specifically, they determine the number (even or odd) of surface Kramers pairs in the surface projections of the corresponding time-reversal invariant planes.

For strong TIs this leads to the generic presence of a *single* surface Dirac cone around one of the time-reversal invariant points of the surface BZ [40,84] which is shown in Fig. 3.5(b). Most importantly, a topologically protected surface Dirac cone has to be present for *any* termination of the system. This is a remarkable feature because Dirac fermions usually come in pairs according to the fermion doubling theorem [87, 88]. In strong TIs, this apparent contradiction is resolved by the presence of the opposite surface. Strong TIs have been the subject of numerous experimental and theoretical studies due to their exotic properties, such as the half-integer QHE on their surface [22] or the Josephson-Witten effect [89], and due to the growing number of materials, such as Bi_2Te_3 or Bi_2Se_3 [90–93].

Weak TIs are qualitatively different from their strong counterparts. First of all, the arrangement of their $\mathbb{Z}_2$ invariants leads to the generic presence of *two* surface Dirac cones [40, 84], which are centered around different time-reversal invariant points in the surface BZ [see Fig. 3.5(a)]. However, this is not true for all terminations of the system. There are certain surfaces, the so-called “dark” surfaces, which do not exhibit protected surface states. These are surfaces whose Miller indices are identical to the vector $\mathbf{G}_\nu$ spanned by the weak indices modulo 2. This can be understood by realizing that a weak TI is equivalent to a multilayer of 2D QSHIs stacked in the direction of $\mathbf{G}_\nu$. On the side surfaces of a stacked QSHI system, the collection of 1D edge states will form the 2D surface Dirac states. They will occur around time-reversal invariant momenta which can be connected by $\mathbf{G}_\nu/2$. The top and bottom surfaces, however, consist of QSHI layers which are gapped by definition. Hence, the top and bottom surfaces do not accommodate nontrivial surface states and are in this sense “dark”.

In contrast to strong TIs, surface states of weak TIs are not robust in the presence of generic time-reversal preserving disorder. The reason is that translational-symmetry breaking perturbations can couple Dirac states at different time-reversal invariant momenta leading to a gap opening [94]. However, it has been shown that the presence of Dirac states is robust if translational symmetry is preserved on average [95, 96].

Although the stacking of 2D QSHIs to build 3D weak topological insulators is a promising recipe, the preparation of weak TIs has so far been challenging. Nonetheless, the material $Bi_{14}Rh_3I_9$ has recently been verified to realize a weak TI [97, 98] and also other candidate materials have been put forward [93, 99].

3.2 Dirac line degeneracies in topological insulators

In the previous section, we have seen that the hallmark of 3D topological insulators is the presence of topologically protected *two-dimensional* Dirac cones on their surfaces.

However, an experimental work by Gibson *et al.* [100] suggests that 3D TIs can also exhibit Dirac-like *line* degeneracies on their surfaces corresponding to effectively 1D Dirac electrons. By angle-resolved photoemission spectroscopy (ARPES) they established the presence of highly anisotropic surface states on the (113) surface of $\mathrm{Ru_2Sn_3}$, which show an almost line-like dispersion along certain high-symmetry directions.

Dirac line degeneracies have been studied in the context of topological semimetals, where the degeneracies appear in the bulk band structure of the materials [101–103]. However, 1D Dirac states have not been investigated in the context of surface states of 3D topological insulators. The first question that arises is whether and under what circumstances TIs can exhibit Dirac-like line degeneracies on their surface, and, secondly, whether they are protected by any kind of symmetry.

As we will see in the following, weak TIs are the most promising candidates to realize such Dirac line degeneracies on their surface. To see this, let us use the following thought experiment in which we will build a weak TI starting from a QSHI.

First of all, let us consider a stack of arbitrary but identical 2D TIs where the stacking direction is, without loss of generality, the z direction. Furthermore, let the system be finite in a direction perpendicular to the stacking direction, e.g., the x direction. Generically, each of the 2D TI ribbons will have topologically protected edge states inside the bulk energy gap with an edge Kramers doublet at a TRI point [74, 75]. Let us first inspect the case where the layers are completely decoupled and the band structure of the system does not disperse in the k_z direction. Thus, the Kramers doublet of the 1D BZ of the layers become perfectly flat line degeneracies, more precisely Dirac lines, in the surface BZ of the stack. With this stacking procedure we have constructed a weak TI with $\mathbb{Z}_2$ indices $(\nu_0; \nu_1\nu_2\nu_3) = (0; 001)$ [40, 84], and with Dirac lines instead of Dirac points on its surfaces. This is not surprising since the stack of 2D TIs is still an effectively 2D system. Generally, one would expect the Dirac lines to break up and leave only Dirac points at TRI momenta once an arbitrary time-reversal invariant interlayer coupling is introduced. This, in turn, leads to a typical surface band dispersion of a weak TI with an even number of surface Dirac cones [84].

In the following we will show that this is not necessarily the case and that the presence of “in-plane time-reversal invariance” leads to topologically protected Dirac lines even in the full 3D system with coupled layers. Moreover, we will show that this is not possible for strong TIs making 1D Dirac states an exclusive feature of weak TIs. The work presented in the following is based on Ref. [104].

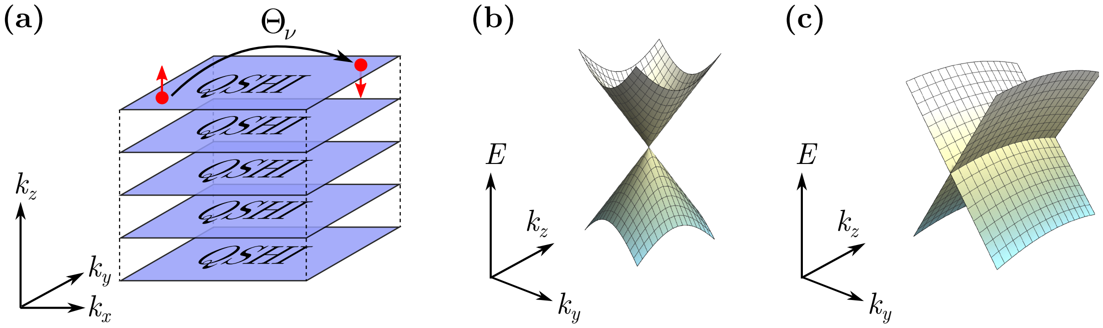

Figure 3.6: (a) Illustration of the in-plane time-reversal operator Θ_ν in momentum space: the operator flips the spin of an electron and reverses the momentum component parallel to the plane defined by the weak indices $\nu = (\nu_1, \nu_2, \nu_3)$. As demonstrated, a weak TI with Θ_ν symmetry represents a QSHI for any fixed k_z. This gives rise to topologically protected Dirac edge states associated with each layer. (b) Typical dispersion of a 2D Dirac electron on the surface of a TI. (c) Typical dispersion of a 1D Dirac electron on the surface of a weak TI with Θ_ν symmetry.

3.3 In-plane time-reversal invariance

We introduce in-plane time-reversal invariance as the 2D analogue of the *conventional* time-reversal symmetry with respect to a specific plane Π [see Fig. 3.6(a)]. The corresponding antiunitary operator Θ_Π acts similarly to its 3D analogue except that the momentum component perpendicular to the plane Π remains unchanged. Without loss of generality, we choose the plane to be (001). Then, the in-plane time-reversal operator for spin-$\frac{1}{2}$ particles reads

$$\Theta_{(001)} := i(\mathbb{1} \otimes s^y)K \text{ with } k_x, k_y, k_z \to -k_x, -k_y, k_z. \tag{3.18}$$

Here, s^y acts on the spin part of the system, where again, without loss of generality, we have chosen S^z as the quantization axis of spin and the Pauli matrices as a spin representation. The identity matrix $\mathbb{1}$ acts in the space spanned by additional degrees of freedom, such as orbital or sublattice degrees of freedom. Note that $\Theta_{(001)}$ has the same operator structure as the conventional time-reversal operator Θ. Obviously, for a 2D system $\Theta_{(001)}$ and Θ are identical. When dealing with a weak TI with weak indices $\nu = (\nu_1, \nu_2, \nu_3)$, we denote the in-plane time-reversal operator associated with the (ν_1, ν_2, ν_3) plane by Θ_ν.

Since both types of time-reversal operators appear to be very similar, one expects the existence of an analogue of Kramers' theorem for the in-plane time-reversal symmetric system. To establish this, recall that a time-reversal symmetric system satisfies

$\Theta H(k_x, k_y, k_z)\Theta^{-1} = H(-k_x, -k_y, -k_z)$, i.e., the Bloch Hamiltonian commutes with Θ at TRI points where $(k_x, k_y, k_z) \simeq (-k_x, -k_y, -k_z)$. For particles with half-integer spin, this implies Kramers' theorem [3]. For an in-plane time-reversal symmetric system, we have instead

$$\Theta_{(001)} H(k_x, k_y, k_z)\Theta_{(001)}^{-1} = H(-k_x, -k_y, k_z). \tag{3.19}$$

Hence, for particles with half-integer spin the energy spectrum must be at least two-fold degenerate along *in-plane time-reversal invariant lines* satisfying $(k_x, k_y, k_z) = (-k_x, -k_y, k_z)$. This gives rise to *Kramers lines* along which Kramers-like degeneracies are guaranteed and topologically protected by $\Theta_{(001)}$ invariance. Furthermore, a Kramers line always connects two Kramers points in the BZ because the condition above includes also the 8 TRI points.

By bulk-boundary correspondence, one generically finds topologically protected Dirac lines on surfaces perpendicular to the stacking direction. The Dirac lines resemble the dispersion of a 1D Dirac electron in a 2D space: along one direction, it shows the typical linear Dirac dispersion whereas the dispersion is line-like in the perpendicular direction. This is illustrated in Fig. 3.6(c). If Θ_ν is broken without breaking conventional time-reversal symmetry, only degeneracies at the Kramers points in the BZ are still topologically protected. Therefore, each Dirac line splits and the associated 1D Dirac electron decays into two 2D Dirac electrons.

It is precisely for this reason that topologically protected Dirac lines cannot exist in strong TIs. Consider a strong TI with one Dirac point and without any in-plane time-reversal symmetry. For a strong TI, it is always possible to reduce the number of Dirac points to one by introducing suitable translational-symmetry breaking and surface potential terms. Now, choose an arbitrary plane (klm) with respect to which we are going to establish the corresponding Θ_{klm} symmetry. We know that the single Dirac point of the strong TI must be connected to the bulk continuum along any line that will later become a Kramers line once in-plane time-reversal symmetry has been established. Otherwise, there would have to be a second Dirac point at the opposite TRI momentum and the system would not be a strong TI. In the process of establishing Θ_{klm} symmetry, the "arms" of the Dirac point, therefore, pull down the bulk bands to which they are attached and thereby close the bulk energy gap. Thus, the final system with in-plane time-reversal symmetry cannot be an insulator but either becomes a semimetal or a metal. For this reason, the presence of in-plane time-reversal symmetry, which is essential for the appearance of Dirac lines, is not reconcilable with a strong TI. A demonstration of this feature will be shown explicitly in Sec. 3.5.

There is another appealing point of view which illustrates the connection between in-plane time-reversal symmetry and Dirac lines in weak TIs. For this, consider a weak TI with weak indices (001) such that the associated stacking direction is the z direction. Furthermore, let us treat k_z in the corresponding Hamiltonian $H(k_x, k_y; k_z)$ as a parameter. If further in-plane time-reversal symmetry $\Theta_{(001)}$ is present, we conclude that the system realizes a 2D QSHI for any value of the parameter k_z [see Fig. 3.6(a)]. This can be seen as follows. First, this is clearly the case for $k_z = 0$ and $k_z = \pi$ since the system obeys conventional time-reversal symmetry and is topologically non-trivial. However, as we move along k_z the 2D systems always preserve time-reversal symmetry in the 2D sense due to the presence of in-plane time-reversal symmetry in the full 3D system. Moreover, the bulk gap does not close. Therefore, a topological phase transition does not occur and the collection of 2D systems stay in the QSHI phase for all k_z. This also implies that any such 2D QSHI will have topologically protected (spin-filtered) edge states that form Kramers doublets at the TRI momenta of the 1D BZ. When we now move along k_z, the Kramers degeneracies remain intact, which implies the existence of Dirac lines along in-plane TRI lines in the surface BZ of the weak TI.

Moreover, it is possible to associate a ”line” of topological invariants with an insulator respecting in-plane time-reversal symmetry. Indeed, for each value of the momentum k_z we can define a 2D topological $\mathbb{Z}_2$ invariant $\nu(k_z)$ [75] which does not change as we move along k_z. Hence, the line of topological invariants can only assume two constant values: $\nu(k_z) = 0$ for a trivial insulator, and $\nu(k_z) = 1$ for an in-plane time-reversal invariant weak TI hosting 1D Dirac electrons on its surfaces.

3.4 Stacked Kane-Mele model

Having established the general consequences of in-plane time reversal invariance, we are now going to apply our results to stacked Kane-Mele systems. We have introduced the Kane-Mele model [74, 76] in Sec. 3.1.2. It is known to be a realization of a 2D TI in certain parameter ranges. Based on this 2D model, we can construct a 3D system by stacking the Kane-Mele layers along the z direction. This is done in such a way that corresponding lattice points of the same sublattice but from different layers lie on top of each other [AA stacking, see Fig. 3.7(a)]. In order to couple the layers, we introduce a nearest-neighbor interlayer hopping term and an interlayer SOC term. This leads us to the model Hamiltonian

$$\mathcal{H} = \sum_{l} \mathcal{H}_{\mathrm{KM},l} + \tau \sum_{\langle l,l' \rangle} \sum_{\mathbf{i}\sigma} c^{\dagger}_{\mathbf{i}l\sigma} c_{\mathbf{i}l'\sigma} + i\lambda_{\mathrm{SO},\perp} \sum_{\langle l,l' \rangle} \sum_{\mathbf{i}\sigma\sigma'} \mu_{ll'}\, c^{\dagger}_{\mathbf{i}l\sigma} s^{z}_{\sigma\sigma'} c_{\mathbf{i}l'\sigma'}, \tag{3.20}$$

where l indexes the layers, and $\mu_{ll'} = \pm 1$ for $l \gtrless l'$. Note that after a Fourier transformation the corresponding Bloch Hamiltonian $H(\mathbf{k})$ is a 4×4 matrix which can be expanded in terms of Dirac matrices and their commutators similar to Ref. [74]. Furthermore, these matrices can be written as Kronecker products of Pauli matrices τ^i in sublattice space and Pauli matrices s^i in spin space. In this way, the interlayer terms of the Hamiltonian become

$$\begin{aligned} H_{ih}(\mathbf{k}) &= 2\tau \cos k_z \,(\mathbb{1} \otimes \mathbb{1}), & (3.21)\\ H_{\mathrm{SO},\perp}(\mathbf{k}) &= -2\lambda_{\mathrm{SO},\perp} \sin k_z \,(\mathbb{1} \otimes s^z), & (3.22) \end{aligned}$$

where the interlayer distance has been set to unity. The intralayer terms of the Kane-Mele Bloch Hamiltonian are [74]

$$\begin{aligned} H_{\mathrm{KM}}(\mathbf{k}) = {} & t(1 + 2\cos x \sin y)\,(\tau^z \otimes \mathbb{1}) + 2t \cos x \sin y\,(\tau^y \otimes \mathbb{1}) \\ & + \lambda_{\mathrm{SO}}(2 \sin 2x - 4 \sin x \cos y)\,(\tau^z \otimes s^z) + \lambda_R(1 - \cos x \cos y)\,(\tau^y \otimes s^x) \\ & + \lambda_R \cos x \sin y\,(\tau^x \otimes s^x) - \sqrt{3}\lambda_R \sin x \cos y\,(\tau^y \otimes s^y) \\ & - \sqrt{3}\lambda_R \sin x \cos y\,(\tau^x \otimes s^y) + \lambda_\nu\,(\tau^z \otimes \mathbb{1}), \end{aligned} \tag{3.23}$$

where $x = k_x a/2$ and $y = \sqrt{3}k_y a/2$, with a being the distance between A and B sites. The parameters t, λ_{SO}, λ_R, and λ_ν parameterize nearest-neighbor hopping, S^z-conserving in-plane SOC, S^z-breaking Rashba SOC, and a staggered sublattice potential, respectively [see also Eq. (3.12)]. The relevant in-plane time-reversal operator for this model is $\Theta_{(001)} = i(\mathbb{1} \otimes s^y)K$ with $(k_x, k_y, k_z) \to (-k_x, -k_y, k_z)$.

In particular, we are going to study surface states for a slab of thickness W with (010) surfaces, where W is the number of bulk unit cells per supercell. The surfaces cut out zigzag-shaped edges from each Kane-Mele layer [see Fig. 3.7(a)]. In other words, we will investigate a stack of infinitely many Kane-Mele layers with zigzag termination. The corresponding Bloch Hamiltonian $H^{(010)}(k_x, k_z)$ of the slab is a $4W \times 4W$ matrix whose energies are obtained by exact diagonalization.

In Fig. 3.8, the band structure of the (010) Kane-Mele slab is shown along high-symmetry lines of the surface BZ for different model parameters. For now, we ignore the sublattice

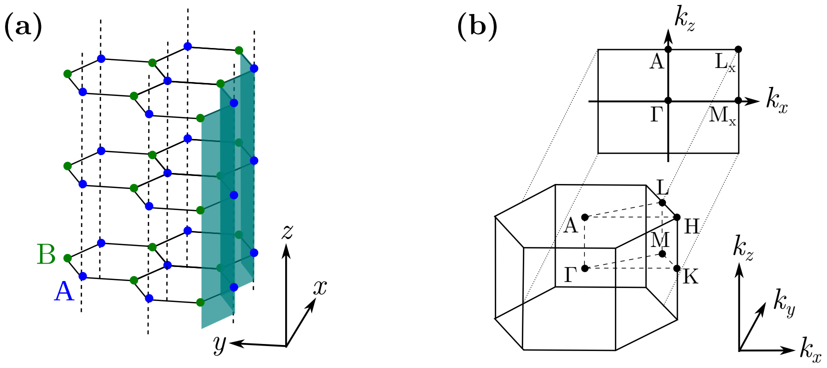

Figure 3.7: (a) Illustration of the lattice for the stacked Kane-Mele model: honeycomb layers are stacked in the z direction following an AA stacking pattern. The shaded zigzag surface represents the (010) termination studied in this chapter. (b) Bulk BZ and (010) surface BZ of the stacked Kane-Mele model with high-symmetry points and notations as used in this chapter.

potential term in H_{KM}. The effect of this term will be discussed at the end of this section. In addition, Fig. 3.9 also shows the corresponding bulk energy bands along high symmetry lines of the bulk BZ. The bulk BZ and the considered surface BZ are illustrated in Fig. 3.7(b).

In Fig. 3.8(a), only in-plane hopping and in-plane SOC are nonzero. For the chosen parameters the bulk spectrum exhibits an energy gap and we find surface states traversing the bulk gap. The band structures along $\overline{\Gamma M_x}$ and $\overline{L_x A}$ are identical to that of the 2D Kane-Mele model with zigzag edges and the same parameter values (see Ref. [105]). For each surface, there is one spin-filtered surface band emerging from the bulk. The bands meet at the TRI momenta M_x and L_x, respectively, where we find two-fold Kramers degeneracies which are topologically protected by conventional time-reversal symmetry. Along $\overline{M_x L_x}$ we find a two-fold line degeneracy of the topological bands: a Dirac line. This is easily explained in the light of in-plane time-reversal symmetry. With the chosen parameters, the 2D Kane-Mele model is a TI with a Dirac point at the M_x point of the surface BZ. Therefore, a stack of these systems forms a weak TI with $\mathbb{Z}_2$ indices $(\nu_0;\nu_1\nu_2\nu_3) = (0;001)$. Since Θ symmetry is preserved for the individual layers and the layers are not coupled, in-plane time-reversal symmetry $\Theta_{(001)}$ is automatically conserved for the stacked system and, thus, we find topologically protected Dirac lines. The Dirac line is flat because there is no dispersion along the k_z direction.

For Figs. 3.8(b)–(d), different terms are added to the Hamiltonian of the system one after the other. In Fig. 3.8(b), interlayer hopping has been included, which causes the band structure to disperse in the k_z direction. The bands, in particular the Dirac line, acquire a

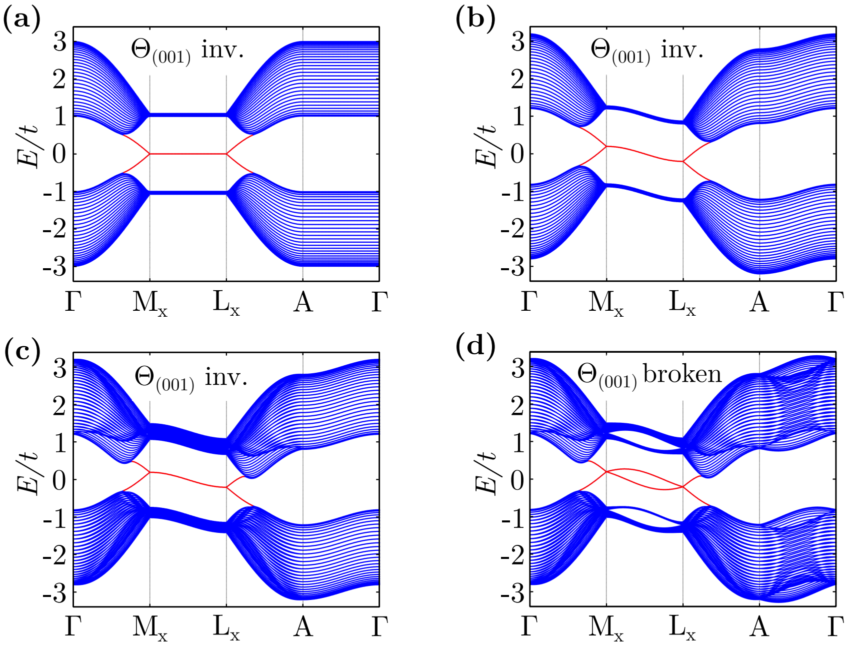

Figure 3.8: Energy bands for the stacked Kane-Mele model: bands of a (010) slab of width $W = 30$ are shown along high symmetry lines of the surface BZ for different model parameters (only nonzero parameters are listed in units of t): (a) $\lambda_{\mathrm{SO}} = 0.1$, (b) $\lambda_{\mathrm{SO}} = \tau = 0.1$, (c) $\lambda_{\mathrm{SO}} = \tau = \lambda_{\mathrm{R}} = 0.1$, (d) $\lambda_{\mathrm{SO}} = \tau = \lambda_{\mathrm{R}} = \lambda_{\mathrm{SO},\perp} = 0.1$. Surface states are highlighted in red. Note the Dirac line in panels (a)–(c) which is split into two Dirac points in panel (d) due to the breaking of $\Theta_{(001)}$ symmetry.

$\cos k_z$ dispersion since the interlayer hopping connects only adjacent layers. However, it is easy to check that the term preserves $\Theta_{(001)}$ symmetry. Therefore, the Dirac line remains topologically protected and we have found a truly 3D system that exhibits a 1D Dirac electron on its surface.

It is worth mentioning that the bands of the bulk spectrum [see Fig. 3.9(a)] are two-fold degenerate in the entire BZ due to the simultaneous presence of conventional time-reversal symmetry and inversion symmetry. For the surface bands of the slab, however, those symmetries only imply that corresponding surface states from *both* surfaces are degenerate. For line degeneracies on just *one* surface, in-plane time-reversal symmetry is essential as can easily be seen by adding an inversion-symmetry breaking term, e.g., in-plane Rashba SOC [see Fig. 3.8(c)]. It preserves in-plane time-reversal symmetry but breaks inversion symmetry as well as the remaining $U(1)$ spin symmetry. Hence, in the bulk spectrum the two-fold degeneracies are lifted except at the Kramers points and along the Kramers lines [see Fig. 3.9(b)]. Also on the surface, the degeneracy of the Dirac line is

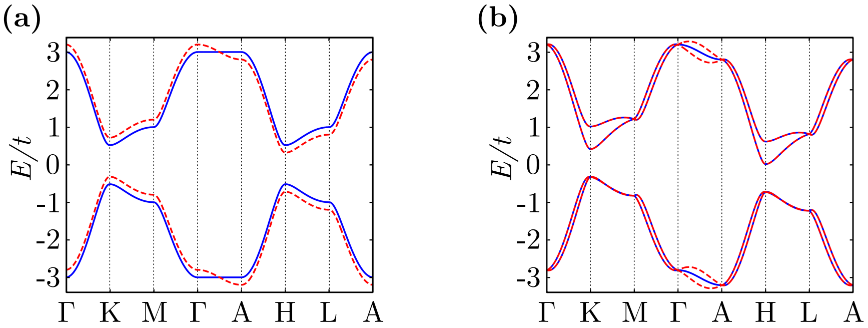

Figure 3.9: Bulk energy bands for the stacked Kane-Mele model along high symmetry lines of the BZ for different model parameters (only nonzero parameters are listed in units of t): (a) with inversion symmetry: $\lambda_{\mathrm{SO}} = 0.1$ (solid blue lines), $\lambda_{\mathrm{SO}} = \tau = 0.1$ (dashed red lines); (b) broken inversion symmetry: $\lambda_{\mathrm{SO}} = \tau = \lambda_{\mathrm{R}} = 0.1$ (solid blue lines), $\lambda_{\mathrm{SO}} = \tau = \lambda_{\mathrm{R}} = \lambda_{\mathrm{SO},\perp} = 0.1$ (dashed red lines).

not lifted as shown in Fig. 3.8(c). Interlayer SOC, however, breaks in-plane time-reversal symmetry while preserving its conventional counterpart. We observe that the effectively 1D Dirac electron decays into two 2D Dirac electrons, one at the M_x point and the other at the L_x point of the surface BZ, with a small shift in energy [see Fig. 3.8(d)].

So far, we have ignored the staggered sublattice potential term in H_{KM}. However, it is well known that such a mass term can result in a transition from a topological to a trivial insulator in the 2D Kane-Mele model [74, 76]. What happens to the Dirac line in the stacked system if we increase the mass? First of all, it is easy to check that the mass term preserves the relevant in-plane time-reversal symmetry. Therefore, the Dirac line cannot be destroyed in the process. But how can the surface states then be trivial in the trivial sector? The key is the closing of the bulk energy gap. Initially, the surface states are connected to both the upper and the lower bulk continuum. However, the process of closing and reopening the gap allows them to change this connectivity. In this way, the Dirac line remains intact but the surface states do no longer traverse the bulk energy gap and are, therefore, topologically trivial (see Fig. 3.10).

3.5 Cubic Liu-Qi-Zhang model

Let us now study in-plane time-reversal invariance in the context of another, more involved model, namely the cubic Liu-Qi-Zhang Hamiltonian [106]. It is derived from a model introduced by Zhang *et al.* [107], which has been successfully used to describe the $\mathrm{Bi_2Se_3}$

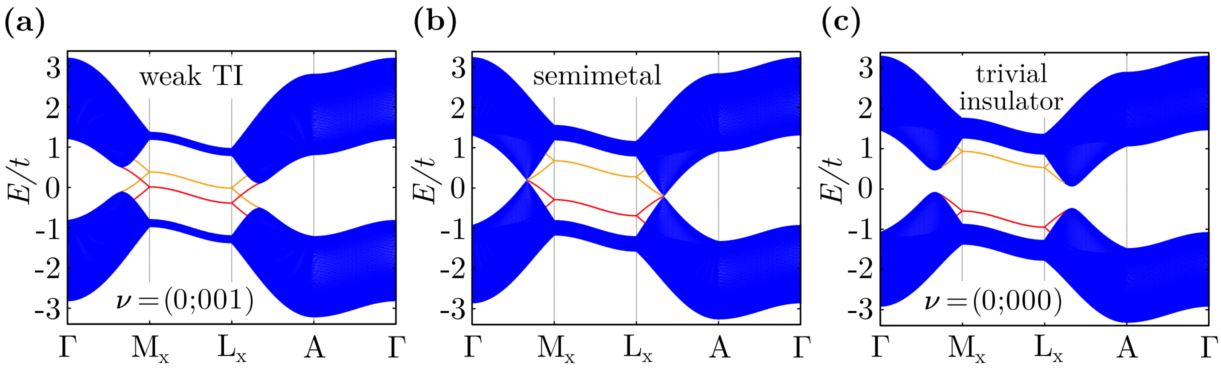

Figure 3.10: Energy bands for the stacked Kane-Mele model with $\Theta_{(001)}$ invariance: bands of a (010) slab of width $W = 80$ are shown along high symmetry lines of the surface BZ for different values of the mass term (in units of t): (a) $\lambda_\nu = 0.2$, (b) $\lambda_\nu = 0.52$, (c) $\lambda_\nu = 0.8$. The mass term does not break in-plane time-reversal invariance with respect to the xy plane. The only other nonzero model parameters are $\lambda_{\mathrm{SO}} = \tau = 0.1t$. Surface states are highlighted in red (left surface) and orange (right surface). Note the transition from a weak TI to a trivial insulator at $\lambda_\nu = 0.52$.

family of strong TIs. It is a 3D nearest-neighbor tight-binding model on a simple cubic lattice with two orbital and two spin degrees of freedom per site. The corresponding Hamiltonian in momentum representation is [106]

$$\mathcal{H} = \sum_{\mathbf{k}} \sum_{a,b=1}^{2} \sum_{\sigma\sigma'} H_{a\sigma,b\sigma'}(\mathbf{k})\, d^\dagger_{\mathbf{k}a\sigma} d_{\mathbf{k}b\sigma'}, \tag{3.24}$$

with the 4×4 Bloch Hamiltonian [106]

$$H(\mathbf{k}) = [M_0 + 6B - 2B \sum_{i=1}^{3} \cos k_i]\,\Gamma_5 + A \sum_{i=1}^{3} \Gamma_i \sin k_i. \tag{3.25}$$

Here, Γ_j denote the Dirac matrices $\Gamma_1 = s^x \otimes \sigma^x$, $\Gamma_2 = s^y \otimes \sigma^x$, $\Gamma_3 = s^z \otimes \sigma^x$, $\Gamma_5 = \mathbb{1} \otimes \sigma^z$, as introduced in Ref. [106]. The Dirac matrices are Kronecker products of Pauli matrices s^i in spin space and Pauli matrices σ^i in orbital space. The coordinate system used is aligned with the edges of the cubic unit cell and we write $\mathbf{k} = (k_1, k_2, k_3) \equiv (k_x, k_y, k_z)$. The model describes a trivial insulator for $M_0 > 0$ and $M_0 < -12$, a strong TI with $\mathbb{Z}_2$ indices $(1;000)$ or $(1;111)$ for $0 > M_0 > -4B$ or $-8B > M_0 > -12B$, and a weak TI with $\mathbb{Z}_2$ indices $(0;111)$ for $-4B > M_0 > -8B$ [106], where in all cases we have $A = B$. In particular, we are going to focus on the weak TI phase $(0;111)$. In this setup, we will study the surface states of a slab of thickness W with (001) surfaces. The corresponding

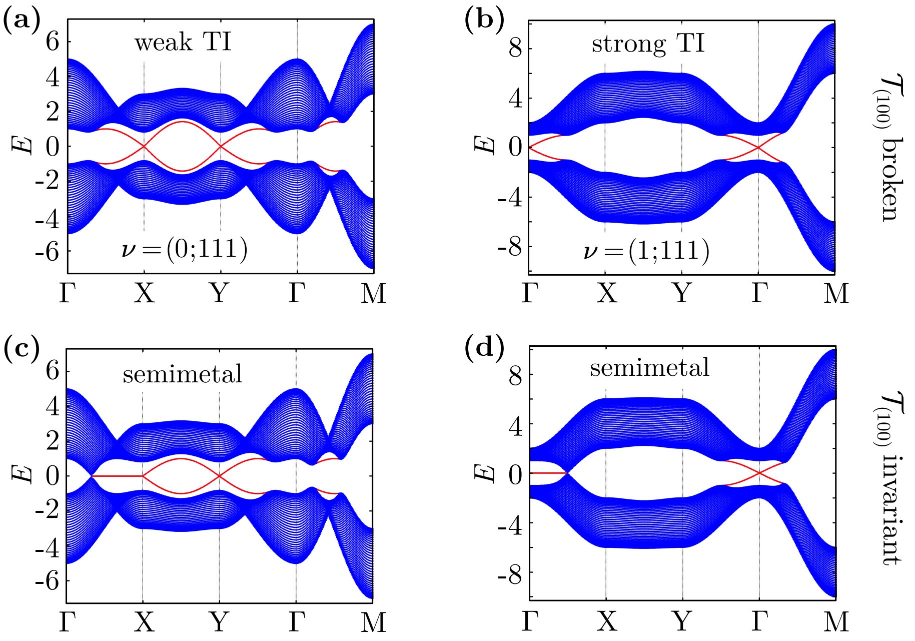

Figure 3.11: Energy bands for the cubic Liu-Qi-Zhang model: bands of a (001) slab of width $W = 40$ are shown along high symmetry lines of the surface BZ associated with the original cubic unit cell. The model parameters are $M_0 = -5.0$, $A = B = 1.0$ for panels (a), (c), and $M_0 = -2.0$, $A = B = 1.0$ for panels (b), (d). Shown are the band structures without (upper panels) and with (lower panels) in-plane time-reversal symmetry with respect to the yz plane. Surface states are highlighted in red.

Bloch Hamiltonian is a $4W \times 4W$ matrix and the band structures of the system are, as usual, obtained by exact diagonalization.

Let us first check the weak TI phase for in-plane time-reversal invariance with respect to the yz plane. The corresponding operator is

$$\Theta_{(100)} = i(s^y \otimes \mathbb{1})K \text{ with } k_x, k_y, k_z \to k_x, -k_y, -k_z. \tag{3.26}$$

It is easily verified that this symmetry is broken due to the $A \sin k_x \Gamma_1$ term in Eq. (3.25). In Fig. 3.11, it is demonstrated how the band structure of the system changes when the symmetry-breaking term is tuned to zero. We see that a two-fold degeneracy is established for surface states along $\overline{\Gamma X}$. However, the surface states are initially connected to the bulk along this line. For this reason, the bulk bands are pulled down resulting in a closing of the bulk energy gap. Hence, the system undergoes a semimetal transition as the in-plane time-reversal symmetry with respect to the yz plane is established. The same behavior can also be observed for the xz and the xy plane (not shown).

Nevertheless, by analogy with the stacked Kane-Mele model, we expect this weak TI, with $\mathbb{Z}_2$ invariants $(0;111)$, to develop Dirac lines without a semimetal transition if in-plane time-reversal symmetry with respect to the (111) plane – the plane described by the weak indices – is established. For convenience, we choose a different unit cell with a different coordinate system attached to it. Since a weak TI with weak indices (111) is topologically equivalent to a stack of 2D TIs stacked along the (111) direction, we are going to construct the new unit cell in this light (see Fig. 3.12).

The Z axis of the new coordinate system points along the (111) direction of the original coordinate system. We further align the c axis of the new unit cell with the new Z axis. Under these conditions, the new unit cell is hexagonal with a basis comprising three elements. The primitive lattice vectors of the new unit cell are $\mathbf{a}_1 = a(1,-1,0)$, $\mathbf{a}_2 = a(0,1,-1)$, $\mathbf{c} = a(1,1,1)$ with respect to the original coordinate system, and $\mathbf{a}_1 = \sqrt{2}a(1,0,0)$, $\mathbf{a}_2 = \sqrt{2}a(-1,\sqrt{3},0)$, $\mathbf{c} = a(0,0,1)$ with respect to the new rotated coordinates. The elements of the basis lie in different planes, where corresponding adjacent points are relatively shifted by a vector $\Delta = 1/3\,(-\mathbf{a}_1 + \mathbf{a}_2 + \mathbf{c})$, as indicated in Fig. 3.12.

After a Fourier transformation of Eq. (3.24) to position space, the model parameters can be translated to the new coordinate system. Another Fourier transformation back to momentum space then yields a new Bloch Hamiltonian $\tilde{H}(\mathbf{k})$. The new Hamiltonian is a 12×12 matrix due to the additional sublayer degrees of freedom A, B, C (see Fig. 3.12). As in Ref. [106], the spin and orbital parts of the Hamiltonian can be expanded in terms of Γ matrices. In addition, the sublayer part can be expanded in 3×3 Gell-Mann matrices [108] λ_i,

$$\lambda_1 = \begin{pmatrix} 0 & 1 & 0 \\ 1 & 0 & 0 \\ 0 & 0 & 0 \end{pmatrix}, \lambda_2 = \begin{pmatrix} 0 & -i & 0 \\ i & 0 & 0 \\ 0 & 0 & 0 \end{pmatrix}, \lambda_3 = \begin{pmatrix} 1 & 0 & 0 \\ 0 & -1 & 0 \\ 0 & 0 & 0 \end{pmatrix}, \lambda_4 = \begin{pmatrix} 0 & 0 & 1 \\ 0 & 0 & 0 \\ 1 & 0 & 0 \end{pmatrix}, \tag{3.27}$$

$$\lambda_5 = \begin{pmatrix} 0 & 0 & -i \\ 0 & 0 & 0 \\ i & 0 & 0 \end{pmatrix}, \lambda_6 = \begin{pmatrix} 0 & 0 & 0 \\ 0 & 0 & 1 \\ 0 & 1 & 0 \end{pmatrix}, \lambda_7 = \begin{pmatrix} 0 & 0 & 0 \\ 0 & 0 & -i \\ 0 & i & 0 \end{pmatrix}, \lambda_8 = \frac{1}{\sqrt{3}} \begin{pmatrix} 1 & 0 & 0 \\ 0 & 1 & 0 \\ 0 & 0 & -2 \end{pmatrix}, \tag{3.28}$$

and the corresponding unit matrix I. The components of the crystal momentum $\mathbf{k}$ with respect to the rotated coordinate system are denoted by k_X, k_Y, k_Z. With this, the Bloch Hamiltonian becomes

$$\tilde{H} = \tilde{H}_0 \otimes \Gamma_5 + \frac{A}{2} \sum_{i=1}^{3} \tilde{H}_i \otimes \Gamma_i, \tag{3.29}$$

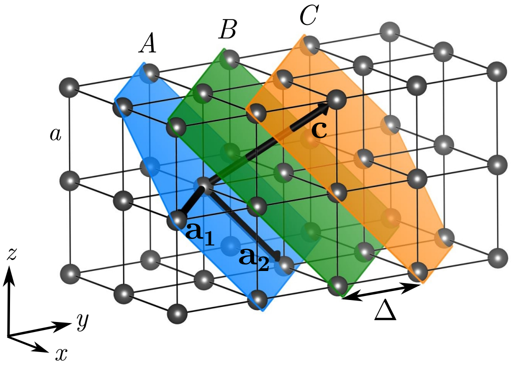

Figure 3.12: Alternative description of the lattice in the cubic Liu-Qi-Zhang model: highlighted are the three inequivalent layers A, B, C of the new hexagonal unit cell. Within the layers, the hexagonal structure of the basal plane is clearly visible. Also shown are the new primitive lattice vectors $\mathbf{a}_1, \mathbf{a}_2, \mathbf{c}$ and the shift vector Δ.

with

$$\begin{aligned}
\tilde{H}_0 \;=\;& (M_0+6B)I - B(2\cos\tilde{X}+\cos\tilde{Y})(\lambda_1+\lambda_6) + B\sin\tilde{Y}(\lambda_2+\lambda_7) \\
& - 2B\cos\tilde{X}\cos\tilde{Y}\cos\tilde{Z}\,\lambda_4 - B\cos\tilde{Z}\,\lambda_4 + 2B\cos\tilde{X}\sin\tilde{Y}\cos\tilde{Z}\,\lambda_5 \\
& + \underline{B\sin\tilde{Z}\,\lambda_5} - \underline{2B\cos\tilde{X}\sin\tilde{Y}\sin\tilde{Z}\,\lambda_4} + \underline{2B\cos\tilde{X}\cos\tilde{Y}\sin\tilde{Z}\,\lambda_5} \qquad (3.30) \\
\tilde{H}_1 \;=\;& \sin\tilde{X}(\lambda_1+\lambda_6) - \cos\tilde{X}(\lambda_2+\lambda_7) + \cos(\tilde{X}+\tilde{Y})\cos\tilde{Z}\,\lambda_5 \\
& + \sin(\tilde{X}+\tilde{Y})\cos\tilde{Z}\,\lambda_4 - \underline{\sin(\tilde{X}+\tilde{Y})\sin\tilde{Z}\,\lambda_5} \\
& + \underline{\cos(\tilde{X}+\tilde{Y})\sin\tilde{Z}\,\lambda_4} \qquad (3.31) \\
\tilde{H}_2 \;=\;& -\sin\tilde{X}(\lambda_1+\lambda_6) - \cos\tilde{X}(\lambda_2+\lambda_7) + \cos(-\tilde{X}+\tilde{Y})\cos\tilde{Z}\,\lambda_5 \\
& + \sin(-\tilde{X}+\tilde{Y})\cos\tilde{Z}\,\lambda_4 - \underline{\sin(-\tilde{X}+\tilde{Y})\sin\tilde{Z}\,\lambda_5} \\
& + \underline{\cos(-\tilde{X}+\tilde{Y})\sin\tilde{Z}\,\lambda_4} \qquad (3.32) \\
\tilde{H}_3 \;=\;& \sin\tilde{X}(\lambda_1+\lambda_6) - \cos\tilde{X}(\lambda_2+\lambda_7) + \cos\tilde{Z}\,\lambda_5 + \underline{\sin\tilde{Z}\,\lambda_4}, \qquad (3.33)
\end{aligned}$$

where we have used the notations $\tilde{X} \equiv k_X a/\sqrt{2}$, $\tilde{Y} \equiv k_Y a\sqrt{3/2}$, and $\tilde{Z} \equiv k_Z a\sqrt{3}$. Here, a denotes the lattice constant of the original cubic unit cell. The underlined terms break in-plane time-reversal symmetry with respect to the XY plane.

In the following, everything is expressed in terms of the new coordinate system. The weak indices are now (001). Therefore, we are particularly interested in the in-plane time-reversal symmetry with respect to the (001) plane. The associated operator reads

$$\Theta_{(001)} = i(I \otimes s^y \otimes \mathbb{1})K \;\text{ with }\; k_X, k_Y, k_Z \to -k_X, -k_Y, k_Z. \qquad (3.34)$$

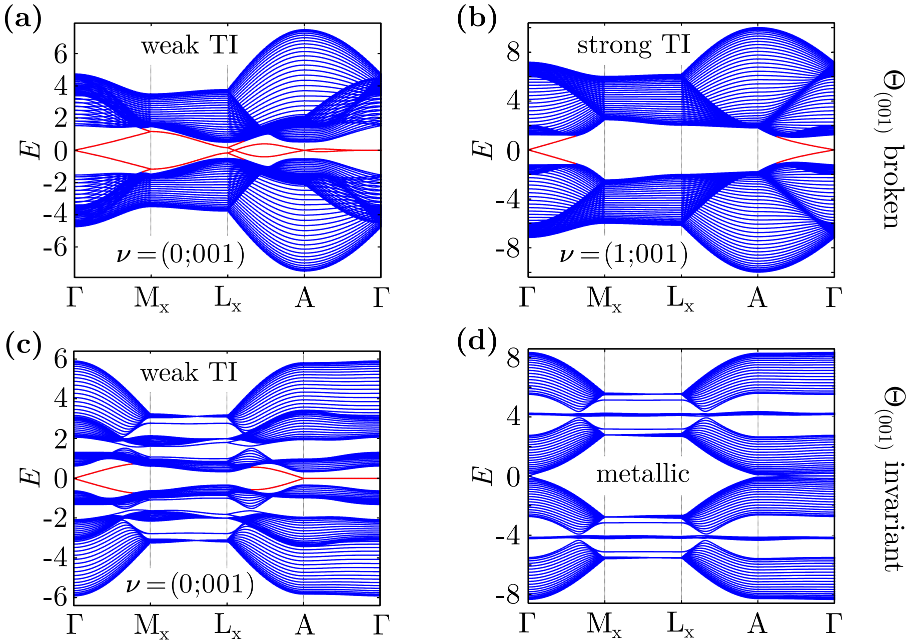

Figure 3.13: Energy bands for the cubic Liu-Qi-Zhang model: bands of a (010) slab (with respect to the rotated coordinate system) of width $W = 20$ are shown along high symmetry lines of the surface BZ associated with the hexagonal unit cell. The model parameters are $M_0 = -4.5$, $A = B = 1.0$ for panels (a), (c), and $M_0 = -2.0$, $A = B = 1.0$ for panels (b), (d). Shown are the band structures without (upper panels) and with (lower panels) in-plane time-reversal symmetry with respect to the XY plane. Relevant surface states are highlighted in red.

We will now turn to the analysis of surface states for a slab of thickness W with (010) surfaces. First, let us have a look at the case where the considered in-plane time-reversal symmetry $\Theta_{(001)}$ is broken. In Fig. 3.13(a), the corresponding band structure is shown along high symmetry lines of the new surface BZ. We find a Dirac point at A, another one at Γ, and two line degeneracies along $\overline{M_x L_x}$. However, these line degeneracies come in pairs and could easily be gapped out. For this reason, they are trivial surface bands.

In Eq. (3.33), all terms of the Bloch Hamiltonian that break in-plane time-reversal symmetry are underlined. We choose to tune *all* k_Z dependent terms to zero except the $\cos k_Z \, \lambda_5 \otimes \Gamma_3$ term which preserves in-plane time-reversal symmetry. This is possible without closing the bulk energy gap thereby ensuring that the system stays in the weak TI phase. The result is shown in Fig. 3.13(c). We observe that the trivial line degeneracies along $\overline{M_x L_x}$ are pushed out of the bulk energy gap. Along the other trivial direction $\overline{A\Gamma}$, a Dirac line forms which is now topologically protected by in-plane time-reversal symmetry. This is in perfect agreement with the results obtained for the stacked Kane-Mele model.

Finally, in the Liu-Qi-Zhang model we can easily check how the surface states of a strong TI phase are affected by establishing in-plane time-reversal symmetry. This is shown in Figs. 3.11(b) and (d) for $\Theta_{(100)}$ symmetry with respect to the original coordinate system, and in Figs. 3.13(b) and (d) for $\Theta_{(001)}$ symmetry with respect to the rotated coordinate system. Without the symmetry, we find one Dirac point at the Γ point of the surface BZ in both cases. However, once we establish the considered in-plane time-reversal symmetry, the bulk energy gap closes. As already pointed out at the end of Sec. 3.3, this is due to the connection of the surface states to the bulk continuum: it causes the bulk bands to be pulled down along $\overline{\Gamma X}$ or $\overline{A\Gamma}$. Therefore, it is not possible for strong TIs to realize topologically protected Dirac lines.

3.6 Possible experimental detection

Experimentally, the surface Dirac lines connecting two time-reversal invariant points in a weak TI with in-plane time-reversal symmetry can, in principle, be detected by ARPES. A potential candidate material, which could be investigated in this regard, is $Bi_{14}Rh_3I_9$ [97, 98]. It is a weak TI with $\mathbb{Z}_2$ invariants 0; (001). Its crystal structure is a periodic alternating stacking of 2D bismuth-rhodium networks and insulating spacer layers. The former can be viewed as a decorated honeycomb lattice, which is why the material could be described by the stacked Kane-Mele model introduced in this chapter. Furthermore, the coupling between the layers is very weak. Hence, $Bi_{14}Rh_3I_9$ is a potential candidate material to exhibit in-plane time-reversal invariance with respect to its honeycomb layers.

ARPES experiments require very clean and smooth surfaces. For $Bi_{14}Rh_3I_9$, the 1D surface Dirac states would appear on surfaces perpendicular to its layers. Such surfaces are very challenging to prepare since the material naturally cleaves parallel to the layers it is composed of. However, their preparation is not impossible [109] and further advances in preparation processes could bring the direct detection of 1D surface Dirac states into reach.

4 Topological mirror insulators in one dimension

4.1 Introduction

4.1.1 Topological crystalline insulators

In the previous chapters we have discussed different realizations of topological phases of matter, namely systems realizing the QHE, and time-reversal invariant TIs in two and three dimensions. The former are characterized by a $\mathbb{Z}$ invariant, the so-called Chern number, whereas the latter are described by a $\mathbb{Z}_2$ topological number. Furthermore, the topological nature of these systems is in perfect agreement with the predictions of the Altland-Zirnbauer table of topological insulators and topological superconductors [28,34], which classifies all gapped single-particle Hamiltonians according to their symmetry and dimensionality (see Sec. 2.1.2).

The topological phases occurring in the Altland-Zirnbauer table are commonly referred to as "strong" since their topologically nontrivial nature is protected entirely by so-called generic, non-spatial symmetries[20], which are time-reversal, particle-hole, and chiral symmetry[21]. These symmetries are *intrinsic* properties of the system and cannot be represented by unitary operators that commute with the Hamiltonian. Specifically, time-reversal and particle-hole operators are anti-unitary and commute with the Hamiltonian, whereas the unitary chiral operator anticommutes with it. As a consequence, topologically protected states appear on *all* surfaces and interfaces of the system, as well as in the presence of weak disorder because those are spatial modifications of the system and, thus, do not affect a non-spatial symmetry.

---

[20] We have already seen an important exception: *weak* topological insulators in 3D also rely on the presence of translational symmetry. Their topological features are only protected as long as translational symmetry is preserved.

[21] In this sense, a QHE system in the unitary Altland-Zirnbauer class A can be considered as the "strongest" topological phase because it does not rely on any symmetry.

In the search for novel topological phases of matter, the notion of topological protection was relaxed to also include ordinary spatial symmetries represented by unitary operators. This led to the discovery of *topological crystalline insulators* [110, 111]: novel states of matter whose topological nature arises from crystal symmetries. Those symmetries are point-group symmetries, such as inversion [47, 48], mirror [112–115] and rotation [110]; space-group symmetries [116–119], such as glide planes and screw axes; or a combination of them [120–123]. Recently, this concept has even been extended to include magnetic space groups [124–126]. It is not difficult to imagine that the discovery of the topological crystalline insulator (TCI) has opened the door to a plethora of new topological phases based on the richness and complexity of crystal structures. Besides, crystal symmetries can also enrich the topology of systems that are already topological in the strong sense [39, 99, 127]. For instance, we have seen in Chapter 2 that inversion symmetry enriches the topology of the Hofstadter model.

Topological crystalline insulators are "weaker" than their strong relatives which rely on intrinsic symmetries only. The reason is twofold. First, crystal symmetries are susceptible to disorder. Therefore, topological features are expected to persist only if the protecting crystal symmetry is preserved on average [115, 128]. Second, *not all* surfaces of a TCI accommodate topological surface states, only those that do not break the protecting crystal symmetry. For instance, a TCI protected by a C_4 rotation symmetry will, in general, have topological states only on surfaces perpendicular to the axis of rotation [110].

To prepare and find novel TCI phases, it is useful to extend the standard Altland-Zirnbauer table to include also crystalline symmetries. This has been done for several cases, such as systems with inversion [47] or reflection symmetry [113, 128]. In general, the resulting tables are much more involved than the standard Altland-Zirnbauer classification due to the various possible relations between the generic symmetry operators and the additional unitary symmetries. The corresponding invariants are typically derived from strong topological invariants associated with symmetry-invariant BZ cuts. An example is the so-called *mirror Chern number* [127]. However, later on we will see that this is not always the case.

In the following sections, we will discuss two examples of topological crystalline insulators and present their topological invariants.

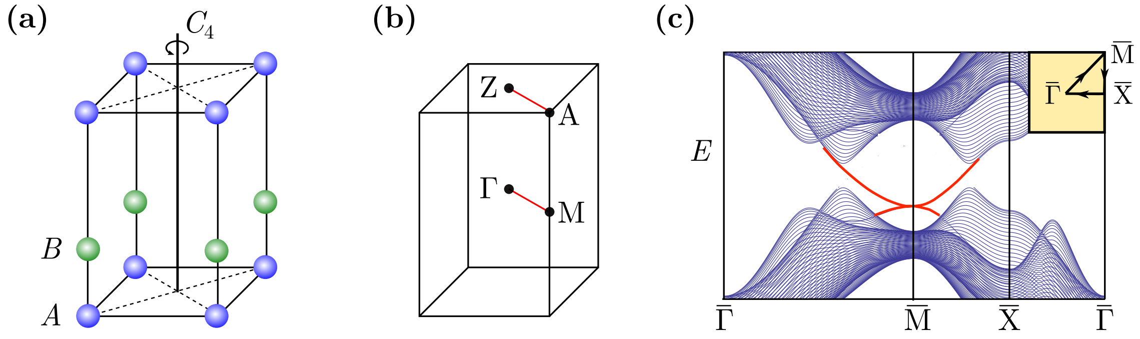

Figure 4.1: (a) Bipartite tetragonal lattice with a C_4 axis. (b) Corresponding bulk BZ with the four bulk momenta invariant under C_4 rotation. The red lines indicate possible paths for the calculation of the topological invariant ν_0. (c) Band structure along high-symmetry lines in the (001) surface BZ as presented in Ref. [110]. A quadratic surface band is highlighted in red.

4.1.2 Topological crystalline insulators with rotational symmetry

The notion of "topological crystalline insulators" was first introduced by Fu using the example of a system with C_4 symmetry [110]. To obtain a minimal model for a TCI, he considered a system of spinless electrons on a tetragonal lattice with a unit cell consisting of two inequivalent atoms A and B stacked along the c axis [see Fig. 4.1(a)]. For this system, he derived a general four-band tight-binding model taking into account only p_x and p_y orbitals of the electrons. Due to the symmetry of the lattice and the chosen orbitals, the model has a natural C_4 symmetry with respect to a rotation about the z axis[22]. Furthermore, it has time-reversal symmetry with $\Theta = K$ for spinless electrons.

Fu showed that his model features a gapped phase in a finite parameter range. Most remarkably, the (001) surface, which preserves the C_4 symmetry, exhibits surface states traversing the entire bulk energy gap in this phase as shown in Fig. 4.1(c). Moreover, the surface states are doubly degenerate at the $\bar{M}$ point of the surface BZ. This degeneracy is not accidental. The $\bar{M}$ point is a fixed point under fourfold rotation and the two degenerate states form a two-dimensional irreducible real representation of C_4. Hence, the degeneracy is protected by symmetry and cannot be removed[23].

Close to the $\bar{M}$ point, the two bands of surface states can be represented in terms of p_x and p_y orbitals. In this representation, C_4 rotation can be represented by $e^{i\sigma_y \pi/4}$, where σ_y is a Pauli matrix. In the presence of C_4 and Θ symmetry, it can be shown that, to leading order, the Hamiltonian of the surface states must be of the form

---

[22] The same argument works for d_{xz} and d_{yz} orbitals since they transform in the same way as p_x and p_y orbitals under C_4.

[23] Note that there is no Kramers theorem to enforce the degeneracy because $\Theta^2 = +1$.

$$H(k_x, k_y) = \frac{k^2}{2m_0}\,\mathbb{1} + \frac{k_x^2 - k_y^2}{2m_1}\,\sigma_z + \frac{k_x k_y}{2m_2}\,\sigma_x. \tag{4.1}$$

Hence, the symmetry constrains suppress the linear order and lead to a *quadratic* dispersion around the $\bar{M}$ point, as opposed to a linear Dirac dispersion for "conventional" topological insulators.

Moreover, these surface states are topologically protected. This can be seen as follows: due to the symmetry of the model, (001) surface states at the C_4-invariant momenta $\bar{M}$ and $\bar{\Gamma}$ must be doubly degenerate. Hence, in analogy with QSHIs in 2D, there are two topologically distinct ways of connecting these doublets with each other and with the valance and conduction bands. This gives rise to a $\mathbb{Z}_2$ classification, where in the nontrivial phase the surface bands cross the Fermi level an *odd* number of times along a path connecting $\bar{\Gamma}$ and $\bar{M}$. Note that other surfaces do not feature topological surface states because they break C_4 symmetry.

From a more general perspective, the topological nature of a spinless, time-reversal invariant insulator with C_4 symmetry can be understood in the following way. There are four C_4-invariant momenta $\mathbf{k}_i$ in the 3D BZ of the system, namely $\Gamma = (0, 0, 0)$, $M = (\pi, \pi, 0)$, $A = (\pi, \pi, \pi)$, and $Z = (0, 0, \pi)$ [see Fig. 4.1(b)]. At these points, the Bloch Hamiltonian $H(\mathbf{k}_i)$ of the system commutes with the unitary operator U representing a C_4 rotation. Hence, the energy states at $\mathbf{k}_i$ can be chosen to be eigenstates of fourfold rotation with possible rotation eigenvalues 1, -1, i, and $-i$. In addition, the momenta $\mathbf{k}_i$ are invariant under time-reversal. Due to time-reversal symmetry with $\Theta = K$ and $\Theta^2 = +1$, this imposes a reality condition. More specifically, the Bloch Hamiltonian $H(\mathbf{k}_i)$ at these points must be real and its eigenstates can always be chosen to be real. Under these conditions, group theory tells us that whenever there is a state with rotation eigenvalue $\pm i$, there must also be another, degenerate state[24] with eigenvalue $\mp i$. Furthermore, such a doublet gives rise to an effective Kramers theorem with respect to the operator $\tilde{\Theta} \equiv U\Theta$, because $\tilde{\Theta}^2 = U\Theta U\Theta = U^2\Theta^2 = -1$, where we have used that, with eigenvalues $\pm i$, the rotation operator U squares[25] to -1.

---

[24] The reason is that the cyclic group C_4 is a rather peculiar group. It has four one-dimensional irreducible representations. However, the two representations with C_4 eigenvalues $\pm i$, which are commonly grouped under the representation label E, together form a so-called *separable degenerate* representation [129]. It can be shown that these representations always appear together and give rise to a degenerate doublet of states.

[25] Note that we do not have an effective Kramers theorem for bands with rotation eigenvalues ± 1, because the corresponding rotation operator would square to $+1$.

For simplicity, let us assume that all occupied bands transform as doublets under fourfold rotation. In this case, we can follow the steps of the derivation of the Fu-Kane invariant for QSHIs in 2D, just with the operator Θ replaced by $\tilde{\Theta}$ and with paths in $\mathbf{k}$ space connecting the C_4-invariant momenta $\mathbf{k}_i$. Finally this leads to $\mathbb{Z}_2$ topological invariants ν_0 and $\nu_{\Gamma M}$, ν_{AZ} of the following form [110]:

$$\begin{aligned}(-1)^{\nu_0} &= (-1)^{\nu_{\Gamma M}}(-1)^{\nu_{AZ}}, && (4.2)\\ (-1)^{\nu_{\mathbf{k}_1\mathbf{k}_2}} &= \exp\left(i\int_{\mathbf{k}_1}^{\mathbf{k}_2} d\mathbf{k}\cdot\mathbf{A}(\mathbf{k})\right)\frac{\mathrm{Pf}[w(\mathbf{k}_2)]}{\mathrm{Pf}[w(\mathbf{k}_1)]}, && (4.3)\end{aligned}$$

where $\mathbf{A}(\mathbf{k}) = -i\sum_j \langle u_{j\mathbf{k}}|\partial_{\mathbf{k}}|u_{j\mathbf{k}}\rangle$ is the $U(1)$ Berry connection and the matrix elements of $w(\mathbf{k}_i)$ are defined as $w_{mn}(\mathbf{k}_i) = \langle u_{m\mathbf{k}_i}|U\Theta|u_{n\mathbf{k}_i}\rangle$. This matrix is antisymmetric because $[H(\mathbf{k}_i), U\Theta] = 0$ and $(U\Theta)^2 = -1$. The line integrals for $\nu_{\Gamma M}$ and ν_{AZ} are along arbitrary paths connecting Γ, M and A, Z, respectively, that lie within the plane $k_z = 0$ and $k_z = \pi$, respectively, as illustrated in Fig. 4.1(b). It can be shown that, in contrast to QSHIs, $(-1)^{\nu_{\mathbf{k}_1\mathbf{k}_2}}$ is already a gauge-invariant $\mathbb{Z}_2$ quantity, i.e., $\nu_{\Gamma M}$ and ν_{AZ} define topological invariants for the planes $k_z = 0$ and $k_z = \pi$, respectively. Due to the relation in Eq. (4.2) between the three $\mathbb{Z}_2$ invariants, a 3D crystalline topological insulator with time-reversal and C_4 symmetry is fully characterized by the strong index ν_0 and one of the weak indices $\nu_{\Gamma M}$ or ν_{AZ}. This is similar to the relation between strong and weak indices for 3D topological insulators with time-reversal symmetry. However, only the strong phase with $\nu_0 = 1$ gives rise to topological surface states on the (001) surface[26].

The $\mathbb{Z}_2$ invariants are only defined for doublet bands. Real materials usually have both doublet and singlet bands. Nonetheless, the $\mathbb{Z}_2$ invariants remain well-defined as long as the doublet bands can be energetically separated from the singlet bands, which is usually the case. This shows an important fundamental difference between "conventional" topological insulators and topological crystalline insulators. In the latter, there is an interplay between symmetry representations and the topology of the corresponding energy bands. Specifically, in our example the nontrivial topology arises from doublet bands alone whereas singlet bands are always trivial.

---

[26] The reason is that the (001) surface of a system with $\nu_0 = 0$ but $\nu_{\Gamma M} = \nu_{AZ} = 1$ would correspond to a dark surface, similar to the dark surface of weak topological insulators (see Sec. 3.1.3). The weak indices would have implications only for surfaces perpendicular to the dark surface. However, these surfaces break the protecting C_4 symmetry and, therefore, surface states are not protected. Such a phase is an example of a topological system without topological surface states. Nevertheless, the nontrivial topology can manifest itself in other quantities, such as the entanglement spectrum, as discussed in Ref. [48]

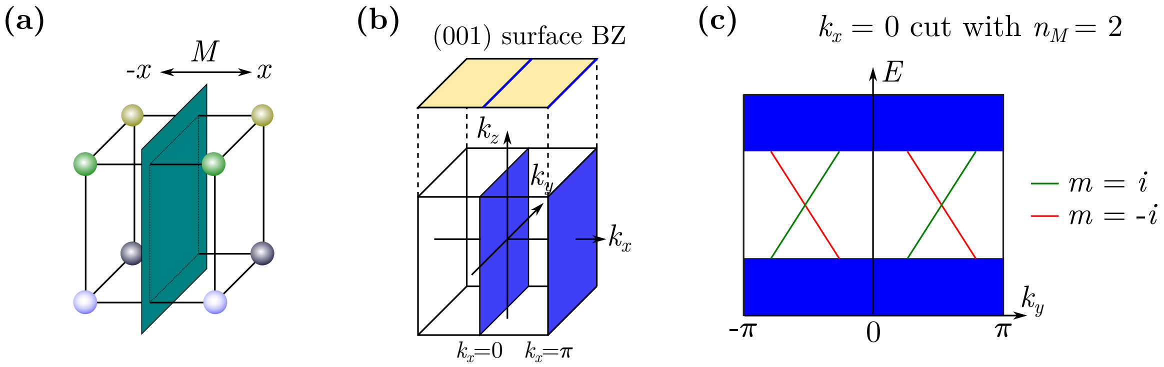

Figure 4.2: (a) Simple cubic lattice with a mirror plane highlighted in turquoise. (b) Corresponding bulk BZ with the two mirror-invariant planes highlighted in blue. The (001) surface BZ is shown on top including the projections of the mirror-invariant planes. (c) Sketch of a nontrivial surface band structure along the projection of the $k_x = 0$ mirror-invariant plane.

4.1.3 Mirror Chern number for systems with reflection symmetry

Let us consider a 3D insulating crystal with time-reversal symmetry and reflection symmetry with respect to a mirror plane. Without loss of generality, let the mirror plane be parallel to the yz plane, i.e., the mirror operation takes x to $-x$. For simplicity, we further assume that the crystal is a simple cubic lattice [see Fig. 4.2(a)]. Due to reflection symmetry, the Bloch Hamiltonian $H(\mathbf{k})$ of the system must satisfy

$$MH(k_x, k_y, k_z)M^{-1} = H(-k_x, k_y, k_z), \tag{4.4}$$

where M is a unitary operator representing the mirror operation. From this equation we immediately see that the Bloch Hamiltonian commutes with the mirror operator M in the mirror-invariant planes $k_x = 0$ and $k_x = \pi$ [see Fig. 4.2(b)]. Therefore, in these planes the Bloch Hamiltonian decomposes into two blocks corresponding to the mirror eigenvalues $m = +i$ and $m = -i$, respectively. Since the system has an energy gap, we can associate a Chern number $n_{\pm i}(k_x)$ with each of the blocks, where $k_x = 0$ or π. Moreover, time-reversal symmetry requires $n_{+i} + n_{-i} = 0$. Nevertheless, in analogy with the QSHE, the difference of the two numbers defines a toplogical invariant for each of the mirror-invariant planes. This is the so-called *mirror Chern number* [127],

$$n_M(k_x) = \frac{1}{2}[n_{+i}(k_x) - n_{-i}(k_x)]. \tag{4.5}$$

What are the implications for surface states? First of all, we already know that surface

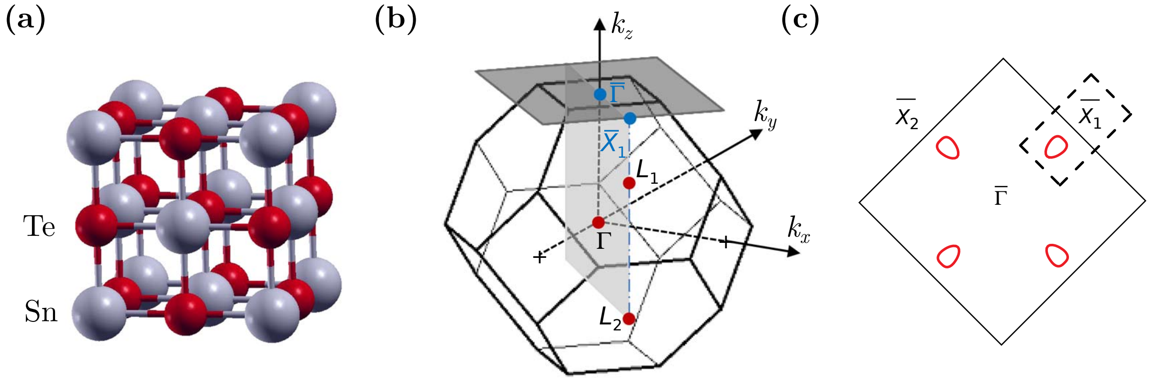

Figure 4.3: Lattice and BZs of the topological crystalline insulator SnTe as presented in Ref. [112]: (a) face-centered cubic lattice. (b) Corresponding BZ with high-symmetry points. Also indicated is the (001) surface BZ and one of the mirror-invariant planes. (c) Fermi surface of the (001) surface with four topologically protected Dirac-cone pockets.

states can only be protected on surfaces that do not break reflection symmetry. In our example, such a surface is for instance the (001) surface. In the corresponding surface BZ the lines with $k_x = 0$ and $k_x = \pi$ correspond to surface projections of the mirror-invariant planes above [see Fig. 4.2(b)]. Let us assume that n_M is nontrivial for the $k_x = 0$ plane. Thus, the nontrivial blocks of the Bloch Hamiltonian in this plane give rise to n_M pairs of counterpropagating surface states along $k_x = 0$ by bulk-boundary correspondence [see Fig. 4.2(c)]. At the crossing point between two counterpropagating states, it is not possible to couple the states in order to open an energy gap since they belong to two different reflection-symmetry sectors. Hence, the crossing point is protected by symmetry. Away from $k_x = 0$, the states no longer have a well-defined mirror eigenvalue and the degeneracy is lifted. This gives rise to n_M topologically protected surface Dirac cones. In contrast to 3D TRI topological insulators, where the Dirac cones are pinned to time-reversal invariant momenta, the surface Dirac cones of a system with nontrivial mirror Chern numbers can in principle be anywhere along the line $k_x = 0$ while respecting time-reversal symmetry [112].

A material realization of a topological crystalline insulator with nonzero mirror Chern number is SnTe [112, 130]. The crystal structure of SnTe is face-centered cubic (rocksalt), as illustrated in Fig. 4.3(a). Moreover, the material is an insulator with trivial $\mathbb{Z}_2$ invariants. However, the (011) mirror plane, and other planes equivalent by symmetry, give rise to a nontrivial mirror Chern number of $n_M = -2$ and, thus, to topologically protected Dirac cones on certain surfaces [112]. Remarkably, the *total* number of protected Dirac cones depends on the considered surface, which is in stark contrast to "conventional" topological insulators in 3D.

The (001) surface is symmetric about the two equivalent (011) and (0-11) mirror planes. In the surface BZ, these planes are projected onto two perpendicular lines going through the $\bar{X}_1$ and $\bar{X}_2$ points. Since we have mirror Chern numbers of $n_M = -2$ associated with *both* lines, there are in total $2 \times 2 = 4$ surface Dirac cones around the $\bar{\Gamma}$ point of the surface BZ [see Fig. 4.3(c)]. Similarly, we can deduce the number of surface Dirac cones for other terminations. The (111) surface preserves three equivalent mirror planes which are projected onto three mirror-invariant lines in the corresponding surface BZ. Hence, there are $2 \times 3 = 6$ topologically protected surface Dirac cones on the (111) surface of SnTe. Finally, the (110) surface is symmetric about one mirror plane giving rise to two surface Dirac cones.

4.2 One-dimensional topological insulators with time-reversal symmetry

As we have seen in the previous sections, crystal symmetries can lead to entirely novel topological phases of matter which are dubbed topological crystalline insulators. In particular, classes of systems that are trivial according to the standard Altland-Zirnbauer classification of topological insulators might reveal a nontrivial topological nature once crystal symmetries are imposed.

In this light, we are going to turn our attention to one of the most-studied classes of the Altland-Zirnbauer table, namely the symplectic class AII [34]. This class contains all time-reversal symmetric systems whose time-reversal operator Θ squares to -1, and thus systems of spin-1/2 electrons with time-reversal symmetry. Most importantly, as we have discussed in Chapter 3, the famous QSHIs in 2D and the $\mathbb{Z}_2$ topological insulators in 3D fall into this class. However, in one dimension this class does not allow for a nontrivial topology in the scope of the standard Altland-Zirnbauer classification. Nevertheless, we will show, by closely following Ref. [115], that a crystalline symmetry, namely mirror symmetry, leads to a class of one-dimensional TRI crystalline topological insulators beyond the standard Altland-Zirnbauer scheme.

We start out by considering a generic system of spin one-half fermions in a 1D crystalline potential with time-reversal symmetry Θ. In addition, we will consider the crystal to be mirror symmetric with respect to a 1D mirror point (see Fig. 4.4). The Bloch Hamiltonian of such a system $H(k)$, where $k \in (-\pi, \pi]$ with the lattice constant set to unity, then

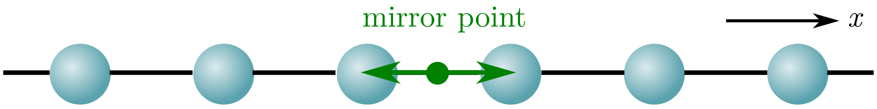

Figure 4.4: One-dimensional lattice with a mirror point.

inherits the two following symmetry constraints:

$$\Theta H(k)\Theta^{-1} = H(-k), \quad MH(k)M^{-1} = H(-k), \tag{4.6}$$

where $\Theta = (\mathbb{1} \otimes is^y)K$ is the antiunitary time-reversal operator, while $M = \mathcal{I} \otimes is^x$ is the unitary operator corresponding to the operation of reflection with respect to the 1D mirror point. Without loss of generality, we assume the latter to be in the $\hat{x}$ direction. In addition, the s^i are the usual Pauli matrices acting in spin space, while $\mathcal{I}$ acts only on the spatial degrees of freedom and thus corresponds to spatial inversion. For this representation of the symmetry operations, we have that $[\Theta, M] = 0$ and $\Theta^2 = -1$ as required for spin one-half fermions, and $M^2 = -1$ since spatial inversion must square to the identity, i.e., $\mathcal{I}^2 = 1$.

4.3 Topological invariant for topological mirror insulators in one dimension

We will now demonstrate that a 1D system under the constraints defined above is characterized by a $\mathbb{Z}_2$ topological invariant. In order to define this invariant, we will make use of the concept of charge polarization.

4.3.1 Charge polarization and partial polarization

The total charge polarization associated with the 1D Bloch Hamiltonian $H(k)$ is a measure for the electric dipole moment per unit cell and can be elegantly written in terms of the Berry connection [131–134]:

$$P_\rho = \frac{1}{2\pi} \int_{-\pi/a}^{\pi/a} dk \, A(k), \tag{4.7}$$

with the $U(1)$ Berry connection

$$A(k) = i \sum_n \langle u_{k,n} | \partial_k | u_{k,n} \rangle, \tag{4.8}$$

where $|u_{k,n}\rangle$ is the lattice-periodic part of a Bloch state at momentum k and band index n, and the sum is over all occupied bands. Since the right-hand side of Eq. (4.7) is equivalent to the famous Berry phase [131] times a factor, P_ρ is in general only defined up to an integer and can assume any value in between. Hence, it can in general not serve as a topological invariant[27].

As we have seen in Sec. 3.1, Fu and Kane introduced the notion of *partial polarization* [75] to define topological invariants for TRI topological insulators in 2D and 3D. Remarkably, also for systems in 1D the partial polarization can be used to define a topological invariant. Let us briefly recall its definition.

The concept of partial polarization is based on the well-known Kramers theorem: for a time-reversal symmetric system with half-integer total spin, every energy level is evenly degenerate. For a translationally invariant system this is equivalent to the statement that every Bloch state at k comes with a time-reversed degenerate partner at $-k$. In particular, states at the time-reversal invariant momenta $k = 0$ and π must be evenly degenerate. Hence, a fully gapped system must have an even number of occupied energy bands. Assuming, for simplicity, there are no other degeneracies than those required by time-reversal symmetry, we can divide the $2N$ occupied bands into N pairs subject to [75]

$$|u^{\mathrm{I}}_{-k,\alpha}\rangle = -e^{i\chi_\alpha(k)}\, \Theta |u^{\mathrm{II}}_{k,\alpha}\rangle, \tag{4.9}$$

where Θ is the antiunitary time-reversal operator with $\Theta^2 = -1$, $\alpha = 1, \ldots, N$, and I, II are the two time-reversed channels. Then, the partial polarizations are simply the polarizations associated with the two channels, i.e.,

$$P^s = \frac{1}{2\pi} \int_{-\pi}^{\pi} dk\, A^s(k), \quad s = \mathrm{I}, \mathrm{II}, \tag{4.10}$$

---

[27] One exception are 1D systems with *inversion symmetry*. In these systems, the total charge polarization can only assume the values 0 and 1/2 and, therefore, does serve as a topological invariant [131].

where $A^s(k) = i\sum_\alpha \langle u^s_{k,\alpha}|\partial_k|u^s_{k,\alpha}\rangle$. It is sufficient to consider P^{I} only, because

$$\begin{aligned} P^{\mathrm{I}} - P^{\mathrm{II}} &= \frac{1}{2\pi}\int_{-\pi/a}^{\pi/a} dk\,[A^{\mathrm{I}}(k) - A^{\mathrm{II}}(k)] \\ &= \frac{1}{2\pi}\int_{0}^{\pi/a} dk\,[A^{\mathrm{I}}(k) + A^{\mathrm{I}}(-k) - A^{\mathrm{II}}(k) - A^{\mathrm{II}}(-k)] \\ &= \frac{1}{2\pi}\sum_\alpha \int_{0}^{\pi/a} dk\,[\partial_k\chi_\alpha(k) - \partial_k\chi_\alpha(-k)] \\ &= \frac{1}{2\pi}\underbrace{\sum_\alpha [\chi_\alpha(\pi/a) - \chi_\alpha(-\pi/a)]}_{=2\pi m,\ m\in\mathbb{Z}} = m \in \mathbb{Z}, \end{aligned} \tag{4.11}$$

where we have used that

$$\begin{aligned} A^{\mathrm{I}}(-k) &= i\sum_\alpha \langle u^{\mathrm{I}}_{-k,\alpha}|\partial_{-k}|u^{\mathrm{I}}_{-k,\alpha}\rangle = -i\sum_\alpha e^{-i\chi_\alpha(k)}\langle \Theta u^{\mathrm{II}}_{k,\alpha}|\partial_k|e^{i\chi_\alpha(k)}\Theta u^{\mathrm{II}}_{k,\alpha}\rangle \\ &= -i\sum_\alpha \langle \Theta u^{\mathrm{II}}_{k,\alpha}|\partial_k \Theta u^{\mathrm{II}}_{k,\alpha}\rangle + \sum_\alpha \partial_k\chi_\alpha(k) \\ &= -i\sum_\alpha \langle \Theta^2 \partial_k u^{\mathrm{II}}_{k,\alpha}|\Theta^2 u^{\mathrm{II}}_{k,\alpha}\rangle + \sum_\alpha \partial_k\chi_\alpha(k) \\ &= -i\sum_\alpha \langle \partial_k u^{\mathrm{II}}_{k,\alpha}|u^{\mathrm{II}}_{k,\alpha}\rangle + \sum_\alpha \partial_k\chi_\alpha(k) = A^{\mathrm{II}}(k) + \sum_\alpha \partial_k\chi_\alpha(k), \end{aligned} \tag{4.12}$$

with the properties $\langle\Theta v|\Theta w\rangle = \langle w|v\rangle$ and $\Theta^2 = -1$ of the antiunitary time-reversal operator. Hence, we have $P^{\mathrm{II}} = P^{\mathrm{I}} \bmod 1$.

4.3.2 Quantization of the partial polarization

We are now going to show that, if the system preserves mirror symmetry with $MH(k)M^{-1} = H(-k)$ and $[M,\Theta] = 0$, we further have $P_{\mathrm{I}} = -P_{\mathrm{I}} \bmod 1$.

Assume again for simplicity that we have no other degeneracies than those required by time-reversal symmetry. Then, we can write, similar to Eq. (4.9),

$$|\tilde{u}^{\mathrm{I}}_\alpha(-k)\rangle := -e^{i\beta(k)}M|u^{\mathrm{II}}_\alpha(k)\rangle, \tag{4.13}$$

where $|\tilde{u}^{\mathrm{I}}_\alpha(k)\rangle$ is an eigenstate of the Hamiltonian. Moreover, we can always choose $|u^{\mathrm{II}}_\alpha(k)\rangle$

such that $|\tilde{u}^{\mathrm{I}}_{\alpha}(k)\rangle$ is equal to $|u^{\mathrm{I}}_{\alpha}(k)\rangle$ up to a phase, i.e.,

$$|\tilde{u}^{\mathrm{I}}_{\alpha}(k)\rangle = e^{i\lambda(k)}|u^{\mathrm{I}}_{\alpha}(k)\rangle. \tag{4.14}$$

Then, using Eqs. (4.9), (4.13) and $[M,\Theta]=0$, we easily see that

$$|u^{\mathrm{I}}_{\alpha}(k)\rangle = -e^{i[\chi(-k)+\beta(-k)]}M\Theta|\tilde{u}^{\mathrm{I}}_{\alpha}(k)\rangle \tag{4.15}$$

With this, we get

$$\begin{aligned} P^{\mathrm{I}} &= \frac{i}{2\pi}\sum_{\alpha}\int_{-\pi/a}^{\pi/a} dk\,\langle u^{\mathrm{I}}_{k,\alpha}|\partial_k|u^{\mathrm{I}}_{k,\alpha}\rangle \overset{(4.15)}{=} \frac{i}{2\pi}\sum_{\alpha}\int_{-\pi/a}^{\pi/a} dk\,\langle M\Theta\tilde{u}^{\mathrm{I}}_{k,\alpha}|\partial_k M\Theta|\tilde{u}^{\mathrm{I}}_{k,\alpha}\rangle \\ & \quad \underbrace{-\frac{1}{2\pi}\sum_{\alpha}\int_{-\pi/a}^{\pi/a} dk\,\partial_k[\chi(-k)+\beta(-k)]}_{=2\pi n,\, n\in\mathbb{Z}}\,. \end{aligned} \tag{4.16}$$

Since P^{I} is defined only up to an integer, we drop the second term and continue as follows

$$\begin{aligned} P^{\mathrm{I}} &= \frac{i}{2\pi}\sum_{\alpha}\int_{-\pi/a}^{\pi/a} dk\,\langle (M\Theta)^{\dagger}\partial_k M\Theta\tilde{u}^{\mathrm{I}}_{k,\alpha}|\tilde{u}^{\mathrm{I}}_{k,\alpha}\rangle = -\frac{i}{2\pi}\sum_{\alpha}\int_{-\pi/a}^{\pi/a} dk\,\langle \tilde{u}^{\mathrm{I}}_{k,\alpha}|\partial_k|\tilde{u}^{\mathrm{I}}_{k,\alpha}\rangle \\ &\overset{(4.14)}{=} -\frac{i}{2\pi}\sum_{\alpha}\int_{-\pi/a}^{\pi/a} dk\,\langle u^{\mathrm{I}}_{k,\alpha}|e^{-i\lambda(k)}\partial_k e^{i\lambda(k)}|u^{\mathrm{I}}_{k,\alpha}\rangle = -P^{\mathrm{I}} + m,\ m\in\mathbb{Z}, \end{aligned} \tag{4.17}$$

where we have used that $M\Theta$ is antiunitary with properties $\langle (M\Theta)^{\dagger}v|w\rangle = \langle M\Theta w|v\rangle$ and $(M\Theta)^{\dagger}M\Theta = 1$. Hence, we have shown that $P^{\mathrm{I}} = -P^{\mathrm{I}}\,\mathrm{mod}\,1$, which means P^{I} can only assume the two distinct values 0 or 1/2 up to an integer.

4.3.3 Topological invariant

The consequence of the result above is twofold. First, it follows that the charge polarization P_{ρ} of a 1D insulator with a 1D mirror point is an integer quantity. Second, the quantized nature of the partial polarization allows to define a $\mathbb{Z}_2$ topological invariant $\nu = 2P^{s}\mathrm{mod}\,2 \equiv 0,1$. This gives rise to two topologically distinct states that cannot be adiabatically connected without closing the bulk energy gap or breaking the defining symmetries. Using the $U(2N)$ invariant form of the partial polarization [75], where $2N$ is the number of occupied energy bands, the topological invariant explicitly reads:

$$\nu := \frac{1}{\pi}\left[\int_0^{\pi} dk\, A(k) + i\,\log\left(\frac{\mathrm{Pf}[w(\pi)]}{\mathrm{Pf}[w(0)]}\right)\right] \mathrm{mod}\,2, \tag{4.18}$$

where $A(k) = i\sum_{n\,\mathrm{occ.}}\langle u_{k,n}|\partial_k|u_{k,n}\rangle$ is the Berry connection of all occupied bands, and we have introduced the $U(2N)$ matrix $w_{\mu\nu}(k) = \langle u_{-k,\mu}|\Theta|u_{k,\nu}\rangle$ which is antisymmetric at $k = 0, \pi$ and thus characterized by its Pfaffian $\mathrm{Pf}(w)$.

A few remarks are in order. First, it has to be emphasized that the quantities in Eq. (4.18) require a continuous gauge. Such a gauge can be straightforwardly constructed from numerically obtained eigenstates (see Appendix A). Second, it is worth to note that the $\mathbb{Z}_2$ invariant of Eq. (4.18) cannot be determined from the knowledge of the electronic wavefunctions only at the mirror invariant momenta, as it usually occurs for topological crystalline insulators in 2D and 3D. Eq. (4.18) requires the knowledge of the wavefunctions in the *entire* BZ. Furthermore, this implies that for a topological phase transition that occurs via a closing and reopening of the 1D bulk gap at momentum q, q is in general not a high-symmetry point in the BZ, as we will later see in the discussion of the spin-orbit coupled AAH model.

Finally, one has to point out that the existence of the $\mathbb{Z}_2$ topological invariant does not contradict the Altland-Zirnbauer classification of topological insulators and superconductors [34], which does not take into account the point-group symmetries of the system. In the absence of mirror symmetry, the partial polarizations of a 1D system with time-reversal symmetry are indeed no longer quantized, and therefore ν does not represent an invariant. The existence of 1D topological mirror insulators is instead in agreement with the recent extensions of the original Altland-Zirnbauer classification taking into account point-group symmetries [47,113,128], in particular with Refs. [113] and [128] which predict that mirror-symmetric 1D systems in principle allow for a $\mathbb{Z}_2$ invariant[28].

4.3.4 Bulk-boundary correspondence: quantized end charges

The quantization of the partial polarization has a direct physical consequence. In fact, the charge polarization of a system is directly connected to the accumulated bound charge at its surfaces [132]. For a one-dimensional system the end charge Q is simply related to the polarization P by $Q\,\mathrm{mod}\,1 = P$. Since the partial polarization P^{I} is just the usual polarization associated with one of the time-reversed channels, we can assign a *partial* bound charge to this channel which is proportional to P^{I}. With two identical time-reversed channels, the total bound charge per end is then

---

[28] In this respect, it must be pointed out that certain types of translational-symmetry breaking terms, such as charge-density waves, can turn the system into a trivial insulator [113], similar to weak topological insulators in 3D.

$$Q \bmod 2 = 2P_{\mathrm{I}} = \nu. \tag{4.19}$$

This establishes a direct connection between the number of bound charges and the $\mathbb{Z}_2$ invariant ν. In particular, systems for which $\nu = 1$ are topological mirror insulators: they are characterized by the presence of an *odd* number of integer-valued electronic end charges at the mirror symmetric boundaries of the system.

4.4 Spin-orbit coupled Aubry-André-Harper models

We are now going to discuss an explicit model that features a 1D topological mirror insulating phase. In particular, we will consider the following tight-binding Hamiltonian for spin-1/2 electrons on a 1D lattice

$$\begin{aligned}\mathcal{H} \;=\; & \sum_{j,\sigma}[t_0 + \delta t \cos(2\pi\alpha j + \phi_t)]\, c^{\dagger}_{j+1,\sigma}c_{j\sigma} + \sum_{j,\sigma}[V_0 + \delta V \cos(2\pi\beta j + \phi_V)]\, c^{\dagger}_{j\sigma}c_{j\sigma} \\ & + i\sum_{j,\sigma,\sigma'}[\lambda_0 + \delta\lambda \cos(2\pi\gamma j + \phi_\lambda)]\, c^{\dagger}_{j+1,\sigma}s^{y}_{\sigma\sigma'}c_{j\sigma'} + \text{h.c.}\end{aligned} \tag{4.20}$$

This is a generalization of the famous AAH model [39,43,135,136] which we have discussed in Chapter 2. It contains harmonically modulated nearest-neighbor hopping, on-site potentials and spin-orbit coupling (SOC) with amplitudes δt, δV, $\delta\lambda$, phases ϕ_t, ϕ_V, ϕ_λ, and periodicities $1/\alpha$, $1/\beta$, $1/\gamma$. For simplicity, we restrict the model to rational values of the periodicities. Moreover, t_0, V_0 and λ_0 are the bond and site independent values of hopping, potentials and SOC, the operators $c^{\dagger}_{j\sigma}$ ($c_{j\sigma}$) create (annihilate) an electron with spin σ ($\sigma = \uparrow, \downarrow$) at lattice site j, and the s^i are Pauli matrices. The Hamiltonian of Eq. (4.20) possesses time-reversal symmetry whereas mirror symmetry is present only for specific values of the phases ϕ_t, ϕ_V and ϕ_λ. For the computation of band structures and eigenstates exact numerical diagonalization is used. In the case of periodic boundary conditions, we are going to exploit the translational symmetry of the system and work with the corresponding Bloch Hamiltonian in momentum space. For open boundary conditions, we will take the real-space Hamiltonian with a finite number of unit cells. The $\mathbb{Z}_2$ invariant of Eq. (4.18) is calculated numerically using the aforementioned procedure to construct a

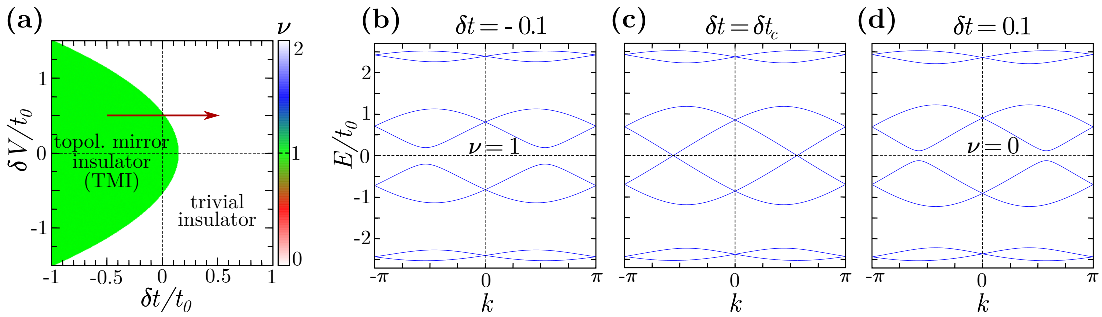

Figure 4.5: Phase diagram and spectra of the spin-orbit coupled AAH model with $\alpha = \gamma = 1/2$ (dimerization), $\beta = 1/4$, $V_0 = 0$, $\lambda_0 = 0.5t_0$, $\delta\lambda = -0.3t_0$, $\phi_t = \phi_\lambda = \pi$: (a) half-filling phase diagram of the bulk for $\phi_V = -\pi/4$. The value of the $\mathbb{Z}_2$ invariant ν is indicated by pixel color. Note that it only assumes two distinct values, 0 and 1. (b)–(d) Bulk band structures for $\delta V = 0.5t_0$ and fixed δt with (b) $\delta t = -0.1t_0$, (c) $\delta t = \delta t_c \approx 0.025$, (d) $\delta t = 0.1t_0$. The band structures correspond to systems along the arrow in (a). Note that the half-filling bulk energy gap closes away from the mirror-invariant points $k = 0$ and π.

continuous $U(2N)$ gauge from numerically obtained eigenstates (see Appendix A).

We will consider the model in Eq. (4.20) with $\alpha = \gamma = 1/2$, $\phi_t = \phi_\lambda = \pi$, $V_0 = 0$, and $\beta = 1/4$. With this choice of parameters, the unit cell of our model Hamiltonian contains four lattice sites and the model preserves reflection symmetry for $\phi_V = -\pi/4$ and $3\pi/4$. This is a direct generalization of the model considered in Chapter 2 to the spinful case. The model can potentially be realized using an ultracold Fermi gas loaded in a 1D optical lattice [54, 59, 137, 138], while the ensuing end states can be detected using time-of-flight measurements or optical microscopy [139, 140] as outlined in Sec. 2.6. We emphasize that while state-of-the-art technologies allow to create SOC terms explicitly breaking mirror symmetry [58, 141], the rapid progress in the field can be expected to bring soon a much larger variety of SOC terms into reach [58, 142, 143].

4.4.1 Phase diagram and in-gap end states

We first determine the phase diagram of our system with respect to the $\mathbb{Z}_2$ invariant ν of Eq. (4.18) for the half-filled system at $\phi_V = -\pi/4$, i.e., where the model has reflection symmetry. The phase diagram in the δt-δV parameter space is shown in Fig. 4.5(a). We identify two phases which are separated by a parabolic phase boundary: a trivial phase with $\nu = 0$ on the right side and a topological phase with $\nu = 1$ on the left side. Similarly to the spinless version of the model [39], the bulk energy gap at half filling closes at the

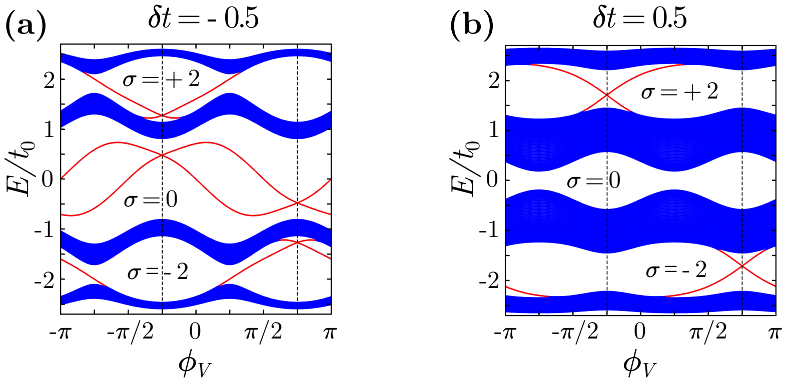

Figure 4.6: Spectra of the spin-orbit coupled AAH model in a finite geometry for different ϕ_V. Other parameters are $\alpha = \gamma = 1/2$ (dimerization), $\beta = 1/4$, $V_0 = 0$, $\delta V = 0.5t_0$ $\lambda_0 = 0.5t_0$, $\delta\lambda = -0.3t_0$, $\phi_t = \phi_\lambda = \pi$: (a) $\delta t = -0.5t_0$, (b) $\delta t = 0.5t_0$. States localized at the ends of the chain are highlighted in red. Hall conductivities σ of the bulk energy gaps are also indicated in units of e^2/h.

topological phase transition.

Note that the bulk energy gap closes and reopens away from the mirror-invariant momenta, as is shown in Figs. 4.5(b)–(d). This is in contrast to other crystalline topological phases as pointed out in Sec. 4.1.1.

Moreover, the nontrivial topology of the model manifests itself through the appearance of characteristic in-gap end states. This is demonstrated in Fig. 4.6, where energy spectra for the AAH model with open boundary conditions are shown. The phase shift ϕ_V of the on-site modulation is varied smoothly from $-\pi$ to π thereby passing through the mirror-symmetric cases at $-\pi/4$ and $3\pi/4$. At these points, we find four degenerate in-gap end states at half filling provided we are in the nontrivial area of the phase diagram of Fig. 4.6(a). Away from the mirror-symmetric points, the observed states are split into two degenerate pairs. The two-fold degeneracy remains since the model in Eq. (4.20) preserves time-reversal symmetry for all values of ϕ_V. The half-filling end states are not encountered for parameters of the model for which we are in the trivial region of the phase diagram, as can be seen in Fig. 4.6(b).

Taking a different perspective, the appearance of end states at the 1/4 and 3/4 filling gaps can also be understood by interpreting the phase ϕ_V as the momentum of an additional artificial dimension. In this case, our model of Eq. (4.20) can be mapped to a dimerized Hofstadter model [36, 39, 41, 43] for spinful fermions, with SOC in one direction only. Contrary to models investigated before [144, 145], the resulting model explicitly breaks 2D time-reversal symmetry, $\Theta^{-1}H(k, \phi_V)\Theta \neq H(-k, -\phi_V)$, thereby allowing for insulating states with nonzero Chern numbers [14,15,39]. By calculating the Hall conductivities, we find that they are doubled with respect to the conventional spinless Hofstadter model [39] indicating that the two spin channels of our model carry the *same* topological content. This, in turn, implies that the in-gap states at 1/4 and 3/4 filling, appearing in Fig. 4.6, correspond to the chiral edge states of a generalized Hofstadter model in a ribbon geometry. They correspond to insulating states with Hall conductivities ±2. On the contrary, the insulating phase at half filling has zero Hall conductivity but displays two quartets of edge states in the topological phase originating from the 1D mirror-symmetric cuts [see Fig. 4.6(a)]. Furthermore, it is worth noting that these results, as a generalization of what was discussed in Chapter 2, can straight-forwardly be extended to arbitrary rational $\beta = p/q$.

4.4.2 Bulk-edge correspondence

We have shown that the appearance of electronic in-gap end states is characteristic of a topological mirror insulator. However, due to the absence of chiral symmetry, which would pin the end modes to the center of the gap, symmetry-allowed perturbations can push the end modes into the continuum of bulk states. Such perturbations could, for instance, be introduced by surface potentials.

The point above can be demonstrated explicitly by adding a generic on-site surface potential $\sum_\sigma V_{\mathrm{LR}}(c^\dagger_{1\sigma}c_{1\sigma} + c^\dagger_{L\sigma}c_{L\sigma})$ to our model with open boundary conditions, and by analyzing the ensuing energy spectra. Again, let us fix the on-site potential phase ϕ_V to $-\pi/4$ such that our model preserves mirror symmetry.

Without the surface potential, we observed two degenerate in-gap Kramers pairs at half filling in the topological phase [see Fig. 4.6(a)]. This picture changes when we switch on the surface potential V_{LR} [see Fig. 4.7(a)]. We observe that the end modes in the half-filling gap are pushed up into the conduction band, while another degenerate pair of Kramers doublets emerges from the valence band. However, the appearance of these states cannot be linked to the topological invariant of the system. In fact, these additional states occur both in the topological and in the trivial phases, as can be seen by comparing Figs. 4.7(a) and (b) at half filling.

Having established that sufficiently strong symmetry-allowed edge potentials are detrimental for the occurrence of in-gap end modes, we now proceed to demonstrate the actual bulk-boundary correspondence for our model, i.e., the existence of an odd number of integer-valued electronic end charges (see Sec. 4.3.4).

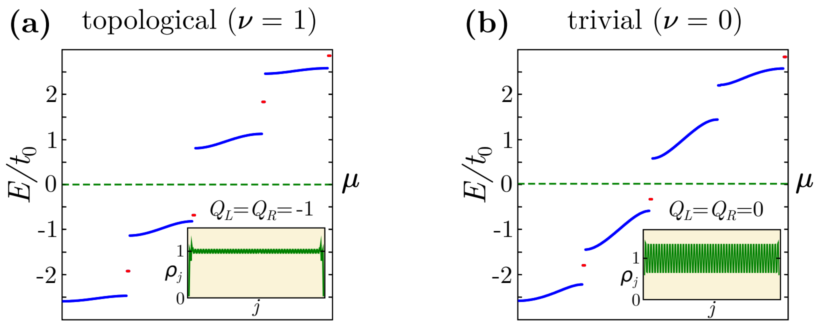

Figure 4.7: Spectra and local charge densities of the mirror-symmetric, spin-orbit coupled AAH model with open boundary conditions and $\alpha = \gamma = 1/2$, $\beta = 1/4$, $V_0 = 0$, $\delta V = 0.5t_0$, $\lambda_0 = 0.5t_0$, $\delta\lambda = -0.3t_0$, $\phi_t = \phi_\lambda = \pi$, $\phi_V = -\pi/4$, and a surface potential $V_{\mathrm{LR}} = 0.6t_0$: (a) topological phase with $\delta t = -0.5t_0$, (b) trivial phase with $\delta t = 0.4t_0$. The main panels show the energy spectra with end states highlighted in red. The dashed line signifies the chemical potential μ used for the calculation of the local charge densities ρ_j. The latter are presented in the insets. In addition, the corresponding values of the electronic end charges Q_{L} and Q_{R} are displayed.

We define the *end charge* of a system to be the net deviation of the local charge density close to the end from the average charge density in the bulk. Adopting the definition of Ref. [146], we calculate the left end charge Q_{L} and the right end charge Q_{R} from the following limits,

$$Q_{\mathrm{L}} = \lim_{l_0 < L \to \infty} \sum_{j}^{L} \Theta(l_0 - j)(\rho_j - \bar{\rho}), \tag{4.21}$$

$$Q_{\mathrm{R}} = \lim_{l_0 < L \to \infty} \sum_{j}^{L} \Theta(l_0 - L + j)(\rho_j - \bar{\rho}), \tag{4.22}$$

for sufficiently large l_0. Here, L is the length of the chain, $\Theta(x)$ is the Heaviside function and l_0 is a cut-off. $\rho_j = \sum_\nu^N |\psi_\nu(j)|^2$ is the local charge density of the ground state in units of $-e$ with the sum running over all N occupied states ψ_ν up to the chemical potential μ. The bulk charge density $\bar{\rho}$ is treated as a constant background that is fixed by the chemical potential. In particular, at half filling we have $\bar{\rho} = 1$ corresponding to one electron per site.

The insets in Fig. 4.7 show the local charge densities of the finite AAH chains when the chemical potential μ is in the half-filling bulk energy gap above or below the end states. As expected, the local charge density oscillates around $\rho = 1$ in the bulk. Moreover, in the topological phase there are large deviations from this value near the ends of the system indicating the presence of electronic end charges. On the contrary, there are no pronounced features in the trivial phase.

This is confirmed by an explicit calculation of the end charges. In the topological phase [see Fig. 4.7(a)], we find $Q_{\mathrm{L}} = Q_{\mathrm{R}} = +1$ when μ is placed right above the topological end states. Conversely, leaving the *two* boundary states at each end unoccupied leads to an end charge of -1. Hence, there is a direct correspondence between end states and end charges. End states always come in degenerate Kramers pairs due to time-reversal symmetry. From this we see that, regardless of where we put the chemical potential in the bulk energy gap and regardless of how many pairs of degenerate Kramers pairs are present, the end charge will always assume an *odd* value in agreement with the general analysis of Sec. 4.3.4. Moreover, this is a robust feature which is not affected by the presence of surface potentials.

In the trivial phase [see Fig. 4.7(b)], we find $Q_{\mathrm{L}} = Q_{\mathrm{R}} = 0$ for a chemical potential above the trivial end states. Hence, only *even* values of end charges are possible. For instance, with the trivial states unoccupied the end charge value is -2.

4.4.3 Effect of disorder

Let us now consider the fate of the in-gap end states and of the topological end charges under the influence of disorder. The topological nature of a 1D topological mirror insulator is protected by time-reversal and mirror symmetry. The latter is a spatial symmetry and is, in general, broken by disorder. However, recent studies on topological crystalline insulators have shown that their topological features are still present if the protecting symmetry is preserved on average [128]. We will now demonstrate that this holds also for our class of systems. To show this, we model the effect of disorder by adding a random nonmagnetic on-site potential of the form $\sum_j W_j c^{\dagger}_{j\sigma} c_{j\sigma}$ to our model, where the W_j are independent random variables subject to a Gaussian distribution with zero mean and standard deviation γ. The latter is a measure for the disorder strength.

To analyze the effect of disorder on the end states, we consider the expectation value of the inverse participation ratio (IPR), which is a quantitative measure of localization [146, 147]. The IPR of a given state ψ is defined as $I_{\psi} = \sum_j^L |\psi(j)|^4$ with $|\psi(j)|^2$ being the weight of the state at site j. The IPR assumes values in the interval $(0, 1]$. An IPR of 1 corresponds to a perfectly localized state whereas small values indicate a state equally distributed over the whole length of the system.

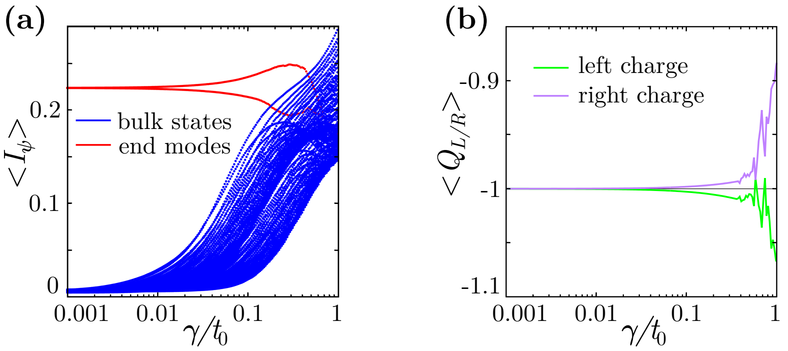

Figure 4.8: Effect of disorder in the half-filled, spinful AAH model with open boundary conditions and $\alpha = \gamma = 1/2$, $\beta = 1/4$, $t = -0.5t_0$ $V_0 = 0$, $\delta V = 0.5t_0$, $\lambda_0 = 0.5t_0$, $\delta\lambda = -0.3t_0$, $\phi_t = \phi_\lambda = \pi$, and $\phi_V = -\pi/4$ (topological phase): (a) disorder-averaged IPR $\langle I_\psi \rangle$ for bulk states and end states, (b) disorder-averaged end charges $\langle Q_\mathrm{L} \rangle$ and $\langle Q_\mathrm{R} \rangle$ with the chemical potential right below the in-gap end states. Shown is the dependence on the standard deviation γ of the random disorder potential.

Fig. 4.8(a) shows the IPR of occupied states for the finite, half-filled AAH chain of length $L = 200$ averaged over 10^3 random disorder configurations. The model parameters are chosen such that the disorder-free chain preserves mirror symmetry and is in the topological phase. We observe that the IPR of the topological end states stays nearly unaffected at a large value as long as the disorder is weak ($\gamma \lesssim 0.01t_0$). In contrast to that, the IPR of the bulk states is more than one order of magnitude lower. For stronger disorder, the topological end modes are still well localized but their IPR starts to deviate from their previously constant value due to mixing with bulk states. However, this does not lead to a sizable decrease of the IPR due to the onset of Anderson localization. The latter also accounts for the substantial increase in the IPR of the bulk states.

Fig. 4.8(b) shows the disorder-averaged values of the boundary charges Q_L and Q_R in the same setting. The chemical potential, which determines the number of occupied states, is set to be in the half-filling bulk energy gap such that the topological end states are unoccupied. In the previous section, we saw that the disorder-free values of the end charges are exactly -1. In the presence of disorder this value is barely affected up to intermediate disorder strength ($\gamma \lesssim 0.1t_0$). Only for strong disorder we see considerable deviations.

We conclude that in the presence of nonmagnetic disorder with zero mean the characteristic end states of a topological mirror insulator remain well localized and its topological end charges remain sharply quantized.

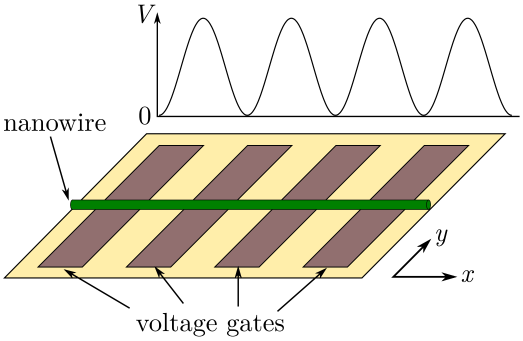

Figure 4.9: A semiconductor nanowire setup with perpendicular modulated voltage gates. The gates induce a modulation of both onsite potentials and Rashba SOC. Subject to mirror symmetry, such a nanowire hosts localized in-gap Kramers pairs at its ends.

4.5 Density- and Rashba spin-orbit-modulated semiconductor nanowires

Finally, we are going to show that the general model of Eq. (4.20) allows for topological mirror-insulating phases in a large portion of its parameter space. To demonstrate this, we consider our model with constant hopping parameters ($\delta t = 0$), larger but equal periods of the on-site potentials and SOC ($\beta = \gamma$), and nonzero average values t_0, V_0, and λ_0. In this parameter regime, the model corresponds to the tight-binding Hamiltonian of a semiconductor nanowire with Rashba SOC where opportunely designed finger gates can cause a periodic density modulation as well as a gate-tuned modulation of the Rashba SOC strength. This is illustrated in Fig. 4.9. In this setup, end states can be detected using tunneling density of states.

Fig. 4.10(a) shows a quarter-filling δV-$\delta\lambda$ phase diagram with respect to the $\mathbb{Z}_2$ invariant of Eq. (4.18) for $\beta = \gamma = 1/4$, where the corresponding unit cell comprises four lattice sites. The modulation phases are chosen such that the model respects mirror symmetry. The Rashba term preserves this symmetry for $\phi_{\lambda,m} = 0$ or π, whereas the onsite term is reflection-symmetric for $\phi_{V,m} = -\beta\pi$ or $(1-\beta)\pi$. This can be easily seen from the related discussions in Sec. 2.3. Again, we identify two distinct topological phases. The shape of the phase boundary is mainly influenced by the relative magnitude of λ_0 and V_0. Moreover, the phase with nontrivial $\mathbb{Z}_2$ invariant features characteristic Kramers pairs at the end points of the corresponding wire. This is demonstrated in Fig. 4.10(b) for a path through the phase diagram at constant $\delta\lambda$ and variable δV. At quarter filling, end states are absent for small values of δV. However, by increasing δV the bulk energy gap closes

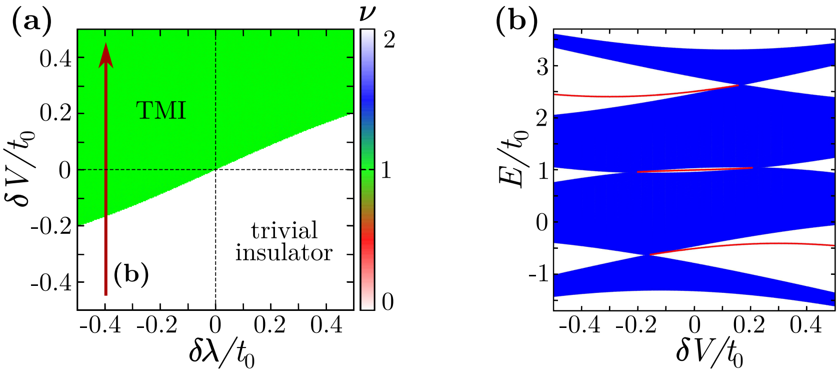

Figure 4.10: Phase diagram and spectra of a density- and Rashba spin-orbit-modulated semiconductor nanowire with $\beta = \gamma = 1/4$, $V_0 = 0.5t_0$, $\lambda_0 = 0.5t_0$, $\delta t = 0$, $\phi_V = 3\pi/4$, and $\phi_\lambda = \pi$: (a) quarter-filling phase diagram. The value of the $\mathbb{Z}_2$ invariant ν is indicated by pixel color. The arrow shows a path through the phase diagram. (b) Energy spectra of nanowires with open boundary conditions at fixed $\delta\lambda = -0.4t_0$ corresponding to δV values along the path shown in (a). States localized at the end points of the wires are highlighted in red. Note that there are end states at filling fractions 1/4, 1/2, and 3/4 in certain ranges of δV.

and reopens again, revealing two degenerate Kramers pairs localized at the end points of the wire. We also observe localized Kramers pairs at filling fractions 1/2 and 3/4 that can be attributed to a nontrivial $\mathbb{Z}_2$ invariant.

In addition, the nanowires feature end charge values of ±1 for the topological phases at 1/4, 1/2, and 3/4 filling depending on whether the chemical potential is tuned above or below the degenerate in-gap Kramers pairs. On the contrary, the trivial phases exhibit no end charges. This once again verifies the bulk-boundary correspondence.

It should be pointed out that the use of finger gates in a realistic system is expected to produce an equal phase modulation of Rashba SOC and onsite potentials ($\phi_V = \phi_\lambda \equiv \phi$). Apparently, this breaks the mirror symmetry in our tight-binding description. However, in the $\beta \to 0$ continuum limit one has $\phi_{V,m} \to \phi_{\lambda,m}$, which shows that a density- and Rashba SOC-modulated mirror-symmetric semiconductor nanowire can be realized in practice. Intriguingly, the end states of such a nanowire render an effective spin-orbit coupled quantum-dot system which can potentially be implemented to realize spin-orbit qubits [148, 149].

5 Weyl semimetals with time-reversal symmetry

5.1 Introduction

The exceptional features and unconventional physical properties of topological insulators arise from the nontrivial topology of their bulk band structure. Their features are protected as long as the relevant symmetries are preserved, and as long as the system remains in a gapped state. Remarkably, relaxing these two requirements gives rise to a plethora of novel topological phases: on the one hand, we have already seen in Chapter 4 how additional lattice symmetries lead to the emergence of topological crystalline insulators. On the other hand, also gapless systems can exhibit topological features. This important insight paved the way to the discovery of *topological semimetals* [103, 150].

The bulk energy bands of topological semimetals cross at isolated points or along nodal lines in the BZ thereby rendering the system gapless. These "diabolical" points or lines represent topologically nontrivial objects by themselves and give thus rise to topological features. In this chapter, we are going to focus on the perhaps most celebrated materials class of this kind: *Weyl semimetals*.

5.1.1 Weyl fermions as solutions of the Dirac equation

To understand the origin of the term "Weyl" semimetal, let us first recall one of the most important quantum-mechanical equations which is the *Dirac equation* [151]. The Dirac equation was derived by Paul Dirac in search for a theory reconciling quantum mechanics with Einstein's special theory of relativity. It reads

$$i\hbar\,\partial_t\psi(\mathbf{x},t) = \Big(\beta mc^2 - ic\hbar\sum_{i=1}^{d}\alpha_i\partial_{x_i}\Big)\psi(\mathbf{x},t) = H_D\,\psi(\mathbf{x},t), \tag{5.1}$$

where d labels the spatial dimension of the system, H_D is the Dirac Hamiltonian, and β, α_i are Hermitian matrices satisfying

$$\begin{aligned} \beta^2 &= \alpha_i^2 = \mathbb{1}, &(5.2)\\ \alpha_i\alpha_j + \alpha_j\alpha_i &= \{\alpha_i, \alpha_j\} = 0 \text{ for } i \neq j, &(5.3)\\ \alpha_i\beta + \beta\alpha_i &= \{\beta, \alpha_i\} = 0. &(5.4) \end{aligned}$$

The minimum size of the β and α_i matrices depends on the dimension of the system. In $d = 3$, for instance, the above algebraic relations are satisfied by four 4×4 gamma matrices: $\beta = \sigma^z \otimes \mathbb{1}_2$, $\alpha_1 = \sigma^x \otimes s^x$, $\alpha_2 = \sigma^x \otimes s^y$, $\alpha_3 = \sigma^x \otimes s^z$, where σ^i, s^i are Pauli matrices[29]. In particular, the s^i are associated with the spin degree of freedom of the particle. The solutions of the corresponding Dirac equation are four-component Dirac spinors with energies E satisfying $E^2 = (\mathbf{p}c)^2 + (mc^2)^2$, where $\mathbf{p}$ represents eigenvalues of the momentum operator $\hat{\mathbf{p}} = -i\hbar\nabla$. In this form, the Dirac equation describes 3D relativistic, *massive* spin-1/2 particles, such as electrons, and their corresponding anti-particles.

Hermann Weyl realized that the Dirac equation can be simplified in odd spatial dimensions for *massless* particles[30] [153]. He found that in any odd spatial dimension $d = 2k+1$, there exists a Hermitian matrix $\gamma_5 = -i^k\alpha_1 \dots \alpha_d$ that commutes with the "kinetic" matrices α_i but anticommutes with the "mass" matrix β. Furthermore, $\gamma_5^2 = \mathbb{1}$ which means that γ_5 has eigenvalues ± 1. Hence, the massless Dirac Hamiltonian with $m = 0$ commutes with γ_5 and its eigenspace decomposes into two sectors associated with the γ_5 eigenvalues ± 1. In particular, for $d = 3$ the Dirac Hamiltonian of a massless spin-1/2 particle is

$$H_D = c\sum_{i=1}^{3} \hat{p}_i(\sigma_x \otimes s^i) = \begin{pmatrix} 0 & c\,\hat{\mathbf{p}}\cdot\mathbf{s} \\ c\,\hat{\mathbf{p}}\cdot\mathbf{s} & 0 \end{pmatrix}. \tag{5.5}$$

Apparently, this Hamiltonian commutes with the Hermitian operator $\gamma_5 = -\sigma^x \otimes \mathbb{1}_2$. If we use eigenstates of γ_5, i.e., $\gamma_5\psi_\pm = \pm\psi_\pm$, the Dirac equation (5.1) becomes

$$i\hbar\,\partial_t\psi_\pm = -c\,(\mathbb{1}_2 \otimes \hat{\mathbf{p}}\cdot\mathbf{s})\gamma_5\,\psi_\pm = (\mathbb{1}_2 \otimes \mp c\,\hat{\mathbf{p}}\cdot\mathbf{s})\,\psi_\pm. \tag{5.6}$$

---

[29] In $d = 2$, the algebraic relations can already be satisfied by the 2×2 Pauli matrices. In particular, one can choose $\beta = \sigma^z$, $\alpha_1 = \sigma^x$, and $\alpha_2 = \sigma^y$.

[30] Another simplification was proposed by Ettore Majorana [152]. He found a real-number valued solution of the Dirac equation which describes neutral particles that are their own anti-particles.

These two equations are expressed more elegantly in the following form,

$$i\hbar\,\partial_t\psi_W = H_W\psi_W = \mp(c\,\hat{\mathbf{p}}\cdot\mathbf{s})\,\psi_W, \tag{5.7}$$

where ψ_W are two-component *Weyl* spinors and $H_W = \mp c\,\hat{\mathbf{p}}\cdot\mathbf{s}$ is the Weyl Hamiltonian. This equation is commonly known as the *Weyl equation*. We immediately see that the Weyl fermions propagate parallel or antiparallel to their spin $\mathbf{s}$ depending on their γ_5 eigenvalue. Hence, Weyl fermions have a well-defined chirality which is why they are also termed *chiral* fermions.

Shortly after Weyl's proposition of a massless spin-1/2 fermion with definite chirality, a new fundamental particle, namely the neutrino, emerged as a promising candidate. The neutrino was first postulated in 1930 by Wolfgang Pauli to explain the beta decay [154], and finally detected experimentally in 1956 [155]. For a long time, neutrinos were believed to be Weyl fermions until the discovery of a non-vanishing neutrino mass in the late 90s put an end to this theory [156,157]. Hence, as of now there are no known "fundamental" Weyl fermions in nature. Nonetheless, this is by no means the end of the story. Remarkably, it is possible for Weyl fermions to emerge as *quasiparticles* in solids [103].

5.1.2 Weyl fermions in condensed matter: Weyl semimetals

In condensed matter physics, the only fundamental particle of interest is the electron. Nevertheless, the interplay of electrons with the underlying lattice can give rise to a multitude of emergent phenomena as we have already seen in the previous chapters. The energy spectrum of electrons in solids typically consists of a multitude of energy bands which, in the ground state, are filled up to the Fermi level. Higher states in energy represent one-particle excitations of the ground state. These excitations can be described in terms of quasiparticles whose properties, such as mass or charge, can be quite different from the "bare" electrons.

A Weyl semimetal (WSM) is a three-dimensional gapless material in which the bulk energy bands close to the Fermi level coincide only at isolated points $\mathbf{k}_0$ in the Brillouin zone [158–161]. Assuming that the crossing is formed by two *non-degenerate* bands, the Hamiltonian of the system can be expanded around $\mathbf{k}_0$ in the following form [103]

$$H(\mathbf{k}) \approx f_0(\mathbf{k}_0)\,\mathbb{1} + \mathbf{v}_0\cdot\delta\mathbf{k}\,\mathbb{1} + \sum_{i=x,y,z}\mathbf{v}_i\cdot\delta\mathbf{k}\,\sigma^i, \tag{5.8}$$

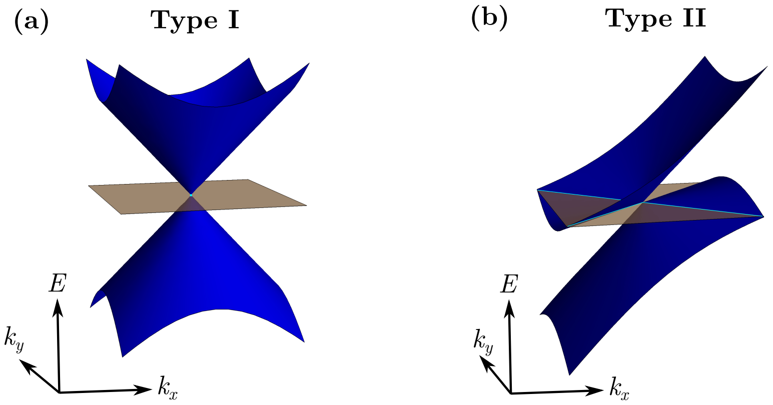

Figure 5.1: Weyl semimetals of Type I and Type II: shown are typical dispersions at $k_z = 0$. (a) Conventional Type I Weyl semimetals with point-like Fermi surface (Weyl point). (b) Type II Weyl semimetal with a Fermi surface consisting of conical electron and hole pockets connected at the Weyl point.

where σ^i are again 2×2 Pauli matrices, and $\delta\mathbf{k} = \mathbf{k}_0 - \mathbf{k}$. If the Fermi level is close to the band crossing point, the low-energy excitations of the system, and therefore the corresponding quasiparticles, are described by this effective Hamiltonian. Moreover, if we set $\mathbf{v}_0 \equiv 0$ and $\mathbf{v}_i \equiv v_0 \mathbf{e}_i$ $(i = x, y, z)$ with $v_0 = \pm c$, we immediately see that the Hamiltonian in Eq. (5.8) is equivalent to the Weyl Hamiltonian H_W from Eq. (5.7). Hence, the quasiparticle excitations of the system are described by a linear Weyl equation, which is the reason why such systems are dubbed *Weyl semimetals*.

By comparing Eq. (5.8) with the Weyl Hamiltonian H_W, we find that the $\mathbf{v}_i$ correspond to effective velocities of the Weyl particles in a potentially anisotropic space. Their energy spectrum is represented by a three-dimensional cone, a so-called Weyl cone [see Fig. 5.1(a)]. The corresponding bulk Fermi surface consists of a single point or, if the Fermi level does not coincide with the Weyl node, of a closed Fermi surface. Furthermore, the chirality of the Weyl fermions can be derived from their velocities through $C = \operatorname{sign}(\mathbf{v}_x \cdot \mathbf{v}_y \times \mathbf{v}_z)$ [103].

If we ignore the $f_0(\mathbf{k}_0)$ term in Eq. (5.8), which simply corresponds to a constant shift in energy, only the $\mathbf{v}_0$ term does not appear in the original Weyl equation. The reason is that such a term is explicitly forbidden by Lorentz symmetry [162]. However, in a linearized low-energy equation such a term is absolutely allowed and generically appears. More specifically, it leads to a tilt of the Weyl cone in energy-momentum space. This gives rise to a new type of Weyl semimetal which does not have an analogue in high-energy physics [162]. In these so-called *Type II* Weyl semimetals, the Weyl cone is overtilted such that the Fermi level cuts out open electron and hole pockets which are connected at the

Weyl point [see Fig. 5.1(b)]. Correspondingly, Weyl semimetals without this feature are dubbed *Type I* Weyl semimetals.

Let us now have a closer look at the topological properties of Weyl semimetals. A band touching point at $\mathbf{k}_0$, a so-called Weyl node, represents a diabolical point of the Berry connection $\mathbf{A}(\mathbf{k}) = \sum_{n=1}^{N} i\langle u_{n\mathbf{k}}|\partial_{\mathbf{k}}|u_{n\mathbf{k}}\rangle$ of the N occupied bands because at $\mathbf{k}_0$ the Berry connection is not uniquely defined. This gives rise to a nontrivial topology. Indeed, it is easily checked that the integral of $\mathbf{A}(\mathbf{k})$ over any closed surface in momentum space enclosing $\mathbf{k}_0$ is exactly $2\pi C$, where C is the chirality of the Weyl node. In other words, Weyl points represent monopoles of the Berry flux and C is also called *topological charge* [103]. Hence, Weyl nodes are topologically protected bulk features: generic perturbations can only shift the nodes in energy and momentum space without removing them. From the view point of the low-energy theory, isolated Weyl nodes are robust because, in contrast to the Dirac equation, there exists no mass term for the Weyl equation in three dimensions[31]. Weyl nodes can only be created or annihilated pairwise by fusing two Weyl nodes of opposite chirality [163]. Furthermore, the total topological charge of the bulk BZ must vanish due to the Nielson-Ninomiya theorem [88, 164]. As a consequence, Weyl nodes always come in pairs of opposite chirality.

It is important to note that Weyl points in a Weyl semimetal represent *accidental* degeneracies and thus do not require the presence of a particular symmetry. They are intrinsic features of the three-dimensional band structure near the Fermi level which is another reason for their robustness. In contrast, this is not possible in dimensions lower than three without imposing additional symmetries[32]. This was already recognized by Neumann and Wigner [165] who found that, in general, an accidental level crossing of two bands requires at least *three* independently tunable parameters in the absence of any symmetries[33]. This condition is naturally fulfilled in three dimensions where, as we can see from Eq. (5.8), the three momentum components k_x, k_y, k_z play the role of tuning

---

[31] This can be seen as follows: in Eq. (5.8), all of the three linearly independent Pauli matrices and the unit matrix are used to describe a Weyl fermion. These matrices span the entire space of Hermitian 2×2 matrices. Hence, any additional term can only contribute to the already utilized matrices thereby shifting the Weyl node in energy or momentum without the creation of an energy gap.

[32] A famous example in two dimensions is graphene as discussed in a previous chapter. In graphene, the 2D Dirac cones are protected by inversion symmetry. However, an inversion-symmetry breaking mass term, such as a staggered sublattice potential, is able to lift the degeneracy at the Dirac point.

[33] This can be seen very easily in analogy with the Weyl semimetal Hamiltonian from Eq. (5.8): a generic two-level crossing is described by the Hamiltonian $H = a_1\sigma_x + a_2\sigma_y + a_3\sigma_z$ with an energy gap given by $\Delta E = 2\sqrt{a_1^2 + a_2^2 + a_3^2}$. Therefore, in order to have a degeneracy in the spectrum, we need to achieve that $a_1 = a_2 = a_3 = 0$ simultaneously. In general, this can only be accomplished if all three parameters a_i can be tuned independently.

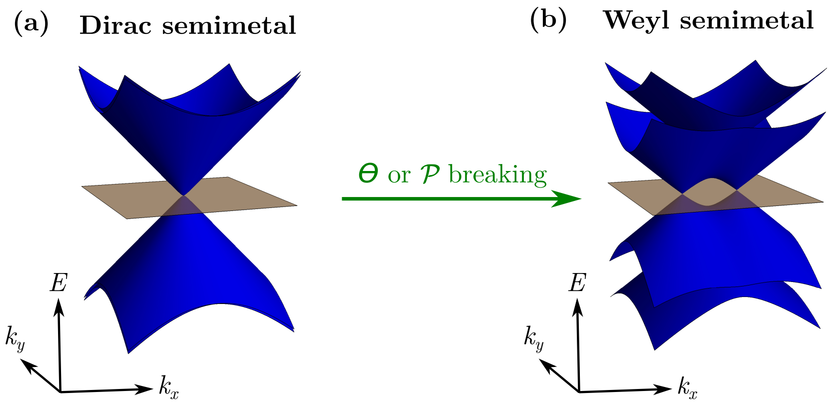

Figure 5.2: Transition from Dirac semimetal to Weyl semimetal ($k_z = 0$): (a) Dirac semimetal with $\mathcal{P}$ and Θ symmetry consisting of two copies of identical Weyl cones. (b) Breaking $\mathcal{P}$ or Θ symmetry separates the Weyl cones in momentum space.

parameters in the BZ.

Although the protection of Weyl degeneracies is intrinsic and does not rely on symmetries, the existence of Weyl nodes generally demands the absence of certain symmetries [103]. This can be seen as follows: consider a system of spin-1/2 electrons with time-reversal symmetry Θ and inversion symmetry $\mathcal{P}$. For such a system, we have $[\Theta, \mathcal{P}] = 0$, $\Theta^2 = -1$, $\mathcal{P}^2 = 1$, and both Θ and $\mathcal{P}$ reverse the momentum, i.e., $\mathbf{k} \rightarrow -\mathbf{k}$. The presence of both symmetries allows us to form a new antiunitary operator $\tilde{\Theta} = \mathcal{P}\Theta$ with $\tilde{\Theta}^2 = -1$ and $\mathbf{k} \rightarrow \mathbf{k}$. This gives rise to a Kramers theorem with respect to $\tilde{\Theta}$ with Kramers doublets at every $\mathbf{k}$. Hence, in the presence of both time-reversal and inversion symmetry all energy bands are at least doubly degenerate and it is not possible to have an accidental level crossing of only two non-degenerate bands. Consequently, in order to create a Weyl semimetal we have to break at least one of these symmetries. This is also reflected in the fact that Weyl nodes are always created pairwise: from the theoretical point of view, one typically induces an energy-gap closing in a time-reversal invariant centrosymmetric system. This results in an isolated fourfold degeneracy whose low-energy theory is described by a 3D Dirac equation[34] [see Fig. 5.2(a)]. This 3D *Dirac point* can be viewed as a pair of Weyl fermions with opposite chirality. Upon breaking time-reversal or inversion-symmetry the two Weyl fermions are then separated in momentum or energy leading to two isolated Weyl nodes as illustrated in Fig. 5.2(b).

There have been several proposals for centrosymmetric magnetic Weyl semimetals such as the pyrochlore iridates $A_2Ir_2O_7$ (with A=Y or a rare earth element Eu, Nd, Sm, or Pr) [158], or the Co-based magnetic Heusler compounds VCo_2Al and VCo_2Ga [166]. However, experimental evidences are still sparse [103].

---

[34] Such a system is called a 3D *Dirac semimetal*. Its Dirac point is in general not stable against generic perturbations unless additional symmetries are imposed [103].

On the contrary, the complementary approach has been much more successful. A large number of time-reversal invariant Weyl semimetals, which will be the focus of this chapter, have been theoretically proposed and confirmed in experiments [103]. The most famous examples are TaAs, TaP, NbAs and NbP [167–173]. Also candidates for time-reversal invariant Type II Weyl semimetals have been put forward, such as WTe_2 and $MoTe_2$ [162, 174]. A promising way to search for new time-reversal symmetric Weyl semimetals is to use their close connection to 3D topological insulators with broken inversion symmetry: typically, stable Weyl semimetal phases appear at the transition between two such insulating phases with different topology [175].

Moreover, time-reversal symmetry imposes restrictions on the number of Weyl nodes. Under time reversal, a Weyl node is mapped onto a different Weyl node with the same chirality. According to the Nielson-Ninomiya theorem, this requires the presence of two other Weyl nodes with opposite charge to compensate the topological excess charge. Thus, in time-reversal symmetric Weyl semimetals the total number of Weyl points must be $4n$ with n being an integer [163].

In general, Weyl semimetals give rise to a number of intriguing physical effects [103], such as the chiral anomaly [176], an anomalous Hall effect [177], or the mixed axial-gravitational anomaly [178]. Furthermore, their bulk-boundary correspondence is at the basis of one of the most interesting hallmarks of Weyl semimetals: the existence of *open* constant-energy contours in the surface BZ of the material which are called *Fermi arcs* [158].

5.1.3 Topological surface states: Fermi arcs

In the surface BZ of a Weyl semimetal, Fermi arcs connect the surface projections of Weyl nodes with opposite chiralities [see Fig. 5.3(a)]. The presence of surface states is directly linked to the nontrivial topology of the Weyl nodes as we are going to explain below by closely following Ref. [158].

Without loss of generality, let us consider the (001) surface of a Weyl semimetal. Let $\mathcal{C}$ be an arbitrary closed curve around the surface projection of a bulk Weyl point as illustrated in Fig. 5.3(a). The curve is parameterized as $\mathbf{k}_s = [k_x(s), k_y(s)]$ with $s \in [-\pi, \pi)$. Let us now recover the bulk BZ. By adding the bulk momentum $k_z \in [-\pi, \pi)$ as an additional parameter, we promote our closed curve $\mathcal{C}$ in the surface BZ to a 2-torus $\mathbb{T}$ in the bulk BZ

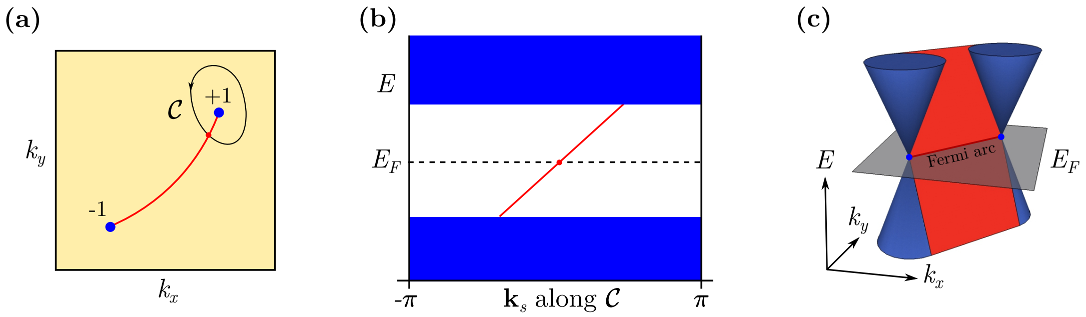

Figure 5.3: (a) Surface BZ of a Weyl semimetal with Weyl node projections (blue dots) of charge ±1 connected by a Fermi arc (red line). A closed path $\mathcal{C}$ enclosing one of the Weyl nodes has to cross a Fermi arc. (b) Cut through the surface BZ along $\mathcal{C}$ which can be viewed as the edge BZ of a quantum Hall insulator where chiral edge states (red line) connect the bulk energy bands (blue continuum). (c) Typical low-energy surface spectrum of a Weyl semimetal with surface projections of Weyl cones (blue) and surfaces states (red) forming a Fermi arc at the Fermi energy E_F (grey plane).

enclosing the bulk Weyl point. On this 2D momentum-space surface the system is gapped. Hence, the Hamiltonian $H(s, k_z) = H(\mathbf{k}_s, k_z)$ on this submanifold can be interpreted as the bulk Hamiltonian of a 2D insulating system in the effective BZ spanned by s and k_z. If the torus is small enough to enclose only one bulk Weyl point, the corresponding surface integral of the Berry connection $\mathbf{A}(\mathbf{k})$ will be proportional to the chirality C of the enclosed Weyl point. Hence, the 2D system described by $H(s, k_z)$ is a quantum Hall insulator with Chern number $n \equiv C$.

By bulk-boundary correspondence, this 2D system will have $|n|$ chiral edge states crossing the Fermi level. In particular, let us pick a boundary that breaks translational symmetry in the z direction only. The corresponding edge BZ of this geometry is then a subset of the original surface BZ of our Weyl semimetal. More specifically, the edge BZ of $\mathbb{T}$ coincides precisely with the curve $\mathcal{C}$. Therefore, there have to be $|n| = |C|$ surface states at E_F along the curve $\mathcal{C}$ in the surface BZ [see Fig. 5.3(b)]. Since $\mathcal{C}$ was arbitrary, there must be $|C|$ surface states for any closed curve around the same Weyl node as long as no other Weyl node is crossed. By continuity, the collection of these states form $|C|$ Fermi arcs beginning at the Weyl node and terminating at different Weyl nodes with opposite chiralities [see Fig. 5.3(c)].

Note that the Fermi arcs are *open* energy contours. Such a feature is not possible in the bulk of a 2D material as it would violate the continuity requirement on the Fermi surface. In a Weyl semimetal, this violation is circumvented due to the presence of the bulk Weyl nodes: Fermi arcs associated with opposite surfaces are connected through the bulk Weyl nodes and thus form a closed Fermi surface globally.

5.2 Generic coexistence of Fermi arcs and Dirac cones on the surface of time-reversal invariant Weyl semimetals

In the previous section, we have introduced surface Fermi arcs as one of the characteristic features of Weyl semimetals. Their existence is demanded by bulk-boundary correspondence as they connect Weyl points of opposite chiralities on the surface.

Recently, it has been theoretically proposed that these Fermi arcs can, under certain conditions, coexist with surface Dirac cones at the interface between a time-reversal broken Weyl semimetal and a 3D time-reversal invariant topological insulator [179,180]. The close relation between Dirac cones and Fermi arcs is also manifest in the fact that Dirac cones can be created by fusing Weyl points in a specific manner as it occurs during the transition between two topologically distinct insulating phases [163].

Given these findings, it is natural to ask whether it is possible to realize both Dirac fermions *and* Weyl fermions in a single material. In the following, we are going to show that in *time-reversal symmetric* Weyl semimetals the coexistence of Dirac cones and Fermi arcs actually arises naturally. The results presented below are based on Ref. [181].

5.2.1 Topological invariants for time-reversal invariant Weyl semimetals

In Section 5.1.3, we have explained how the nontrivial topological charge of Weyl nodes leads to the existence of Fermi arcs. The key idea was to consider a closed 2D momentum-space surface in the bulk BZ enclosing the Weyl node. This surface was then interpreted as a quantum Hall system with a nontrivial Chern number equal to the Weyl node chirality whose chiral edge states then formed the Fermi arcs.

In view of the following considerations, let us adopt a closely related point of view. For that, we decompose the 3D BZ of a Weyl semimetal in 2D momentum space cuts separating the Weyl points from each other [see Fig. 5.4(a)]. Most of the momentum-space cuts are gapped systems and, as before, we can calculate their Chern number. At the Weyl points, however, the 2D systems undergo a gap closing-reopening phase transition and their Chern

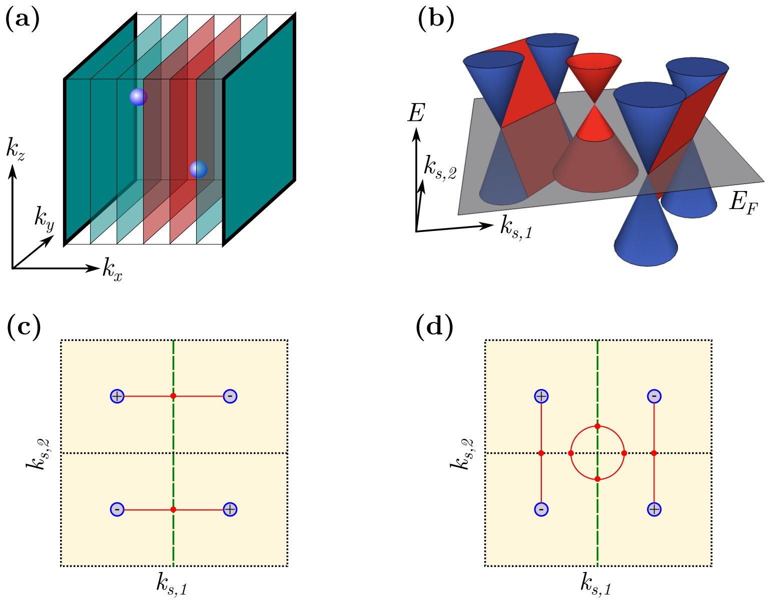

Figure 5.4: (a) The BZ of a WSM as a collection of 2D insulators with zero (green) or nonzero (red) Chern numbers. Weyl nodes (blue spheres) separate planes with different Chern numbers. The bold frames indicate the TRI 2D insulators characterized by a $\mathbb{Z}_2$ invariant. (b) Typical low-energy surface spectrum of a TRI WSM with an additional surface Dirac cone: surface states are shown in red, whereas the surface projections of the 3D bulk Weyl cones are highlighted in blue. (c)–(d) Fermi arc connectivities in the surface BZ of a TRI WSM with four Weyl points indicated by their topological charge ±. The surface projections of the 3D TRI planes are highlighted by dotted black ($\nu = 0$) or dashed green ($\nu = 1$) lines.

number changes. In this way, we can interpret the topological charge of a Weyl node as the change in the Chern number of the collection of gapped 2D systems associated with the 3D BZ of the Weyl semimetal. As in Section 5.1.3, the chiral edge states of the 2D cuts lead to the characteristic surface Fermi arcs of the Weyl semimetal.

Remarkably, time-reversal invariant Weyl semimetals can in general[35] be additionally characterized by six $\mathbb{Z}_2$ invariants [183]. The Chern number of the effective 2D insulators realized by the TRI planes will be zero, but the time-reversal polarizations still allow to characterize the effective 2D systems in terms of a $\mathbb{Z}_2$ topological invariant ν [75]. Contrary to TRI insulators in 3D, where the six ν_i are not independent and can be reduced to four using homotopy arguments [67, 85] – the strong and weak indices of 3D TRI insulators [75, 84] discussed in Sec. 3.1.3 – in a time-reversal invariant WSM all six $\mathbb{Z}_2$

---

[35] An exception are Kramers-theorem enforced Weyl semimetals, where the Weyl points are pinned to time-reversal invariant momenta. However, this can only occur in materials with chiral space groups [182] which we explicitly exclude from this study.

invariants are independent. The reason is the breakdown of the 3D homotopy argument [67,85] due to the gapless nature of Weyl semimetals. In particular, the strong topological index, as defined in Sec. 3.1.3, is no longer well defined and, hence, there are no longer additional constraints on the values of the six $\mathbb{Z}_2$ invariants.

For a generic surface of a WSM, by bulk-boundary correspondence the ν_i determine whether an even ($\nu_i = 0$) or odd ($\nu_i = 1$) number of Kramers pairs of surface states cross the Fermi level along the surface projection of the i-th TRI plane. This imposes restrictions on the structure of the surface Fermi surface but still does not uniquely determine it. Figs. 5.4(c) and (d) sketch two allowed but qualitatively very different surface Fermi surfaces of a time-reversal invariant WSM in which the $\mathbb{Z}_2$ invariants of the planes $k_{s,2} = 0, \pi$ and $k_{s,1} = \pi$ have the trivial value 0, whereas the invariant associated with the plane at $k_{s,1} = 0$ has the nontrivial value 1. A surface Fermi surface consisting of only two open arcs, connecting Weyl points as depicted in Fig. 5.4(c), is entirely allowed. However, different pairs of Weyl points of opposite chirality can be connected only if an additional Fermi pocket, enclosing a time-reversal invariant point, is created [see Fig. 5.4(d)]. The latter situation is a unique signature of Fermi arcs coexisting with a surface Dirac cone [see Fig. 5.4(b)], which is an exclusive feature of TRI Weyl semimetals. This surface Dirac cone is *protected* for a given connectivity of the Fermi arcs since its corresponding Fermi pocket can only be removed by connecting it to the Fermi arcs, which would lead to another reconnection of the Weyl nodes. We emphasize that while this transition does not change the $\mathbb{Z}_2$ invariants of the time-reversal invariant WSM, the change of the Fermi surface topology does imply a Lifshitz transition on the surface of the material [184,185]. Before studying this Lifshitz transition in an explicit Hamiltonian, we will first determine the generic consequences for quasiparticle interference (QPI) which are relevant for scanning tunneling experiments. We will then compare this to explicit QPI calculations for the explicit Hamiltonian in Sec. 5.2.3.

5.2.2 Phenomenological quasiparticle-interference patterns

Having established the coexistence of Fermi arcs and Dirac cones in a time-reversal invariant WSM, we now proceed to analyze their fingerprints in QPI patterns, which can be observed in scanning tunneling spectroscopy (STS) experiments [186–190]. In STS experiments, the differential conductance between the tip and the surface of a material is used to obtain a spatial map of the electronic local density of states (LDOS) at a certain energy and temperature [186, 191]. Impurities lead to characteristic modulations in the LDOS

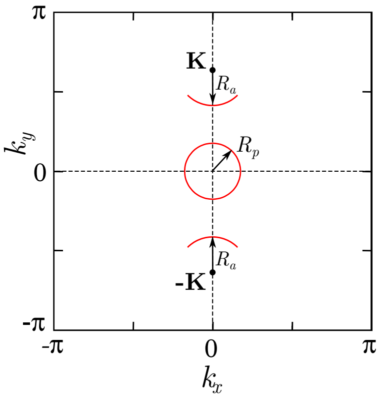

Figure 5.5: Idealized surface Fermi surface of a time-reversal symmetric Weyl semimetal: two Fermi arcs with center of curvature at ±**K** and radius of curvature R_a, and a circular Fermi pocket originating from a surface Dirac cone centered at $\bar{\Gamma}$ with radius R_p.

that depend strongly on the electronic structure of the host material and on the properties and distribution of impurities. In particular, impurities break translational symmetry on the surface thereby enabling scattering between states with the same energy $E = E_F$ but different momentum $\mathbf{k}$ and $\mathbf{k}'$. The modulations in the LDOS can be analyzed with Fourier-transform STS. In this way, the Fourier transformed LDOS is interpreted in terms of the QPI between diagonal states of the clean host material [186, 191].

Typically, the Fourier transformed LDOS is approximated by the joint density of states (JDOS) [186, 191], which is expressed as

$$J(\mathbf{q}, E) = \int d^2k \, A(\mathbf{k}+\mathbf{q}, E)A(\mathbf{k}, E), \tag{5.9}$$

$$A(\mathbf{k}, E) = -\frac{1}{2\pi} \operatorname{Im}\{\operatorname{Tr}[G_s(\mathbf{k}, E)]\}, \tag{5.10}$$

where $A(\mathbf{k}, E)$ is the spectral function, $G_s(\mathbf{k}, E)$ is the surface Green's function, and $\mathbf{k}$ is the momentum parallel to the surface.

In order to obtain a phenomenological picture of the QPI patterns on the surface of Weyl semimetals, we consider an idealized Fermi surface consisting of a circular Fermi pocket around the origin that is surrounded by an open Fermi arc of constant curvature and its time-reversal partner (see Fig. 5.5). Furthermore, we assume a constant spectral density.

The spectral function of the system can then be decomposed as $A = A_p + A_{a_1} + A_{a_2}$ with

$$\begin{aligned} A_p(\mathbf{k}) &= \int_0^{2\pi} d\alpha'\, \delta(\mathbf{k} - R_p\,(\cos\alpha', \sin\alpha')]), && (5.11) \\ A_{a_{1,2}}(\mathbf{k}) &= \int_\alpha^{\alpha+\Delta\alpha} d\alpha'\, \delta(\mathbf{k} \mp [\mathbf{K}{+}R_a\,(\cos\alpha', \sin\alpha')]). && (5.12) \end{aligned}$$

A_p is the spectral function associated with the circular Fermi pocket of radius R_p. $A_{a_{1,2}}$ are the contributions from the two Fermi arcs. The arcs are cut out from circles centered at $\pm\mathbf{K}$ with radius R_a. The end points of the arcs are at angles $\pm\alpha$ and $\pm\alpha \pm \Delta\alpha$. With this decomposition, the JDOS of Eq. (5.9) becomes

$$\begin{aligned} J(\mathbf{q}) &= \int d^2k\, [\underbrace{A_{a_1}(\mathbf{k}+\mathbf{q})A_{a_1}(\mathbf{k}) + A_{a_2}(\mathbf{k}+\mathbf{q})A_{a_2}(\mathbf{k})}_{\text{intra-arc}} \\ &\quad + \underbrace{A_{a_1}(\mathbf{k}+\mathbf{q})A_{a_2}(\mathbf{k}) + A_{a_2}(\mathbf{k}+\mathbf{q})A_{a_1}(\mathbf{k})}_{\text{inter-arc}} + \underbrace{A_p(\mathbf{k}+\mathbf{q})[A_{a_1}(\mathbf{k}) + A_{a_2}(\mathbf{k})]}_{\text{arc-pocket}} \\ &\quad + \underbrace{[A_{a_1}(\mathbf{k}+\mathbf{q}) + A_{a_2}(\mathbf{k}+\mathbf{q})]A_p(\mathbf{k})}_{\text{arc-pocket}} + \underbrace{A_p(\mathbf{k}+\mathbf{q})A_p(\mathbf{k})}_{\text{intra-pocket}}]. \qquad (5.13) \end{aligned}$$

We see that there are four different contributions to the total JDOS which can be attributed to scattering events within each Fermi arc (intra-arc), between the Fermi arcs (inter-arc), between Fermi pocket and Fermi arcs (arc-pocket), and within the Fermi pocket (intra-pocket). Inserting Eqs. (5.11) and (5.12), each individual contribution involves integrals of the form

$$\int d^2k \int d\alpha'\, d\alpha''\, \delta[\mathbf{k} + \mathbf{q} - \mathbf{u}_i(\alpha')]\, \delta[\mathbf{k} - \mathbf{u}_j(\alpha'')]. \qquad (5.14)$$

This can be written as a convolution of two δ functions, $\delta * \delta$. By using that $\delta * \delta \equiv \delta$, the integral becomes

$$\int d\alpha'\, d\alpha''\, \delta[\mathbf{q} + \mathbf{u}_i(\alpha')]\, \delta[\mathbf{u}_j(\alpha'')]. \qquad (5.15)$$

In general, this integral cannot be simplified further. To obtain qualitative results for the JDOS, we therefore approximate the appearing δ functions of the form $\delta(\mathbf{k}) \equiv \delta(k_x)\delta(k_y)$ by Lorentz functions

$$\delta_\epsilon(k_i) = \frac{1}{\pi}\frac{\epsilon}{k_i^2 + \epsilon^2}, \quad \epsilon \ll 1, \qquad (5.16)$$

with height $1/\sqrt{\epsilon}$ and width $\sqrt{\epsilon}$. The ensuing integrals are then solved numerically. The results for the different JDOS contributions are shown in Fig. 5.6. Note that in each panel the color scale is renormalized with respect to the considered contribution.

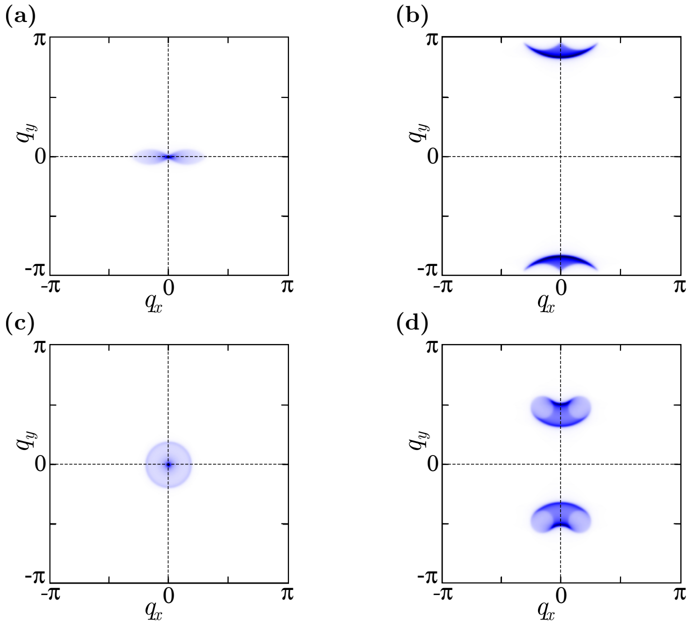

Figure 5.6: JDOS contributions from an analytical treatment: (a) intra-arc scattering, (b) inter-arc scattering, (c) intra-pocket scattering, (d) arc-pocket scattering. Note that in each panel the color scale is renormalized with respect to the considered JDOS contribution. The color scale ranges from white (small JDOS), over blue to black (high JDOS).

Fig. 5.6(a) shows the intra-arc JDOS contributions. We can clearly see a pinch point at $\mathbf{q} = 0$ which is in the center of a dumbbell-shaped feature aligned with the q_x axis. This is the unique QPI pattern of an open Fermi arc. Since the considered Fermi surface consists of two of those arcs, we get an additional JDOS (inter-arc) contribution originating from scattering between the arcs. These features appear around the q_y axis at $\mathbf{q}$ vectors corresponding to scattering vectors between the two arcs in the BZ [see Fig. 5.6(b)].

The intra-cone JDOS contribution, shown in Fig. 5.6(c), is strongly peaked at $\mathbf{q} = 0$ and falls off rapidly away from the center. The resulting pattern is rotationally symmetric reflecting the symmetry of the Fermi pocket. The feature has a sharp boundary with a slightly enhanced intensity at $|\mathbf{q}|$ values corresponding to the diameter of the underlying Fermi pocket. This is due to scattering events from opposing states of the Fermi pocket.

In Fig. 5.6(d) we present the arc-pocket JDOS contribution which is characteristic of the coexistence of open Fermi arcs and closed Fermi pockets. It therefore represents the universal QPI pattern of Weyl semimetals with additional surface Dirac cones. The kidney-shaped features appear around the q_y axis at $\mathbf{q}$ vectors corresponding to scattering vectors that connect the open Fermi arcs to the closed Fermi pocket.

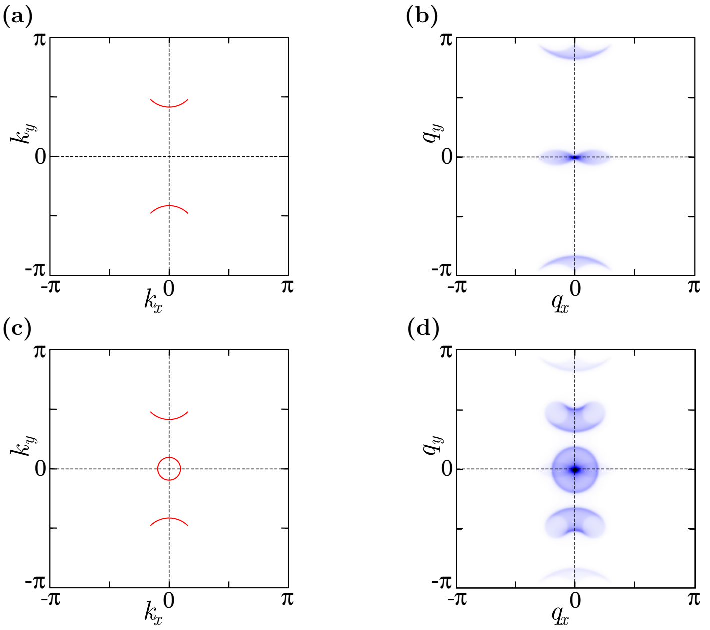

Figure 5.7: JDOS contributions from an analytical treatment: (a) Fermi surface consisting of two Fermi arcs only. The corresponding JDOS in (b) shows the characteristic pinch point at $\mathbf{q} = 0$. (c) A Fermi surface with additional circular Fermi pocket shows additional features in the JDOS as shown in (d). Most remarkable are the kidney-shaped features stemming from scattering between Fermi pocket and Fermi arcs.

Finally, Fig. 5.7 shows the accumulated JDOS spectra and the corresponding idealized surface Fermi surfaces for the cases with [Figs. 5.7(a) and (b)] and without an additional Fermi pocket [Figs. 5.7(c) and (d)].

5.2.3 The coexistence in a tight-binding model formulation

Next, we introduce a tight-binding model for a time-reversal invariant WSM to investigate, on a microscopic basis, the coexistence of surface Dirac cones and Fermi arcs. The tight-binding model is defined on a cubic lattice and reads

$$\begin{aligned} H(\mathbf{k}) \;&=\; a\,(\sin k_x\,\tau^1 s^3 + \sin k_y\,\tau^2 s^0) + \beta\,\tau^2 s^2 + d\,\tau^2 s^3 + \alpha \sin k_y\,\tau^1 s^2 \\ &\quad + [t\cos k_z + 2b(2-\cos k_x - \cos k_y)]\,\tau^3 s^0 + \lambda \sin k_z\,\tau^0 s^1, \end{aligned} \tag{5.17}$$

where the s^i are Pauli matrices in spin space, whereas the τ^i are Pauli matrices associated with additional orbital degrees of freedom. The lattice constant has been set to unity. The Hamiltonian is based on a general tight-binding model introduced in Ref. [187]. The model preserves time-reversal symmetry with $\Theta = i\tau^0 s^2 K$, $\mathbf{k} \to -\mathbf{k}$, where K is complex conjugation. The β, d and λ terms break inversion symmetry with the inversion operator $P = \tau^3 s^0$, $\mathbf{k} \to -\mathbf{k}$, which is a necessary condition for the existence of a Weyl semimetal phase.

In the following, we will analyze $H(\mathbf{k})$ in a finite geometry. For the analysis of the energy spectrum, we choose the system to have open boundary conditions in the y direction and periodic boundary conditions in the x and z direction. This gives rise to two (010) surfaces. The energies of the system are then obtained from exact numerical diagonalization of the corresponding tight-binding Hamiltonian in mixed position-momentum space associated with Eq. (5.17). The topological charge of the bulk Weyl nodes is obtained from the bulk Hamiltonian by integration of the Berry flux over the surface of a BZ volume containing the Weyl node. The $\mathbb{Z}_2$ invariants ν_i of the time-reversal invariant planes are instead computed using a Wannier-center formulation of the topological invariant (see Appendix B). Furthermore, the JDOS corresponding to the (010) surface of a semi-infinite slab of the system described by Eq. (5.17) will be computed. For that, the (010) surface Green's function of the system is determined using an iterative scheme (see Appendix C). In all calculations the Fermi energy is assumed to be at $E_F = 0$.

To demonstrate the coexistence of surface Dirac cones and Fermi arcs in $H(\mathbf{k})$, we start from a particular Weyl semimetal phase and, first, vary the parameter β. The results are presented in Fig. 5.8. With the chosen parameters, the model features four bulk Weyl points of charge ±1 which are all located away from the time-reversal invariant planes of the bulk BZ. Hence, all six $\mathbb{Z}_2$ invariants are well-defined. In particular, we find that $\nu_{k_z=\pi} = 1$ while the remaining five $\mathbb{Z}_2$ invariants are zero. At the (010) surface we therefore expect an odd number of Kramers pairs at $k_z = \pi$ and an even number of Kramers pairs at $k_z = 0$ and $k_x = 0, \pi$. Furthermore, the surface projections of the four Weyl nodes appear in different quadrants of the surface BZ.

For large values of β, we find that Fermi arcs connect two Weyl nodes in the left half-plane and two Weyl nodes in the right half-plane [see Fig. 5.8(a)]. The fact that the Fermi arcs cross only the line $k_z = \pi$ is in agreement with the values of the topological invariants. In Fig. 5.8(b), the corresponding JDOS is shown. We see an elongated "figure-eight" feature aligned with the q_z axis and two crescent-shaped patterns parallel to it, which occur at $\mathbf{q}$ values corresponding to the mutual distance of the Fermi arcs in the surface BZ.

By decreasing the parameter β, the Fermi arcs are bent towards each other until they intersect at a critical value of β [see Fig. 5.8(c)]. This point corresponds to the Lifshitz

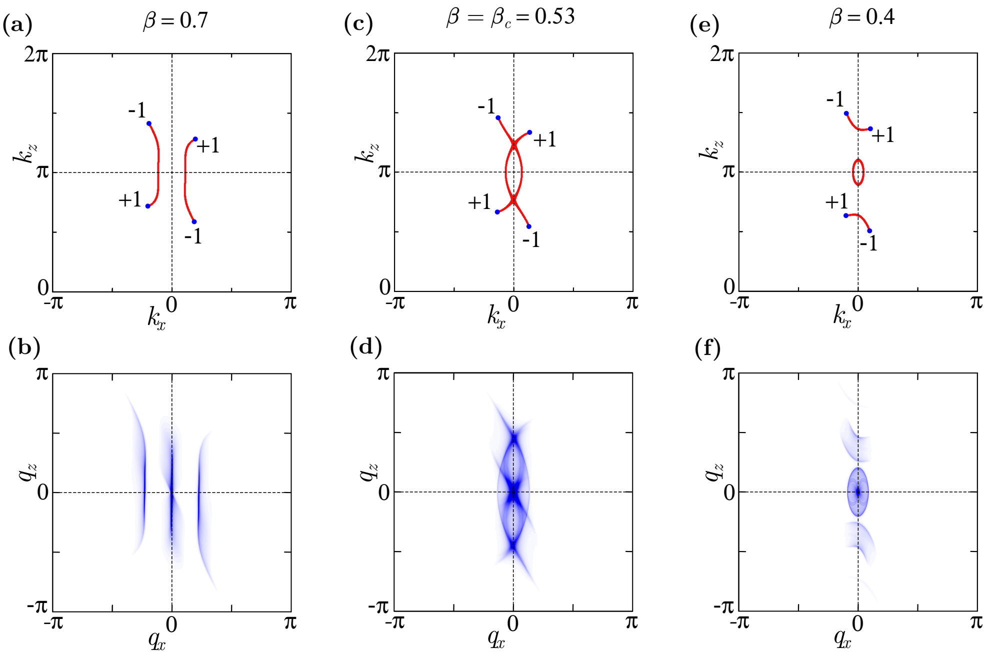

Figure 5.8: Fermi surfaces and JDOS for (010) surfaces in the tight-binding model with $a = b = 1$, $t = 1.5$, $\alpha = 0.3$, $d = 0.1$, $\lambda = 0.5$, and $E_F = 0$: the first row shows the Fermi surfaces for different values of the parameter β. The bulk Weyl nodes are highlighted in blue and their topological charge is indicated. Surface states are highlighted in red. The second column shows the corresponding JDOS spectra. In (f), the kidney-shaped features indicative of the coexistence of Fermi arcs and Dirac cones are clearly visible in the JDOS. Also note how the Fermi-surface topology changes with β while passing a surface Lifshitz transition at $\beta = \beta_c \approx 0.53$.

transition at which the connectivity of the Fermi arcs changes. Note that the position of the Weyl nodes has barely changed. A further decrease in the parameter β reveals the coexistence of Dirac cones and Fermi arcs [see Fig. 5.8(e)]: surface Fermi arcs connect two Weyl nodes in the upper half-plane and two Weyl nodes in the lower half-plane of the surface BZ. In addition to the open-arc features, we find an elliptical Fermi pocket of surface states around the $\bar{Z}$ point of the surface BZ. The existence of the Fermi pocket is required for this particular connectivity of Weyl nodes to satisfy the number of surface states imposed by the topological invariants ν_i which have not changed during the Lifshitz transition.

The JDOS of this configuration is in perfect agreement with the analytical considerations above [see Fig. 5.8(f)]: we find the elliptical inter-pocket feature with a pronounced central peak around the origin whose semi-axes are twice as large as those of the associated Fermi pocket in the surface BZ. We do not clearly see a characteristic intra-arc feature, most

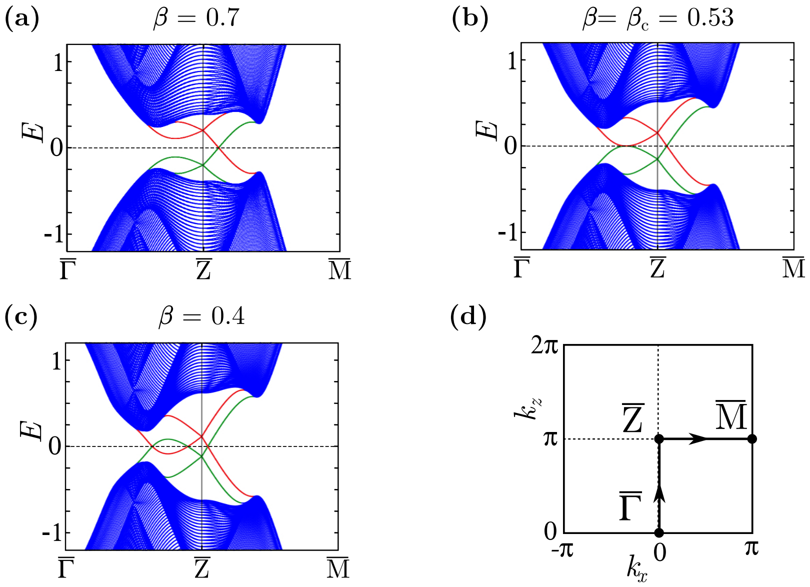

Figure 5.9: Surface energy spectra along high-symmetry lines in the tight-binding model with $a = b = 1$, $t = 1.5$, $\alpha = 0.3$, $d = 0.1$, $\lambda = 0.5$: (a)–(c) energy spectra for different values of the parameter β. Bulk-like states are highlighted in blue, surface states are highlighted in red and green indicating different surfaces. The Fermi energy is at $E_F = 0$ (dashed line). (d) High-symmetry path through the surface BZ corresponding to the displayed energy spectra.

likely because its intensity is too weak as compared to the Fermi pocket features. Also the inter-arc features are barely visible due to the small size of the Fermi arcs. However, their position and shape agree with the expectation from our simple analytical consideration. Most importantly, we find the kidney-shaped features indicative of scattering between the Fermi arcs and the Fermi pocket. As expected, the broadening equals the size of the Fermi pocket whereas their position corresponds to the distance between Fermi pocket and Fermi arcs. The comparison of Figs. 5.8(b) and (f) shows that the different Fermi arc connectivities are reflected in distinct universal JDOS features.

In addition, Fig. 5.9 presents energy spectra along high-symmetry lines through the k_x-k_z surface BZ, which are indicated in Fig. 5.9(d). Recall that for $\beta = 0.7$ the surface Fermi surface consists of two Fermi arcs only. They cross the $k_z = \pi$ axis in two points which are related by time reversal. The corresponding energy spectrum along $\bar{\Gamma}\bar{Z}$ and $\bar{Z}\bar{M}$ is shown in Fig. 5.9(a). For the sake of clarity, let us focus on surface states associated with only one of the two surfaces. We see that there is an in-gap surface Kramers doublet at $\bar{Z}$, relatively far away from the Fermi energy, which is protected by time-reversal symmetry. Away from this point, the doublet is split but the ensuing non-degenerate states evolve

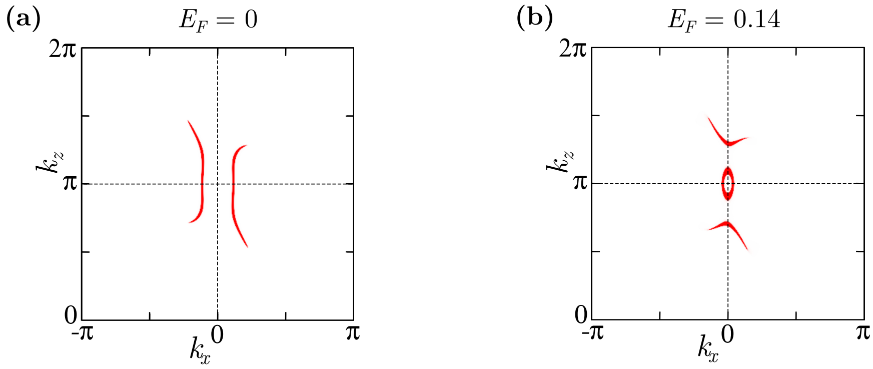

Figure 5.10: Surface spectral weight for the (010) surface in the tight-binding model with $a = b = 1$, $t = 1.5$, $\alpha = 0.3$, $d = 0.1$, $\lambda = 0.5$ and $\beta = 0.7$. Note that the Fermi energy E_F is varied while the parameter β is fixed. We can see how the Fermi arc connectivity is changed by changing the Fermi energy.

differently depending on the considered direction in **k** space. Along $\bar{\Gamma}\bar{Z}$ both surface bands terminate at the bulk conduction/valence band. On the contrary, along $\bar{Z}\bar{M}$ one band terminates at the conduction band whereas the other terminates at the valence band. By bulk-boundary correspondence, this behavior is in agreement with the topological invariants of the 2D bulk systems associated with these lines.

By decreasing β, the Kramers doublet at $\bar{Z}$ moves closer to the Fermi energy. At the Lifshitz transition [see Fig. 5.9(b)], one of the surface bands along $\bar{\Gamma}\bar{Z}$ intersects the Fermi-energy plane tangentially. This is the point where the topology of the Fermi surface changes: below a critical β_c, the Kramers doublet, whose low-energy spectrum is a 2D Dirac cone, is close enough to the Fermi-energy plane to cut out a circular Fermi pocket [see Fig. 5.9(c)]. To preserve the evenness of the number of crossings, there also has to be a second crossing along $\bar{\Gamma}\bar{Z}$. In contrast, the number of $E = 0$ states along $\bar{Z}\bar{M}$ has not changed. This leads to the formation of new Fermi arcs which only cross the $k_x = 0$ line of the surface BZ.

Furthermore, note that the Dirac cone appearing on the surface of the considered Weyl semimetal has a peculiar feature: along one direction, here $\bar{Z}\bar{M}$, it connects the bulk valence to the bulk conduction band, as on the surface of a topological insulator. However, along the perpendicular direction, here $\bar{\Gamma}\bar{Z}$, the Dirac cone is connected to the bulk conduction band (or to the bulk valence band) only. Such a "dangling" Dirac cone can only appear on the surface of a Weyl semimetal due to the lack of a global relation between the $\mathbb{Z}_2$ invariants.

Finally, we are going to show that the Fermi arc connectivity can also be changed

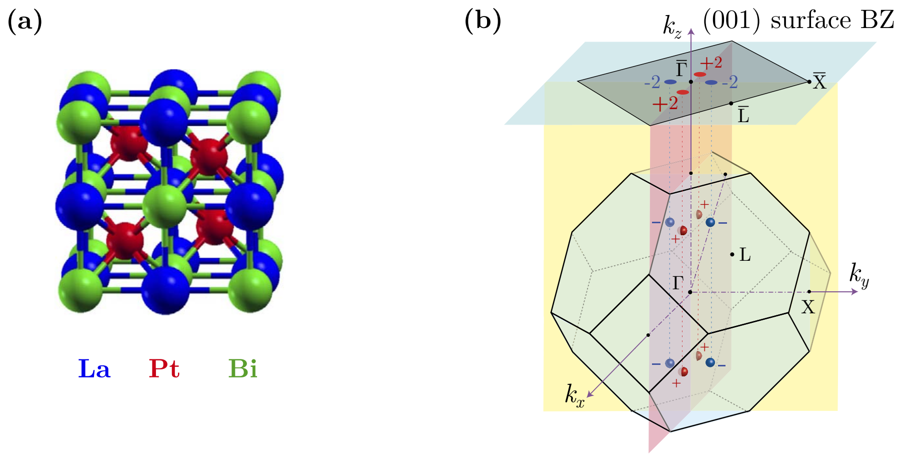

Figure 5.11: (a) Crystal structure of LaPtBi [192]. (b) Bulk BZ of LaPtBi with schematic Weyl point positions (red and blue spheres) and mirror planes (red and yellow planes) [192]. Also shown is the projection of the bulk features onto the (001) surface BZ.

by varying the Fermi energy E_F. For that, we analyze the spectral weight on a (010) surface of the tight-binding model (see Fig. 5.10). Since only the Fermi energy is varied, the progression can be compared to the energy dispersion of the red surface bands in Fig. 5.9(a). For $E_F = 0$, the Dirac point is far above the Fermi energy and there are no surface states at the Fermi energy along $\bar{\Gamma}\bar{Z}$. Hence, there is no Dirac Fermi pocket as can be seen in Fig. 5.10(a). By increasing E_F, the Fermi level moves closer to the Dirac point until it intersects the "dangling" arm of the Dirac cone along $\bar{\Gamma}\bar{Z}$. This is where the Lifshitz transition takes place and the connectivity of the Fermi arcs is changed in the same way as for varying only the parameter β. In particular, a Dirac Fermi pocket is formed [see Fig. 5.10(b)]. The linear dispersion of the corresponding Dirac states can be inferred from Fig. 5.9(a).

5.2.4 Density-functional theory analysis of strained LaPtBi

Having established the coexistence of Dirac cones and Fermi arcs in a generic tight-binding model of TRI Weyl semimetals, we are now going to show its realization in the half-Heusler compound LaPtBi (see Fig. 5.11), which possesses both band inversion [193] and lattice noncentrosymmetry. Under a broad range of in-plane biaxial compressive strain, LaPtBi realizes a Weyl semimetal phase with eight Weyl nodes residing precisely at the Fermi level at stoichiometry composition [192]. LaPtBi has a face-centered cubic crystal structure with a lattice constant of $a_0 = 6.829\text{Å}$ [192]. Furthermore, it preserves time-reversal symmetry

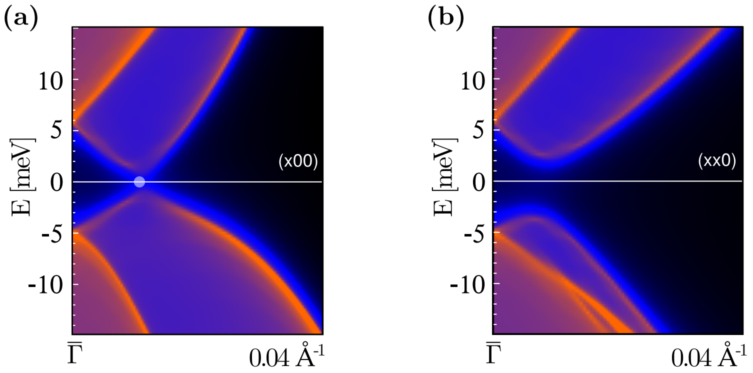

Figure 5.12: Bulk energy bands of LaPtBi projected onto the (001) surface BZ along high-symmetry directions close to the $\bar{\Gamma}$ point: (a) $(x00)$ direction (surface projection of $k_y = 0$ plane). (b) $(xx0)$ direction (surface projection of $k_x = k_y$ plane). Weyl node projections are marked by grey dots.

which makes it a suitable material for our study.

For the density-functional theory calculations[36], the full potential local orbital method in 4-component relativistic mode [194] was employed, using 12^3 points for the tetrahedron integration method. The resulting bands were fitted via maximally projected Wannier functions including a minimum basis of La 6s6p5d4f, Bi 6s6p6d and Pt 6s6p5d. The Wannier model was used to prove the existence of the Weyl points via Berry curvature monopoles and was mapped onto a semi infinite slab with LaBi-plane (001) termination for the determination of the surface spectral function. Furthermore, compressive in-plane strain of $a = 0.99a_0$, $c = 1.02a_0$ was applied following [192].

Due to the concomitant presence of time-reversal and two-fold rotations along the x and y axis, eight Weyl points of charge ±1 are located at the $k_x = 0$ and $k_y = 0$ planes of the bulk BZ. More specifically, the Weyl points positions are $(\pm k_x^*, 0, k_z^*)$ and $(0, \pm k_y^*, k_z^*)$, with $k_x^* = k_y^* = 0.0106\mathring{\text{A}}^{-1}$ and $k_z^* = 0.041\mathring{\text{A}}^{-1}$, which agrees very well with the results in Ref. [192]. In Fig. 5.12, the bulk bands projected onto the (001) surface BZ are shown along the $(x00)$ and $(xx0)$ direction close to the $\bar{\Gamma}$ point. More specifically, the shown slices correspond to surface projections of the $k_y = 0$ and $k_y = k_x$ planes of the bulk BZ. As we can see, there is a bulk gap-closing point at $E = 0$ along $k_y = 0$ [see Fig. 5.12(a)], which corresponds to the projection of two Weyl nodes, whereas the system has a full bulk gap along the $k_y = k_x$ plane [see Fig. 5.12(b)]. Similar observations can be made for the planes with $k_x = 0$ and $k_y = -k_x$ (not shown). Hence, the electronic states in the $k_x = k_y$ and $k_x = -k_y$ planes are all gapped, so that the $\mathbb{Z}_2$ topological invariant in these

---

[36] The calculations were done in collaboration with Dr. Klaus Koepernik [181].

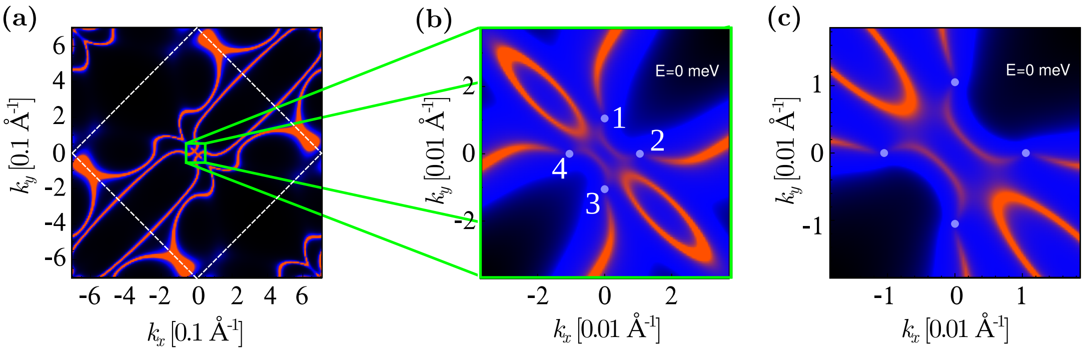

Figure 5.13: Surface spectral weight in the (001) surface BZ of LaPtBi for $E = 0$: (a) entire surface BZ. Borders of the surface BZ are indicated by white dashed lines. The region inside the green square is magnified in panel (b). (b) Magnified region around the $\bar{\Gamma}$ point of the surface BZ. The positions of the projected Weyl nodes are marked by grey dots. For clarity, the Weyl node projections have been labeled by numbers. Panel (c) shows the same region with a higher magnification factor. Note how the surface Fermi arcs connect the Weyl node projections.

time-reversal invariant subsystems is well-defined.

Fig. 5.13 shows the results for the surface spectral weight in the k_xk_y-plane of the LaBi terminated (001) surface of a semi-infinite slab. In panel (a), the full surface Fermi surface of the system in the (001) surface BZ is displayed, whereas panels (b) and (c) show a magnified region around the $\bar{\Gamma}$ point with different zoom factors. The four Weyl point projections along the $k_x = 0$ and $k_y = 0$ lines are highlighted in grey and labeled by numbers for clarity. We note that each point corresponds to the projection of two Weyl nodes with the same charge giving each point an effective Weyl charge of ± 2. Hence, there must be two outgoing Fermi arcs for each Weyl-point projection.

From the shown figures we infer the following Fermi arc connectivity: node 1 is connected to node 2, node 2 is connected to node 3 through the border of the surface BZ, node 3 is connected to node 4, and node 4 is connected to node 1 again through the border of the surface BZ. This means that all Weyl node projections are on *one* closed loop of Fermi arcs. Furthermore, along $k_x = -k_y$ we find two trivial Fermi pockets and there are also two more trivial lines of surface states farther away from the origin.

Let us now analyze the surface Fermi surface in the light of the general coexistence presented earlier. In Fig. 5.14(a), the Fermi level coincides with the Weyl-point energies. As demonstrated above, the time-reversal invariant planes $k_x = k_y$ and $k_x = -k_y$ have full energy gaps in the bulk. Therefore, they represent 2D TRI insulators. The corresponding $\mathbb{Z}_2$ invariant can be inferred, by bulk-boundary correspondence, by simply counting the

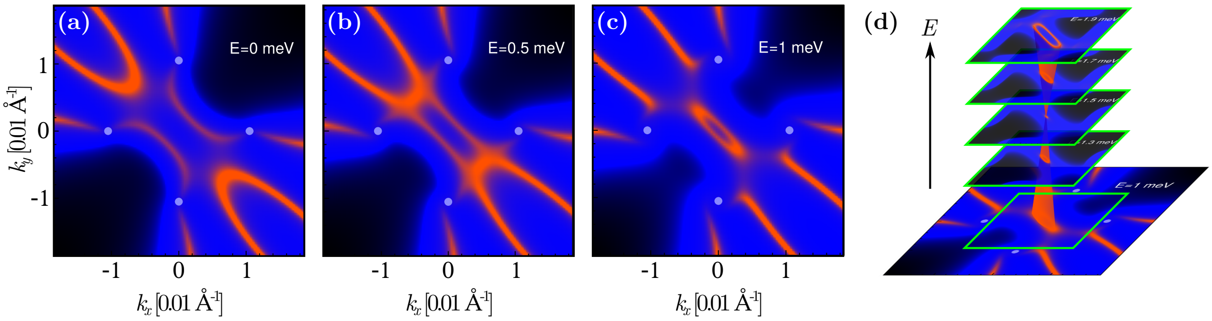

Figure 5.14: Surface Fermi surfaces of LaPtBi with (001) termination: shown is the surface spectral weight. The positions of the four Weyl-point projections are marked by grey dots. The panels display the transition between different Fermi-arc connectivities by varying the Fermi level. Note that the connectivity shown in (c) requires the presence of an additional Fermi pocket around the origin which resembles Fig. 5.8(e). (d) A further increase of the Fermi level reveals that the Fermi pocket indeed originates from a Dirac cone around $\bar{\Gamma}$.

number of Kramers pairs in the (001) surface BZ. We count *one* Kramers pair of surface states for the $k_x = k_y$ plane, and *three* for the $k_x = -k_y$ plane. Hence, both planes represent nontrivial 2D insulators with $\mathbb{Z}_2$ invariant $\nu = 1$. This agrees with the results of an explicit computation of the invariants using the Wannier-center formulation of the $\mathbb{Z}_2$ invariant discussed in Appendix B. As we have discussed above, the $\mathbb{Z}_2$ invariants give rise to restrictions on the Fermi surface topology. In this case, the Fermi arcs connect in a way that does not require an additional Fermi pocket.

Let us now study what happens if we increase the Fermi level, which could for instance be achieved by electron doping. Note that this corresponds to the procedure discussed at the end of the previous section in the context of a tight-binding model. The results are shown in Fig. 5.14. We observe that the Fermi arcs connecting node 1 to node 2 and node 3 to node 4 start to fuse with the trivial Fermi pockets [see Fig. 5.14(b)]. At this point the Weyl nodes reconnect and a Lifshitz transition takes place [compare Fig. 5.14(b) to Fig. 5.8(c)]. Starting from the given Fermi arc connectivity, such a reconnection is only possible by creating an additional Fermi pocket around the origin in order to respect the constraints imposed by the $\mathbb{Z}_2$ invariants of the TRI planes. This is shown in Fig. 5.14(c). Note that the Weyl point projections are indeed connected in a different way. More specifically, node 1 and node 4 are now *directly* connected by two Fermi arcs. The same holds for node 2 and node 3. This means that the Fermi arcs now form *two* closed loops each including two Weyl node projections.

The additional Fermi pocket indeed originates from a Dirac cone as can be seen in

Fig. 5.14(d), where a sequence of surfaces Fermi surfaces close to the $\bar{\Gamma}$ point is shown for different E_F. We observe that the Fermi pocket shrinks as the the Fermi level is increased. At $E_F \approx 1.5\,\mathrm{meV}$, the Fermi pocket has shrunk to a single point, which is the Dirac point. By tuning E_F further, the Fermi pocket expands again. The sequence of Fermi surfaces is accumulated in Fig. 5.14(d) to indicate the resulting surface Dirac cone. This demonstrates the close connection between Fermi arc states and Dirac states on the surface of time-reversal invariant Weyl semimetals.

5.3 Synthesizing Weyl semimetals in weak topological insulator and topological crystalline insulator multilayers

An important cornerstone of the success of Weyl semimetals is the growing number of candidate materials exhibiting Weyl physics. However, available materials typically exhibit a huge number of Weyl nodes [103] making it difficult to test theoretical predictions, which are instead based on models with the minimal number of Weyl nodes allowed by symmetry. Therefore, in view of experimental investigations and potential applications of Weyl semimetals, it is highly desirable to develop new design principles that allow for the controlled preparation of Weyl semimetals.

In this section, we are going to discuss a multilayer design for time-reversal invariant Weyl semimetals based on a heterostructure model introduced by Balents and Burkov [159]. In the latter, only strong TIs with a single Dirac cone per surface as the active layer were considered. Here, we are going to extend this principle to topological materials with an even number of surface Dirac cones. In particular, we will consider two distinct cases: multilayers based on weak TIs with two Dirac cones pinned to TRI momenta, and multilayers based on TCIs with two unpinned Dirac cones. We will show that both systems give rise to time-reversal invariant Weyl semimetal phases with the minimal number of Weyl nodes which exhibit a high degree of tunability. The results presented here closely follow Ref. [195].

5.3.1 Balents-Burkov model for strong topological insulator multilayers

Let us first review the Weyl semimetal model introduced by Balents and Burkov [159]. Generally speaking, it provides an alternative approach to creating new Weyl semimetals based on other topologically nontrivial materials. The idea is to construct a multilayer heterostructure consisting of alternating layers of a 3D strong topological insulator (STI), such as Bi_2Se_3, and layers of an ordinary insulator (OI) [see Fig. 5.15(a)]. Generically, there will be a surface Dirac cone at each STI-OI interface. If the layers are sufficiently thin, Dirac cones from adjacent interfaces are able to hybridize and open an energy gap. Furthermore, magnetic impurities inserted into the STI layers provide a time-reversal breaking mechanism as well as another gap-opening term for the interface Dirac cones. Balents and Burkov found that it is the interplay of these two "mass" terms that leads to the emergence of a stable Weyl semimetal phase.

The multilayer design described above can be modeled by the following Hamiltonian [159],

$$\begin{aligned}\mathcal{H} &= \sum_{\mathbf{k}_\perp, ij} \Big[v_D \sigma_3 (\hat{z} \times \mathbf{s}) \cdot \mathbf{k}_\perp \, \delta_{i,j} + m \sigma_0 s_z \, \delta_{i,j} + \Delta_S \sigma_1 s_0 \, \delta_{i,j} \\ &\qquad + \frac{1}{2} \Delta_D \sigma_+ s_0 \, \delta_{i,j+1} + \frac{1}{2} \Delta_D \sigma_- s_0 \, \delta_{i,j-1} \Big] c^\dagger_{\mathbf{k}_\perp, j} c_{\mathbf{k}_\perp, i}, \end{aligned} \tag{5.18}$$

where $\sigma_{0,1,2,3}$ and $\sigma_\pm = \sigma_1 \pm i\sigma_2$ are Pauli matrices associated with the two (top and bottom) surfaces, $s_{0,x,y,z}$ are Pauli matrices corresponding to the spin degree of freedom, and $\mathbf{k}_\perp$ is the momentum parallel to the interfaces. The first term describes the Dirac cones of the two surfaces, the second represents the magnetic impurities, and the remaining terms model tunneling between Dirac states of adjacent surfaces. In the following, we will briefly summarize the key features of the half-filling phase diagram [159].

For $m = 0$, the model preserves time-reversal symmetry. Balents and Burkov found that the spectrum is gapped for $\Delta_D \neq \Delta_S$ with $\Delta_D < \Delta_S$ being a trivial phase and $\Delta_D > \Delta_S$ being a strong TI phase [see Fig. 5.15(b)]. However, along the line $\Delta_D = \Delta_S$ the system has a 3D Dirac point at $k_z = \pi$. Apparently, this semimetal phase is not stable since any generic perturbation pushes the system into one of the insulating phases.

For $m > 0$, time-reversal symmetry is broken leading to a sizable Weyl semimetal phase in the region $(\Delta_S - \Delta_D)^2 < m^2 < (\Delta_S + \Delta_D)^2$ [see Fig. 5.15(c)]. In this region, the Dirac points are split into two isolated Weyl nodes of chirality $C = \pm 1$ separated along the k_z axis in momentum space. Furthermore, the phase diagram also features insulating phases.

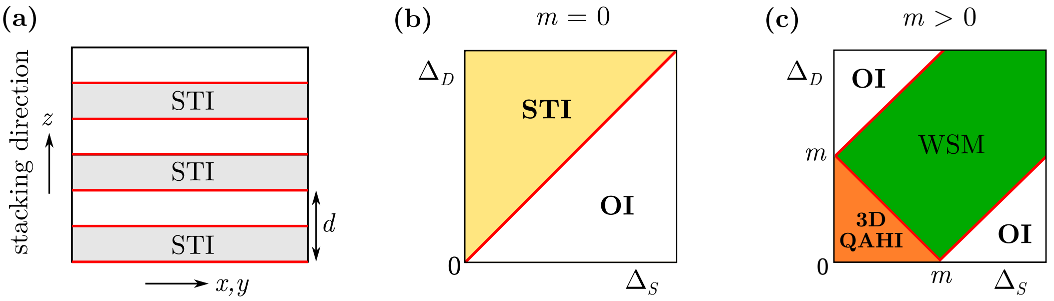

Figure 5.15: (a) Multilayer heterostructure of strong topological insulators (STIs) separated by ordinary insulators (OI) as spacer layers. The interfaces (red) each contribute a single 2D surface Dirac cone. (b) Without magnetic impurities ($m = 0$): two gapped phases (STI and OI) are separated by an unstable Dirac semimetal phase (red line). (b) With magnetic impurities ($m > 0$): a stable Weyl semimetal phase (green) emerges.

For both $\Delta_D - \Delta_S > m$ and $\Delta_S - \Delta_D > m$ the system is in a trivial phase because of the break-down of the STI phase. Around $\Delta_D = \Delta_S = 0$, a new insulating phase emerges. This phase can be understood as a 3D quantum Hall system in the sense that each STI layer has a quantized Hall conductivity of $\sigma_{xy} = e^2/dh$, where d is the distance between two adjacent STI layers.

While this particular model leads to magnetic Weyl semimetals with inversion symmetry, it can also be used to build time-reversal invariant Weyl semimetals [160, 195]. In particular, we are now going to show that this design principle can be extended to build Weyl semimetals from other topologically nontrivial materials, such as weak topological insulators and crystalline topological insulators.

5.3.2 Weak topological insulator multilayer

Let us briefly recall the main properties and features of time-reversal invariant topological insulators in 3D, which we have introduced in Sec. 3.1.3. Time-reversal invariant topological insulators are realizations of gapped topological phases in Altland-Zirnbauer class AII [30, 31, 34]. In three dimensions, gapped systems belonging to this class can be characterized by the four $\mathbb{Z}_2$ topological invariants $\nu_0; (\nu_1\nu_2\nu_3)$ [75, 84]. An insulator with nonzero ν_0 is called strong topological insulator (STI). Its hallmark is the existence of an odd number of protected surface Dirac cones *pinned* to TRI momenta [84].

If the strong index ν_0 is zero but at least one of the weak indices ν_1, ν_2, ν_3 is nonzero, the system is dubbed a weak topological insulator (WTI). In contrast to their strong

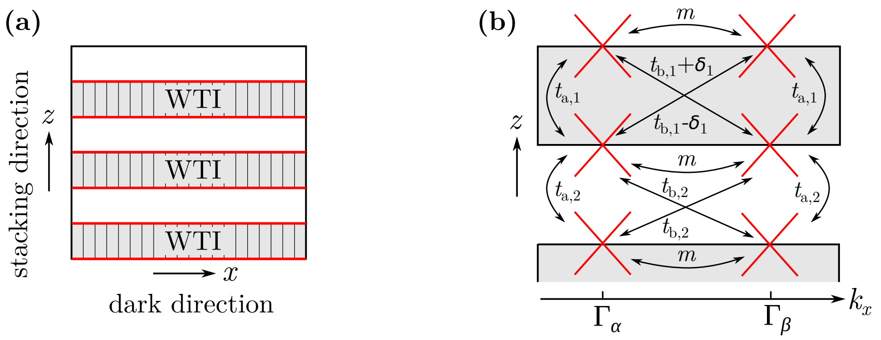

Figure 5.16: Weak TI multilayer: (a) cartoon of the multilayer design. The surfaces of the weak TI layers, which contribute two pinned Dirac cones each, are highlighted in red. The layered structure of the weak TIs is indicated. (b) Schematic of the coupling terms between the surface Dirac cones (red). The Dirac cones are pinned to different TRI momenta Γ_α and Γ_β which are mapped onto each other by translational-symmetry breaking induced by the dimerization mass m.

relatives, WTIs feature an even number of topologically protected, *pinned* Dirac cones only at certain surfaces [84, 104]. More specifically, there exist so-called "dark surfaces" where surface Dirac cones are absent. These are the surfaces whose Miller indices (modulo 2) are identical to the weak indices $(\nu_1\nu_2\nu_3)$. This property is related to the fact that a weak TI is topologically equivalent to a stack of 2D TIs with stacking direction $[\nu_1\nu_2\nu_3]$.

Let us now consider a heterostructure consisting of layers of weak TIs as illustrated in Fig. 5.16(a). Without loss of generality, we consider the invariants of the weak TIs to be $0;(100)$, i.e., the weak TIs are equivalent to 2D TIs stacked in the x direction, which thus corresponds to the "dark direction". Next, we create a one-dimensional superlattice in the z direction, which is perpendicular to the dark direction, by inserting spacers of OIs between the weak TI layers. Due to the bulk-boundary correspondence, there will be an even number of Dirac cones at each interface between the OI and the weak TI. For simplicity, we here assume each interface to have the minimal number of two Dirac cones. Initially, the Dirac cones are pinned to *different* TRI momenta Γ_α and Γ_β along the dark direction. However, a dimerization in the weak TI crystal [196] breaks the translational symmetry along the dark direction x and allows the two Dirac cones to couple. Furthermore, if weak TI layers and spacer layers are sufficiently thin, also Dirac states from adjacent surfaces can couple through hybridization.

Low-energy theory formulation

The low-energy theory of the multilayer heterostructure described above is given by the following Hamiltonian,

$$\begin{aligned}\mathcal{H} \;=\; \sum_{\mathbf{k}_\perp, ij} \Big[& v_D \sigma_3 \tau_0 (\hat{z}\times\mathbf{s})\cdot\mathbf{k}_\perp\,\delta_{i,j} + m\sigma_0\tau_2 s_3\,\delta_{i,j} + t_{\mathrm{a},1}\sigma_1\tau_0 s_0\,\delta_{i,j} \\ & + \frac{t_{\mathrm{a},2}}{2}(\sigma^-\,\delta_{i,j+1} + \sigma^+\,\delta_{i,j-1})\tau_0 s_0 + t_{\mathrm{b},1}\sigma_1\tau_1 s_0\,\delta_{i,j} + \delta_1\sigma_2\tau_2 s_0\,\delta_{i,j} \\ & + \frac{t_{\mathrm{b},2}}{2}(\sigma^-\,\delta_{i,j+1} + \sigma^+\,\delta_{i,j-1})\tau_1 s_0 \Big]\, c^\dagger_{\mathbf{k}_\perp, j} c_{\mathbf{k}_\perp, i},\end{aligned} \tag{5.19}$$

where σ_ν, τ_ν, and s_ν are Pauli matrices associated with the top and bottom surfaces of the weak TIs, the two Dirac cones per surface, and the spin degree of freedom, respectively. In addition, v_D is the Fermi velocity of the Dirac fermions, $\mathbf{k}_\perp = (k_x, k_y)$ is their momentum in the 2D surface BZ of the weak TIs, m is the "dimerization mass", and the indices i, j label the weak TI layers. The parameters of our model are illustrated in Fig. 5.16(b). Note that we also allow for an inter-valley coupling imbalance δ_1. Such an imbalance is expected to arise naturally when top and bottom surfaces of the weak TI layers are nonidentical, e.g., when one surface is canted relative to the other. For simplicity, other imbalances have been omitted since they do not change the results qualitatively.

The model of Eq. (5.19) preserves time-reversal symmetry with the operator $\Theta = i\sigma^0\tau^0 s^2 K$, $\mathbf{k}\to-\mathbf{k}$, where K is complex conjugation. The inter-valley coupling imbalance serves as an inversion-symmetry breaking term. The corresponding inversion operator is $P = \sigma^1\tau^0 s^0$, with $\mathbf{k}\to-\mathbf{k}$. In order to pin down the existence of a WSM phase, the energies of the system are computed and its half-filling gap is monitored through the parameter space. This allows to identify gap closing points and their degeneracies. We can anticipate the existence of a WSM phase qualitatively using the following arguments: the hybridization of the surface Dirac cones $\propto t_{a,1}, t_{a,2}$ leads to two 3D Dirac points in the 3D BZ of the model. The dimerization $\propto m$ can either gap out these degeneracy points, leading to fully gapped phases, or shift the two 3D Dirac points in momentum space. Such an unstable Dirac semimetal phase can in principle be transformed into a stable WSM phase by breaking inversion symmetry [159–161]. This is accomplished by the inter-valley coupling imbalance: each 3D Dirac point is split into two separate Weyl points.

Let us first explore the half-filling phase diagram for the inversion-symmetric model with $\delta_1 = 0$ [see Fig. 5.17(a)]. We find several gapped phases, which we dub A and B, separated by phase boundaries along which the system is semimetallic. More specifically,

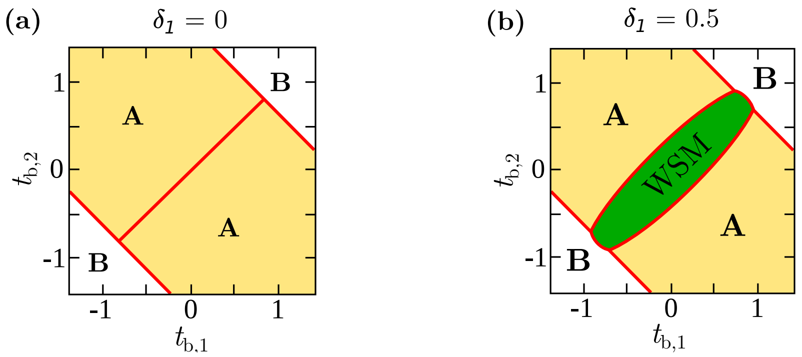

Figure 5.17: Phase diagrams of the weak TI multilayer with $v_D = m = t_{\mathrm{a},1} = t_{\mathrm{a},2} = 1$. (a) With inversion symmetry ($\delta_1 = 0$): there are two different gapped phases, phase A (strong TI) and phase B (OI), and an unstable Dirac semimetal phase (red lines). (b) Broken inversion symmetry ($\delta_1 = 0.5$): between the strong TI phases, a stable WSM phase (green) with four isolated Weyl points emerges.

in the semimetallic phase the system exhibits two unpinned 3D Dirac points on the k_z axis related by time-reversal symmetry.

By exploring the parameter space of the model, it can be found that the B phases are adiabatically connected to a multilayer of fully-decoupled dimerized weak TIs. Since a dimerized weak TI is topologically trivial, these phases correspond to an ordinary insulator with $\mathbb{Z}_2$ invariants $0;(000)$. In order to determine the nature of the other gapped phases, the corresponding parity eigenvalues of all occupied states are calculated at the TRI momenta $\Gamma = (0,0,0)$ and $Z = (0,0,\pi)$ [40], assuming that the topologically active band inversions occur only at these momenta. As a result, a band inversion at the Γ point occurs by moving from a B phase to an A phase. On the contrary, no band inversion occurs between the two A phases. Hence, under our assumption, we deduce that the A phases correspond to strong TIs with $\mathbb{Z}_2$ invariants $1;(000)$. Below, we will confirm these results by analyzing a lattice regularization of the model.

Let us now turn to the inversion-broken case ($\delta_1 \neq 0$). With inversion symmetry, the two strong TI phases are separated by a Dirac-semimetal line. By breaking inversion symmetry, the Dirac points are split into four separate Weyl points along the k_z axis. In this way, a WSM stability region emerges in the phase diagram [Fig. 5.17(b)]. By integrating the Berry curvature over a closed momentum-space surface around each of the Weyl nodes, their topological charges are calculated to be ± 1.

In order to synthesize the proposed weak TI multilayer, one could start out with a dimerized weak TI material, namely $\mathrm{Bi}_{13}\mathrm{Pt}_3\mathrm{I}_7$ [98]. Into the dark surface of the material one could then carve an array of sufficiently thin channels, where the channels are alternatingly tilted against each other. In this way, opposite weak TI surfaces are nonidentical thereby providing the required interlayer coupling imbalance. This setup is extremely challenging but can be accomplished using terraces or creating trenches by, e.g., focused ion beams. The coupling between the layers can be fine-tuned by varying the channel spacing, the channel width, and their relative angle. Finally, the channels must be filled with an insulating spacer material. The resulting sample can be viewed as a dimerized weak TI with a WSM layer on top of it. The characteristic features of the WSM, such as surface Fermi arcs, could then be detected by performing angle-resolved photoemission experiments.

Tight-binding model formulation

Let us now construct a tight-binding model whose low-energy theory is represented by the Hamiltonian introduced in Eq. (5.19) above. For simplicity, we regularize the continuum model on a cubic lattice.

We start by taking the momentum-space Hamiltonian corresponding to Eq. (5.19), and perform the replacements $k_{x,y} \to \sin k_{x,y}$. This yields a Weyl semimetal with 16 Weyl points. In order to get a model with the minimal number of Weyl points allowed by symmetry, which is four for a time-reversal invariant system, we can annihilate all Weyl points away from the k_z axis. This is accomplished by replacing m with $m + b(2 - \cos k_x - \cos k_y)$, where the additional tight-binding parameter b has been introduced. The Bloch Hamiltonian of the ensuing model reads

$$\begin{aligned} H(\mathbf{k}) \;=\; & v_D\, \sigma^3 \tau^0 (\sin k_y s^1 - \sin k_x s^2) + \big[m + b(2 - \cos k_x - \cos k_y)\big]\, \sigma^0 \tau^2 s^3 \\ & + t_{\mathrm{a},1}\, \sigma^1 \tau^0 s^0 + t_{\mathrm{a},2} (\cos k_z\, \sigma^1 - \sin k_z\, \sigma^2)\, \tau^0 s^0 + t_{\mathrm{b},1}\, \sigma^1 \tau^1 s^0 + \delta_1\, \sigma^2 \tau^2 s^0 \\ & + t_{\mathrm{b},2}\, (\cos k_z\, \sigma^1 - \sin k_z\, \sigma^2)\, \tau^1 s^0 + \alpha \sin k_z\, \sigma^3 \tau^0 (s^1 + s^2), \end{aligned} \tag{5.20}$$

In agreement with the low-energy model, this Hamiltonian preserves time-reversal symmetry and has inversion symmetry for $\delta_1 = 0$. In addition, the Bloch Hamiltonian for $\alpha = 0$ is invariant under a π rotation around the z axis, with the rotation operator given by $R_z(\pi) = i\sigma^0 \tau^0 s^z$, and $(k_x, k_y, k_z) \to (-k_x, -k_y, k_z)$. To break this symmetry explicitly, a rotational-symmetry breaking term has been introduced parameterized by α.

Around $k_x = k_y = 0$ and for $\alpha = 0$, the Hamiltonian in Eq. (5.20) is identical to the low-energy model. As a consequence, both models have qualitatively the same phase diagrams

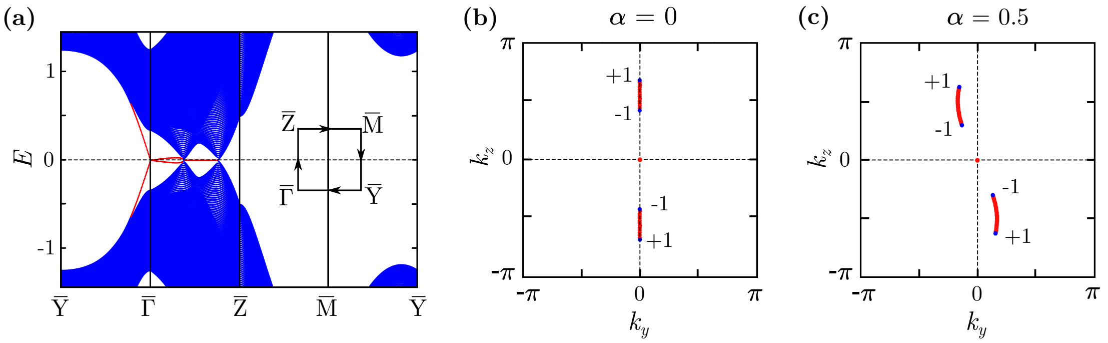

Figure 5.18: Band structure and $E_F = 0$ surface Fermi surfaces for the WTI multilayer tight-binding model in a slab geometry with $v_D = m = b = t_{\mathrm{a},1} = t_{\mathrm{a},2} = 1$, $t_{\mathrm{b},1} = t_{\mathrm{b},2} = 0.7$, and $\delta_1 = 0.5$ (Weyl semimetal phase). States localized to the surfaces are highlighted in red. (a) Band structure along high-symmetry lines of the surface BZ. Note the surface Dirac cone around $\bar{\Gamma}$, and the surface Fermi arcs and bulk Weyl cone projections along $\bar{\Gamma}\bar{Z}$. (b) Surface Fermi surface for $\alpha = 0$ (with rotational symmetry). (c) Surface Fermi surface for $\alpha = 0.5$ (without rotational symmetry). The topological charges of the Weyl nodes are also indicated.

including Weyl semimetal and STI phases (see Fig. 5.17 above). In particular, for the gapped phases the $\mathbb{Z}_2$ invariants can now be calculated directly. For this, either inversion symmetry is restored to use the parities of the eigenstates at the six time-reversal invariant points in the BZ [40], or a Wannier-center formulation of the topological invariants [197] is used (see Appendix B). Both methods yield the same results and, as expected, the calculations confirm the invariants of the STI phases to be $1;(000)$.

Let us now investigate the surface features of our system in the Weyl semimetal phase. For that, we carry out an inverse Fourier transformation of the Hamiltonian in Eq. (5.20) with respect to k_x and study the resulting mixed position-momentum space Hamiltonian with open boundary conditions in the x direction. This setup corresponds to a slab geometry with two surfaces representing the dark surfaces of the underlying WTI layers. Energies and eigenstates are obtained by exact numerical diagonalization.

In the presence of rotational symmetry, the surface Fermi surface with respect to a Fermi energy at $E_F = 0$ contains four isolated bulk states along the k_z axis which correspond to the surface projections of the four bulk Weyl nodes [see Fig. 5.18(b)]. The isolated bulk states are connected pairwise by doubly degenerate Fermi arcs of states localized at the two surfaces, as expected for a Weyl semimetal. The vanishing curvature of the Fermi arcs is a consequence of rotational symmetry. Moreover, we find a pair of isolated, doubly degenerate surface states pinned to the $\bar{\Gamma}$ point of the surface BZ. These states belong to the vertex of a surface Dirac cone which happens to coincide with the Fermi level. Hence, this system is yet another realization of a time-reversal invariant Weyl semimetal with coexisting Fermi arcs and Dirac cones at its surfaces [181, 198].

The dispersion of the energy states along high-symmetry lines of the surface BZ is illustrated in Fig. 5.18(a). The projections of the bulk Weyl cones are clearly visible along the k_z direction as well as the connecting Fermi arcs. In the k_y direction we see the linear dispersion of the surface Dirac cone. Its dispersion along the k_z axis is extremely flat and terminates at one of the Weyl nodes. When rotational symmetry is broken ($\alpha \neq 0$), the Weyl node projections move away from the k_z axis and the surface Fermi arcs are no longer straight lines, as can be seen in Fig. 5.18(c).

5.3.3 Topological crystalline insulator multilayer

The essential ingredient used in the setup introduced in Sec. 5.3.2 is the presence of two Dirac cones per surface that are coupled to each other. The question that arises is whether this idea is also applicable to systems in which surface Dirac cones are not pinned to TRI momenta. This occurs, for instance, in the topological crystalline insulators in the SnTe material class which we have introduced in Sec. 4.1.3. They allow for an even number of *unpinned* surface Dirac cones protected by mirror symmetry [112].

Let us briefly recall the main features of TCIs. TCIs are similar to “conventional” TIs except that topological states are protected by additional discrete symmetries, such as mirror, inversion or space group symmetries [48, 110, 113, 115, 120, 128]. For systems in the SnTe material class, we can define mirror Chern numbers n_M for each mirror-invariant plane, which represent $\mathbb{Z}$ topological invariants. By bulk-boundary correspondence, a nonzero mirror Chern number implies the presence of $|n_M|$ Dirac cones on surfaces which preserve the protecting mirror symmetry M [112].

In following, we are going to show that also TCI multilayers give rise to WSM phases. In analogy with weak TI heterostructures, let us consider a multilayer consisting of alternating layers of TCIs and OIs [see Fig. 5.19(a)]. Moreover, we will use a minimal TRI TCI with mirror Chern number $n_M = 2$ protected by a yz mirror plane. Thus, on surfaces parallel to the xy plane there will be two *unpinned* Dirac cones at momenta related by time-reversal symmetry. Without loss of generality, let them be at $\mathbf{k}_\perp = \pm\mathbf{d} = (0, \pm d)$. As opposed to a dimerized weak TI multilayer, the Dirac cones can be gapped even in the absence of intravalley scattering by breaking mirror-symmetry with respect to the yz mirror plane. This can be accomplished, for instance, by a ferroelectric distortion [112, 199]. Moreover,

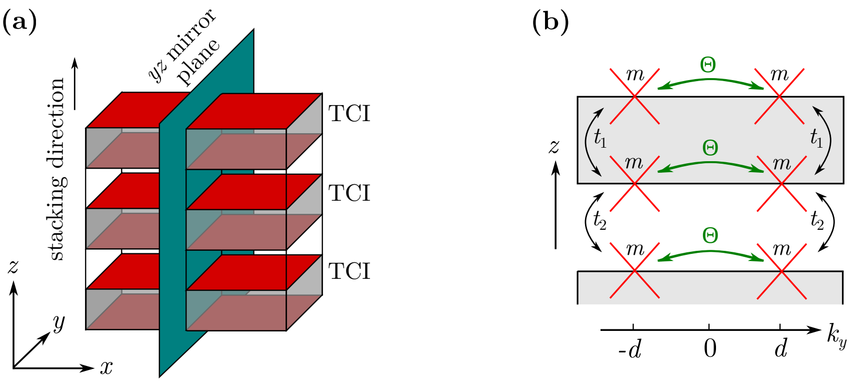

Figure 5.19: TCI multilayer: (a) cartoon of the multilayer design. The surfaces of the TCI layers (red) contribute two unpinned surface Dirac cones each, which are protected by a yz mirror plane. (b) Schematic of the coupling terms between the surface Dirac cones (red). The Dirac cones are connected by time reversal Θ and can be gapped by a mirror-symmetry breaking mass m.

let the stacking direction of the TCI layers coincide with the z axis.

Low-energy theory formulation

As in the previous section, let us start with a low-energy description of our heterostructure. Taking into account a ferroelectric Dirac mass parameterized by m, which breaks the mirror symmetry of the system, the low-energy theory of the TCI multilayer can be written down in analogy with the weak TI heterostructure. The model parameters are illustrated in Fig. 5.19(b). The corresponding Hamiltonian is

$$\begin{aligned}\mathcal{H} &= \sum_{\mathbf{k}_\perp,ij}\Big[\frac{v_D}{2}\sigma^3(\tau^0+\tau^3)(\hat{z}\times\mathbf{s})\cdot(\mathbf{k}_\perp+\mathbf{d})\,\delta_{i,j}+\frac{v_D}{2}\sigma^3(\tau^0-\tau^3)(\hat{z}\times\mathbf{s})\cdot(\mathbf{k}_\perp-\mathbf{d})\,\delta_{i,j}\\ &\quad+t_1\sigma^1\tau^0s^0\,\delta_{i,j}+\frac{t_2}{2}(\sigma^-\,\delta_{i,j+1}+\sigma^+\,\delta_{i,j-1})\tau^0s^0+m\,\sigma^0\tau^3s^3\,\delta_{i,j}\Big]\,c^\dagger_{\mathbf{k}_\perp,j}c_{\mathbf{k}_\perp,i}. \qquad (5.21)\end{aligned}$$

The reflection operator is $M_x = i\sigma^0\tau^0s^1$ with $k_x \to -k_x$. Time-reversal symmetry is preserved for all parameters with $\Theta = i\sigma^0\tau^1s^2K$, and $\mathbf{k}\to-\mathbf{k}$. The operator of spatial inversion is represented by $P = \sigma^1\tau^1s^0$ (with $\mathbf{k}\to-\mathbf{k}$) and does not commute with the ferroelectric Dirac mass. Hence, the ferroelectric distortion also breaks inversion symmetry, which will enable us to create a stable WSM phase similar to the weak TI multilayer.

In Figs. 5.20(a) and (b), the t_1-t_2 phase diagrams of the heterostructure are shown. For $m = 0$, the system preserves inversion symmetry. In this case, we find gapped phases for $t_1 \lessgtr t_2$, as well as a gapless phase along the line $t_1 = t_2$, as is shown in Fig. 5.20(a). In

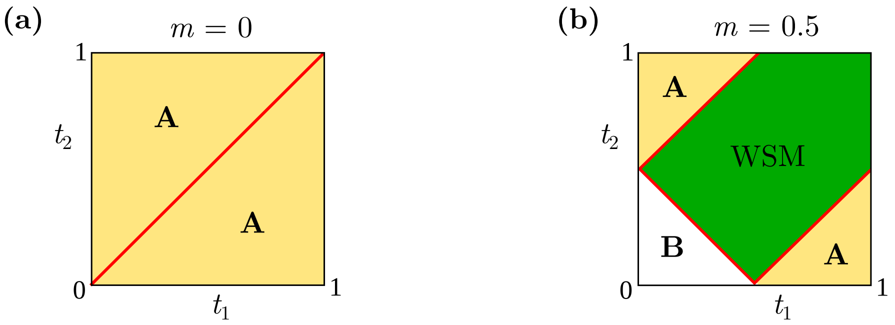

Figure 5.20: Phase diagrams of the TCI multilayer with $v_D = 1$ and $\mathbf{d} = (0, 1)$. (a) With inversion symmetry ($m = 0$): there are two gapped phases A (weak TI) and an unstable Dirac semimetal phase (red line). (b) Broken inversion symmetry ($m = 0.5$): a new gapped phase B (OI) emerges. Between the gapped phases, there is a stable WSM phase (green) with four isolated Weyl points.

the latter, the system has two isolated bulk Dirac points at $\mathbf{k} = (0, \pm d, \pi)$.

For nonzero m, a WSM phase with four isolated Weyl points emerges in the phase diagram [see Fig. 5.20(b)]. The Weyl nodes have topological charges of ±1. Furthermore, a new gapped phase appears around $(t_1, t_2) = (0, 0)$.

Let us briefly comment on the gapped phases in Figs. 5.20(a) and (b). For $m \neq 0$, the point $(0, 0)$ in the phase diagram represents a multilayer of decoupled, mirror-symmetry broken TCIs with gapped Dirac cones. This is a topologically trivial system. Hence, the B phase corresponds to a phase of OIs with $\mathbb{Z}_2$ invariants $0; (000)$. To determine the nature of the A phases, let us assume our model describes the low-energy theory of a lattice model. Then, an analysis of the change of parities, by going from one A phase to the other in the inversion-symmetric case ($m = 0$), shows that both A phases are identical. For the inversion-symmetry broken case, let us consider the transition from A phase to B phase along the t_1 or along the t_2 axis. The bulk energy gap of the system closes along lines in momentum space at $(k_x, k_y) = (0, \pm d)$. Such a gap closing transition can only change the weak $\mathbb{Z}_2$ invariant ν_3 relative to the B phase while the others remain unchanged. Hence, the A phases correspond to weak TIs with $\mathbb{Z}_2$ invariants $0; (001)$, i.e., their dark direction coincides with the stacking direction of the multilayer. We will verify this conclusion below by comparing these results to a lattice regularization of the model.

As opposed to the weak TI multilayer, the heterostructure based on TCI layers could be prepared in the form of a superlattice. The coupling between the surface Dirac cones can be adjusted by choosing a particular thickness for the layers of TCIs and OIs. To break mirror symmetry on the surfaces of the TCI layers, one could use an insulating, ferro-electric material for the layers in between the TCIs.

A concrete material candidate is a heterostructure of alternating layers of PbTe and SnTe stacked in the [110] direction [112]. SnTe is a TCI and hosts two Dirac cones on (110) surfaces protected by a $(1\bar{1}0)$ mirror plane, whereas PbTe is an OI. Moreover, SnTe undergoes a ferroelectric distortion at low temperatures [112]. The distortion is along the [111] direction. This breaks the $(1\bar{1}0)$ mirror plane thereby providing an intrinsic mechanism to gap out the surface Dirac cones. Hence, this superlattice is expected to realize a WSM phase.

Tight-binding model formulation

Following the same procedure as before, we now construct a tight-binding model based on the TCI multilayer Hamiltonian of Eq. (5.21) above. To achieve this, we first perform the following substitutions: $k_x \to \sin k_x$, $k_y \pm d \to \sin(k_y \pm d)$. As before, this leads to a multitude of Weyl points. Another substitution, namely

$$\begin{aligned} m\,\sigma^0\tau^3 s^3 \quad &\to \quad [m + b(2-\cos k_x)]\sigma^0\tau^3 s^3 - \frac{b}{2}\cos(k_y+d)\,\sigma^0(\tau^3+\tau^0)s^3 \\ &\qquad - \frac{b}{2}\cos(k_y-d)\,\sigma^0(\tau^3-\tau^0)s^3 \end{aligned} \tag{5.22}$$

finally yields a tight-binding model with only four Weyl nodes, whose low energy theory is thus identical to the Hamiltonian of Eq. (5.21). The Bloch Hamiltonian reads

$$\begin{aligned} H(\mathbf{k}) \quad = \quad & \frac{v_D}{2}\,\sigma^3(\tau^0+\tau^3)[\sin(k_y+d)s^1 - \sin k_x s^2] \\ & + \frac{v_D}{2}\,\sigma^3(\tau^0-\tau^3)[\sin(k_y-d)s^1 - \sin k_x s^2] \\ & + \frac{1}{2}\big(m + b[2-\cos k_x - \cos(k_y+d)]\big)\,\sigma^0(\tau^3+\tau^0)s^3 \\ & + \frac{1}{2}\big(m + b[2-\cos k_x - \cos(k_y-d)]\big)\,\sigma^0(\tau^3-\tau^0)s^3 \\ & + t_1\,\sigma^1\tau^0 s^0 + t_2(\cos k_z\,\sigma^1 - \sin k_z\,\sigma^2)\,\tau^0 s^0 \\ & + \alpha \sin k_z\,\sigma^3\tau^0(s^1+s^2). \end{aligned} \tag{5.23}$$

Similar to the tight-binding model for the WTI multilayer, this model is invariant under a π rotation about the z axis (for $\alpha = 0$). For this reason, an additional rotational-symmetry breaking term parameterized by α has been incorporated.

First of all, the phase diagram of the tight-binding model is computed by keeping track of all the gap-closing and reopening transitions. Those happen approximately at the same

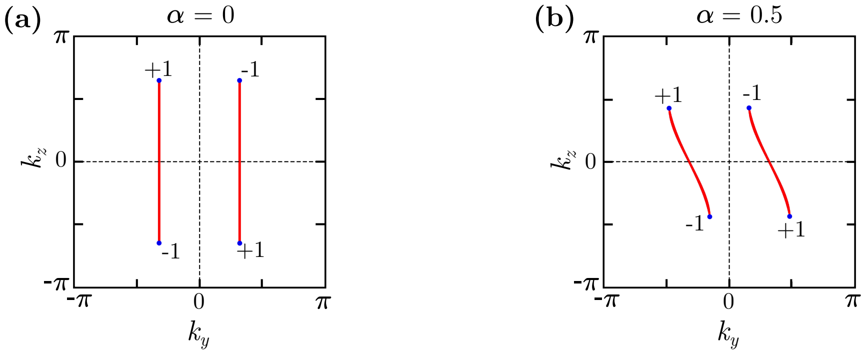

Figure 5.21: $E_F = 0$ surface Fermi surfaces for the TCI multilayer tight-binding model with $v_D = b = 1$, $t_1 = t_2 = m = 0.5$ and $d = 1$ (Weyl semimetal phase). The surface projections of the bulk Weyl nodes are highlighted in blue: (a) with rotational symmetry ($\alpha = 0$). (b) broken rotational symmetry ($\alpha = 0.5$). The topological charges of the Weyl nodes are also indicated.

points and for the same parameter values as for the low-energy model. In particular, there are gapless Weyl semimetal phases and also insulating phases (see Fig. 5.20 above). For the insulating phases, the four $\mathbb{Z}_2$ invariants are again calculated explicitly. They are in agreement with the values determined before solely based on adiabaticity arguments, i.e., the invariants of the WTI phases are 0; (001) whereas those of the trivial phase are 0; (000). Furthermore, the Weyl semimetal phase has four Weyl nodes of charge ±1.

To investigate the structure of the Fermi arcs in the Weyl semimetal phase, the (100) surface Green's function of the tight-binding model in Eq. (5.23) is determined for a semi-infinite slab [200] (see Appendix C). This allows to calculate the spectral function $A(\mathbf{k}, E) = -1/2\pi \, \mathrm{Im}\{\mathrm{Tr}[G_s(\mathbf{k}, E)]\}$ at the Fermi level $E = E_F$. Since our Hamiltonian is bilinear, the spectral function is sharply peaked whenever there is an eigenstate of the Hamiltonian at the Fermi level. Hence, the spectral function can be used to determine the surface Fermi surface of the semi-infinite slab.

The results are shown in Fig. 5.21. In the rotation-symmetric case [Fig. 5.21(a)], two straight lines of surface states connect the surface projections of the Weyl nodes. By breaking rotation symmetry, as shown in Fig. 5.21(b), the Weyl nodes are displaced and the Fermi arcs acquire a finite curvature.

6 Outlook and conclusions

In this dissertation, the interplay of topology and symmetry in weakly-interacting materials has been explored on a theoretical level. In particular, it has been shown how additional symmetries can enrich the topology of insulating and semi-metallic systems considerably.

In Chapter 2, the celebrated Hofstadter model, a lattice realization of the quantum Hall effect, has been considered in the presence of a lattice *dimerization*. It has been shown that depending on the sign of the dimerization mass, this model exhibits topological edge states at half filling. Remarkably, the edge states arise from topologically nontrivial, inversion-symmetric slices of the two-dimensional Hofstadter Brillouin zone. Most importantly, these novel topological states are different from the well-known quantum-Hall edge states because their Hall conductivity is zero and they are, thus, solely subject to inversion symmetry in the one-dimensional subsystems. To uncover the topological nature of the edge states, an integer topological invariant for the inversion-symmetric cuts has been defined and calculated. From a more general perspective, a two-dimensional insulating system has been presented where lower-dimensional physics enriches the global topological structure of the system.

Chapter 3 has dealt with surface states of time-reversal symmetric topological insulators. In particular, the presented results show how effectively one-dimensional Dirac electrons appear on the surface of weak topological insulators in the presence of *in-plane* time-reversal invariance. The corresponding *Dirac lines* are topologically protected by this symmetry and connect time-reversal invariant momenta in the surface Brillouin zone of the material. The surface states are, thus, qualitatively different from those in conventional weak topological insulators which exhibit pairs of surface *Dirac points*. Furthermore, it has been shown that these line features cannot appear on the surface of strong topological insulators and are, therefore, an exclusive feature of weak topological insulators. This example demonstrates how an additional symmetry enriches the structure of surface states in a topological insulator.

Going one step further, Chapter 4 has inspected how the celebrated family of time-reversal symmetric topological insulators in two and three dimensions can be extended to one dimension by imposing an additional symmetry. More specifically, it has been shown that one-dimensional spin-1/2 fermionic systems with *both* time-reversal and mirror symmetry give rise to nontrivial topology. In these systems, the partial polarization can only assume two distinct values and, therefore, defines a topological $\mathbb{Z}_2$ invariant. If this number is nonzero, the system is a topological mirror insulator whose hallmark is an odd number of topologically protected electronic end charges. These findings have been checked against a class of models that realize topologically nontrivial $\mathbb{Z}_2$ phases and can potentially be realized in ultracold Fermi gases loaded in periodic optical lattices, as well as in semiconductor nanowires with perpendicular modulated voltage gates. The results of this analysis show how systems previously considered to be trivial may be turned into topological phases by imposing additional symmetries.

Chapter 5 has ventured into the realm of topological semimetals, particularly Weyl semimetals with time-reversal symmetry. In the first part of the chapter, a generic coexistence of Dirac cones and Fermi arcs on the surface of time-reversal invariant Weyl semimetals has been revealed. It has been argued that the coexistence is due to the existence of six $\mathbb{Z}_2$ invariants that additionally characterize such a semimetallic system: the invariants impose restrictions on the number of surface Kramers pairs along time-reversal invariant lines in the surface BZ and, therefore, also on the structure of the Fermi arcs. Nevertheless, a remaining modulo-two ambiguity gives rise to many possible and qualitatively different Fermi-arc connectivities. It has been shown that certain connectivities require the creation of a Dirac Fermi pocket which is connected to the presence of a surface Dirac cone pinned to a time-reversal invariant momentum. Consequently, a change of the connectivity changes the topology of the Fermi surface and is, thus, accompanied by a Lifshitz transition. It is crucial to note that this transition does not change the $\mathbb{Z}_2$ invariants of the material and is, therefore, generic to *all* Weyl semimetals with time-reversal symmetry. Moreover, by means of density-functional theory calculations, the half-Heusler compound LaPtBi under compressive strain has been proposed as a candidate material to realize the coexistence of Fermi arcs and Dirac cones. Generally speaking, it has been demonstrated how time-reversal symmetry enriches the structure of surface states in a topological semimetal.

Finally, the second part of Chapter 5 has looked into multilayer heterostructures, based either on weak topological insulators or on topological crystalline insulators, as a novel platform for the study of time-reversal invariant Weyl semimetals. In the proposed designs, thin layers of the materials are stacked on top of each other while inserting spacer layers of ordinary insulators in between. At the interfaces, pairs of pinned or unpinned

Dirac cones, which are coupled to each other, provide the main ingredient of the multilayer designs. Weyl phases are then stabilized by breaking inversion symmetry. Moreover, the corresponding phase diagrams also indicate the possibility of strong topological insulator phases in the weak topological insulator multilayer, and of weak topological insulator phases in the topological crystalline insulator heterostructure. As a result, the multilayers may also provide a novel way of designing artificial three-dimensional topological insulators.

Building upon these results, there are several promising research directions to pursue from this point. First of all, the focus of this dissertation has been entirely on insulating and semimetalic materials. Nevertheless, as already indicated in the main body of the thesis, also superconductors can be classified using the language of topology [201, 202]. In particular, topological superconductors give rise to exotic quasiparticle excitations which are realizations of Majorana particles in a condensed matter setup. Most remarkably, Majorana modes obey anyonic non-Abelian statistics which makes them potential building blocks for topological quantum computers [203]. In the light of this thesis, the effect of symmetries on the properties of topological superconductors and on their exotic quasiparticles would be an interesting route to follow.

From the material perspective, topological superconductivity can be induced at the interface between a topological material and a normal superconductor using the proximity effect [204–206]. This gives rise to a plethora of possible platforms for topological superconductivity which could be explored in future research. Also in this context, symmetry plays an essential role and potentially leads to novel unexplored features. More specifically, interfaces between various topological systems with symmetries, such as the topological crystalline insulators or Weyl semimetals discussed in this thesis, and superconductors with different pairing symmetry could be studied. Other systems of interest are Majorana nanowires [207] or systems featuring topological bulk superconductivity [208–210].

Another promising research direction is the study of interaction-enabled topological phases with symmetries. This dissertation has dealt with weakly-interacting systems only, i.e., systems that can effectively be mapped to a non-interacting picture. Nonetheless, the on-set of interactions can reduce [211] or even enrich the topological content of a system [212–214]. This can lead to novel phases, such as fractional quantum-Hall systems, topological Kondo insulators or topological Mott insulators. Building on the results of the non-interacting case, it could be studied how electron-electron interactions affect the topological features of the systems considered in this thesis.

A Smooth gauge for one-dimensional systems

The $\mathbb{Z}_2$ topological invariant defined in Eq. (4.18) of Chapter 4 requires a continuous gauge. In the following, a method to construct such a gauge from numerically obtained eigenstates of a 1D system is going to be presented. The discussion closely follows the appendix of Ref. [215].

Let us consider an isolated set of N bands, i.e., the bands can cross each other but shall have no crossings with other bands outside the considered set. Furthermore, consider a discrete uniform k mesh of $M+1$ points $\{k_j\}$, $j \in [1, M+1]$, where $k_{j+1} = k_j + \Delta$ and $k_{M+1} = k_1 + G$ with a reciprocal lattice vector G. We label the corresponding eigenstates along the mesh by $|\tilde{u}_{nk_j}\rangle$, where n is the band index. If these states are obtained from a numerical diagonalization routine, they will in general have random phases. It is easy to see that in the limit $M \to \infty$ such a choice of phases is highly non-differentiable.

In order to construct a smooth numerical gauge, we have to define what we mean by "smooth" for a discrete mesh. This can be done by requiring that the states remain as parallel as possible as we move along a path from k_1 to k_{N+1}. In other words, the change in the states should be orthogonal to the states themselves. The corresponding gauge is called *parallel transport gauge*. For a single isolated band this can be realized by choosing the phases of the Bloch states such that the overlap $\langle u_{nk_j}|u_{nk_{j+1}}\rangle$ is real and positive. For N bands, one has to require that the overlap matrix $L_{mn} = \langle u_{mk_j}|u_{nk_{j+1}}\rangle$ is hermitian with only positive eigenvalues.

We are now going to discuss how a parallel-transport gauge can be constructed in practice. We start from the initial point $j = 1$ where we set $|u'_{nk_1}\rangle = |\tilde{u}_{nk_1}\rangle$. Then, at each subsequent k_{j+1} we have to rotate the states $|\tilde{u}_{nk_{j+1}}\rangle$ by a unitary matrix U in such a way that the overlap matrix $\tilde{L}$ becomes hermitian and positive. This is accomplished by employing a singular value decomposition. More specifically, $\tilde{L}$ can be written as $\tilde{L} = V\Sigma W^\dagger$, where V and W are unitary and Σ is positive real diagonal. If we now set

$U = WV^\dagger$ and transform the states as

$$|u'_{nk_{j+1}}\rangle = \sum_m^N U_{mn}(k_{j+1})|\tilde{u}_{mk_{j+1}}\rangle, \tag{A.1}$$

the new overlap matrix becomes $L' = V\Sigma V^\dagger$, which is hermitian and positive. Repeating this for the entire k mesh, we finally get a set of states $|u'_{nk_j}\rangle$ that are smooth in the sense specified above. However, states at k_1 and k_{N+1} will in general differ by a unitary transformation Λ and are, thus, not mapped onto themselves via parallel transport. The matrix Λ corresponds to a non-Abelian analogue of the Berry phase and has eigenvalues of the form $\lambda_l = e^{i\phi_l}$.

The periodicity can be restored in the following way: we first determine the unitary matrix S that diagonalizes Λ. We then rotate all states, for all k_j, by S. This results in a gauge in which the new states correspond to a diagonal Λ with eigenvalues $e^{i\phi_l}$. At last, we spread the residual phase differences over the k mesh,

$$|u_{lk_j}\rangle = e^{i(j-1)\phi_l/M}|u'_{lk_j}\rangle. \tag{A.2}$$

Eventually, we have constructed a smooth, periodic gauge for the set of N bands. Note, however, that the new states $|u_{lk_j}\rangle$ are in general not eigenstates of the Hamiltonian. Nevertheless, at each k_j they span the eigenspace corresponding to the N bands. They can therefore be used for the calculation of $U(N)$-invariant quantities like the partial polarization.

B Wannier-center formulation of the topological invariant

This section reviews a method [197] that enables one to calculate the $\mathbb{Z}_2$ topological invariant of a general 2D insulator with time-reversal symmetry. This method allows to calculate the $\mathbb{Z}_2$ number without choosing a gauge-fixing condition, which makes it particularly appealing for numerical studies.

The central notion of this method is the *time-reversal polarization* [75]. In a time-reversal invariant 1D band insulator, the $2N$ occupied bands can be decomposed into two sets which are connected by time reversal. The time-reversal polarization is then the difference in the net charge polarization of the two sets of bands. Furthermore, it can be shown that the time-reversal polarization can only assume the values 0 or 1 (modulo 2) as long as the system preserves time-reversal symmetry.

A 2D TRI band insulator can be thought of as a collection of 1D insulators in momentum space parametrized by, say, k_y. In this collection, only the effective 1D systems at $k_y = 0$ and π preserve 1D time-reversal symmetry. Thus, the time-reversal polarization can assume non-integer values in between. The key idea is now to determine how the time-reversal polarization changes with k_y. It was shown that this leads to a well-defined $\mathbb{Z}_2$ invariant for a 2D band insulator [75, 197]. Moreover, the charge polarization of an occupied band is related to its Wannier center in position space. For this reason, the change in time-reversal polarization can also be understood as a shift of the Wannier centers.

The Wannier centers of the occupied bands at fixed k_y are defined as the eigenvalues of the position operator projected onto the occupied subspace. By using localized Wannier functions $|\alpha j\rangle$ as a basis, where α is an orbital index and j denotes the lattice site, the position operator for a 1D lattice system with periodic boundary conditions can be written as

$$\hat{X} = \sum_{\alpha j} e^{-i\frac{2\pi j}{N_x}} \, |\alpha j\rangle\langle\alpha j|, \tag{B.1}$$

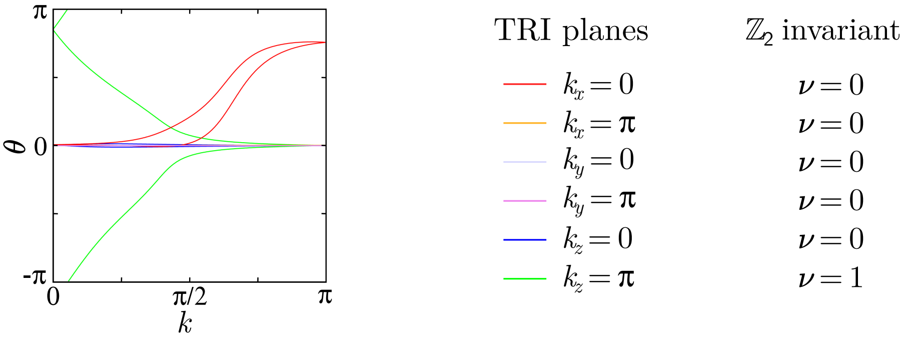

Figure B.1: Evolution of the Wannier centers θ_m as a function of k for the TRI planes of the tight-binding model with $a = b = 1$, $t = 1.5$, $\alpha = 0.3$, $d = 0.1$, $\lambda = 0.5$ and $\beta = 0.7$. k denotes a momentum parallel to the considered plane in the 3D BZ. The corresponding value of the $\mathbb{Z}_2$ invariant ν, as inferred from the winding number of the Wannier pair, is also indicated.

where N_x is the number of unit cells. Furthermore, the projection operator onto the occupied bands o at fixed k_y is defined as

$$\hat{P}(k_y) = \sum_{n \in o, k_x} |\Psi_{nk_xk_y}\rangle\langle\Psi_{nk_xk_y}|, \tag{B.2}$$

with the Bloch state $|\Psi_{n\mathbf{k}}\rangle = e^{i\mathbf{k}\cdot\mathbf{r}}|n\mathbf{k}\rangle$. The projected position operator can be written as follows

$$\hat{X}_P(k_y) = \hat{P}(k_y)\hat{X}\hat{P}(k_y) = \sum_{j=1}^{N_x}\sum_{mn\in o} |\Psi_{n,k_{x,j},k_y}\rangle\langle\Psi_{n,k_{x,j+1},k_y}|F^{nm}_{j,j+1}(k_y), \tag{B.3}$$

with $k_{x,j} = 2\pi j/N_x$ being the discrete k_x points taken along the x axis. The $F_{j,j+1}(k_y)$ are $2N \times 2N$ matrices with matrix elements

$$F^{nm}_{j,j+1}(k_y) = \langle n, k_{x,j}, k_y|m, k_{x,j+1}, k_y\rangle. \tag{B.4}$$

The eigenvalues of $\hat{X}_P(k_y)$ can be obtained by the transfer matrix method. For this purpose, we define the $2N \times 2N$ matrix

$$T(k_y) = F_{1,2}F_{2,3}\cdots F_{N_x-1,N_x}F_{N_x,1}. \tag{B.5}$$

T is unitary and has the following eigenvalues

$$\lambda_m(k_y) = e^{i\theta_m(k_y)}, \quad m = 1, 2, \ldots, 2N, \tag{B.6}$$

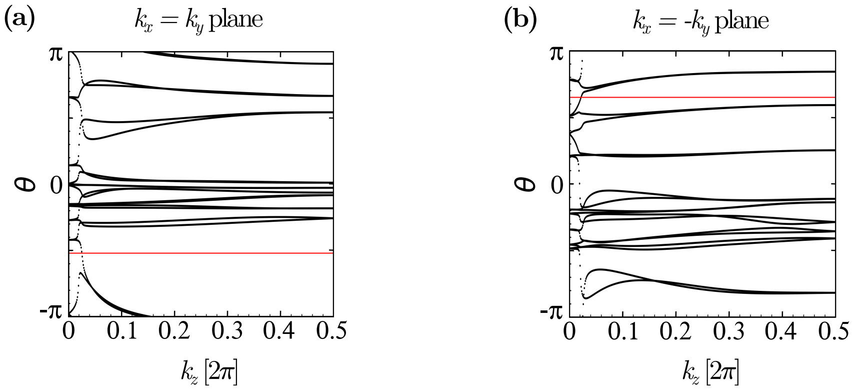

Figure B.2: Evolution of the Wannier centers θ as a function of k_z for the time-reversal invariant planes (a) $k_x = k_y$, and (b) $k_x = -k_y$ of LaPtBi. The path along k_z ranges from Γ ($k_z = 0$) to Z ($k_z = \pi$) of the bulk BZ. A reference line (red) is used to determine the $\mathbb{Z}_2$ topological invariant of the planes.

which are gauge invariant under $U(2N)$ transformations of the $|n\mathbf{k}\rangle$. Furthermore, it can be shown that in the continuum limit $T(k_y)$ corresponds to the $U(2N)$ Wilson loop [197],

$$T(k_y) = P\, e^{-i \int_{\mathcal{C}_{k_y}} A(k_x)\, dk_x}, \tag{B.7}$$

with the non-Abelian Berry connection $A(k)$ which is a unitary $2N \times 2N$ matrix. The eigenvalues of the projected position operator $\hat{X}_P(k_y)$, and thus the Wannier centers of the occupied bands, are then obtained from the eigenvalues of T as

$$\chi_{m,j}(k_y) = e^{i[\theta_m(k_y)+2\pi j]/N_x}, \quad j = 1, \ldots N_x. \tag{B.8}$$

Since the Wannier centers of adjacent unit cells differ only by a constant, k_y independent phase shift $e^{i2\pi/N_x}$, it is sufficient to look at the evolution of the $2N$ phases $\theta_m(k_y) = \operatorname{Im} \log \lambda_m(k_y)$.

The connection to the $\mathbb{Z}_2$ invariant is established as follows. We plot the $2N$ phases θ_m as a function of k_y and glue the lines $\theta = -\pi$ and $\theta = \pi$ together, such that the Wannier centers live on the surface of a cylinder. At $k_y = 0$, the phases have to appear as degenerate pairs due to time-reversal symmetry. By moving away from this point, the pairs split and recombine at $k_y = \pi$ (again due to time-reversal symmetry). Because the θ_m are phases, the Wannier-center pairs may now differ by an integer multiple of 2π. Hence, the evolution of the Wannier-center pairs from $k_y = 0$ to $k_y = \pi$ will encircle the cylinder an integer number of times. The sum of these integers over all pairs of Wannier centers defines a winding number. However, an even number of windings can always be removed, whereas this is not possible for a single winding. Consequently, the total winding number modulo 2 is a topological $\mathbb{Z}_2$ invariant. In practice, one draws an arbitrary reference line parallel to the k_y axis and counts how many times the Wannier centers cross this line. The system is topological (trivial), if the reference line is crossed an odd (even) number of times.

As an example, Fig. B.1 shows the evolution of the θ_m for the six TRI planes of the tight-binding model considered in Sec 5.2.3. There are only two occupied bands which is why we only need to look at a single pair of Wannier centers for each plane. We find that only the Wannier pair for the TRI plane at $k_z = \pi$ winds non-trivially around the θ-k cylinder. Hence, we infer that the $\mathbb{Z}_2$ invariant of this plane is $\nu = 1$. All other TRI planes have a trivial $\mathbb{Z}_2$ number, i.e., $\nu = 0$.

Furthermore, this scheme was also used to determine the $\mathbb{Z}_2$ invariants of the $k_x = \pm k_y$ planes in the density-functional theory study of LaPtBi in Sec 5.2.4. The evolution of the Wannier centers is shown in Fig. B.2. In both cases, the chosen reference line is crossed only once. From this we infer that both time-reversal invariant planes are topologically nontrivial with $\mathbb{Z}_2$ invariants $\nu = 1$.

C Iterative scheme for the calculation of surface Green's functions

The calculation of the surface JDOS of a lattice system, as in Sec. 5.2.3, requires the computation of the surface Green's function. In the following, an iterative scheme [200] for the computation of this surface Green's function is reviewed. For simplicity,the considerations will be restricted to systems described by tight-binding Hamiltonians with only nearest-neighbor hopping terms. Note, however, that any solid with a surface can be reduced to a semi-infinite stack of principal layers with nearest-neighbor interactions [200].

Let us consider a tight-binding model described by the lattice Hamiltonian $\mathcal{H}$. A surface can be introduced by cleaving the lattice along a principal layer of unit cells. Each unit cell in this layer may have M degrees of freedom, such as spin, orbital or sublattice degrees of freedom. Let us further assume that the system preserves translational symmetry parallel to the surface. Consequently, the momentum $\mathbf{k}_{||}$ parallel to the surface is a good quantum number and we can form Bloch-state vectors for each principal layer of the form

$$\Psi_n(\mathbf{k}_{||}) = [\varphi_n^1(\mathbf{k}_{||}), \ldots, \varphi_n^M(\mathbf{k}_{||})], \tag{C.1}$$

where n labels the layer. By taking matrix elements of the operator equation $(\omega - \mathcal{H})\mathcal{G}(\omega) = \mathcal{I}$ with the Bloch states, we get the following chain of coupled equations for each $\mathbf{k}_{||}$

$$\begin{aligned}
(\omega - H_{00})G_{00} &= \mathbb{1} + H_{01}G_{10} && \text{(C.2)}\\
(\omega - H_{00})G_{10} &= H_{01}^\dagger G_{00} + H_{01}G_{20} && \text{(C.3)}\\
&\vdots \\
(\omega - H_{00})G_{n0} &= H_{01}^\dagger G_{n-1,0} + H_{01}G_{n+1,0}, && \text{(C.4)}
\end{aligned}$$

where the H_{nm} and G_{nm} are $M \times M$ matrices defined as

$$\begin{aligned} H_{nm}(\mathbf{k}_{||}) &= \langle \Psi_n(\mathbf{k}_{||}) | \mathcal{H} | \Psi_m(\mathbf{k}_{||}) \rangle, && \text{(C.5)} \\ G_{nm}(\omega, \mathbf{k}_{||}) &= \langle \Psi_n(\mathbf{k}_{||}) | \mathcal{G}(\omega) | \Psi_m(\mathbf{k}_{||}) \rangle, && \text{(C.6)} \end{aligned}$$

and we have assumed an ideal surface with $H_{00} = H_{11} = \ldots = H_{nn}$ and $H_{01} = H_{12} = \ldots = H_{n-1,n}$. Note that $n = 0$ corresponds to the surface principal layer. Hence, $G_{00}(\omega, \mathbf{k}_{||})$ defines the surface Green's function.

The general equation for G_{n0} in Eq. (C.4) can be rewritten as ($n \geq 1$)

$$G_{n0}(\omega) = (\omega - H_{00})^{-1}(H_{01}^{\dagger} G_{n-1,0} + H_{01} G_{n+1,0}). \tag{C.7}$$

If we put $n = 1$ in this equation and plug it into Eq. (C.2) we get

$$[\omega - H_{00} - H_{01}(\omega - H_{00})^{-1} H_{01}^{\dagger}] G_{00} = \mathbb{1} + H_{01}(\omega - H_{00})^{-1} H_{01} G_{20}. \tag{C.8}$$

Similarly, we can replace $G_{n-1,0}$ and $G_{n+1,0}$ in Eq. (C.4) by replacing $n \to n-1$ and $n \to n+1$, respectively. The ensuing equations can be written more compactly as ($n \geq 2$)

$$\begin{aligned} (\omega - \epsilon_{1s}) G_{00} &= \mathbb{1} + \alpha_1 G_{20} && \text{(C.9)} \\ (\omega - \epsilon_1) G_{n0} &= \beta_1 G_{n-2,0} + \alpha_1 G_{n+2,0} && \text{(C.10)} \end{aligned}$$

with

$$\begin{aligned} \alpha_1 &= H_{01}(\omega - H_{00})^{-1} H_{01} && \text{(C.11)} \\ \beta_1 &= H_{01}^{\dagger}(\omega - H_{00})^{-1} H_{01}^{\dagger} && \text{(C.12)} \\ \epsilon_{1s} &= H_{00} + H_{01}(\omega - H_{00})^{-1} H_{01}^{\dagger} && \text{(C.13)} \\ \epsilon_1 &= H_{00} + H_{01}(\omega - H_{00})^{-1} H_{01}^{\dagger} \\ &\quad + H_{01}^{\dagger}(\omega - H_{00})^{-1} H_{01}. && \text{(C.14)} \end{aligned}$$

These equations only involve next-nearest-neighbor Green's functions, whereas nearest neighbors have disappeared completely.

Let us now consider the subset of equations formed by taking only even values for n, namely

$$\begin{aligned}(\omega - \epsilon_{1s})G_{00} &= \mathbb{1} + \alpha_1 G_{20} && \text{(C.15)}\\ (\omega - \epsilon_1)G_{20} &= \beta_1 G_{00} + \alpha_1 G_{40} && \text{(C.16)}\\ &\vdots \\ (\omega - \epsilon_1)G_{2n,0} &= \beta_1 G_{2(n-1),0} + \alpha_1 G_{2(n+1),0}. && \text{(C.17)}\end{aligned}$$

This set of equations is isomorphic to Eqs. (C.2)–(C.4) except for the different zeroth-order matrix elements, $\epsilon_{1s} \neq \epsilon_1$. Thus, we can reiterate the same steps to obtain α_2, β_2, ϵ_2 and ϵ_{2s}. Starting with $\epsilon_0 = \epsilon_{0s} = H_{00}$, $\alpha_0 = H_{01}$ and $\beta_0 = H_{01}^\dagger$, this defines an iterative sequence in which after the i-th step the system of equations reads

$$\begin{aligned}(\omega - \epsilon_{is})G_{00} &= \mathbb{1} + \alpha_i G_{2^i,0} && \text{(C.18)}\\ (\omega - \epsilon_i)G_{2^i,0} &= \beta_i G_{00} + \alpha_1 G_{2^{i+1},0} && \text{(C.19)}\\ &\vdots \\ (\omega - \epsilon_i)G_{2^i n,0} &= \beta_i G_{2^i(n-1),0} + \alpha_i G_{2^i(n+1),0} && \text{(C.20)}\end{aligned}$$

with

$$\begin{aligned}\alpha_i &= \alpha_{i-1}(\omega - \epsilon_{i-1})^{-1}\alpha_{i-1} && \text{(C.21)}\\ \beta_i &= \beta_{i-1}(\omega - \epsilon_{i-1})^{-1}\beta_{i-1} && \text{(C.22)}\\ \epsilon_i &= \epsilon_{i-1} + \alpha_{i-1}(\omega - \epsilon_{i-1})^{-1}\beta_{i-1} \\ &\quad + \beta_{i-1}(\omega - \epsilon_{i-1})^{-1}\alpha_{i-1} && \text{(C.23)}\\ \epsilon_{is} &= \epsilon_{i-1,s} + \alpha_{i-1}(\omega - \epsilon_{i-1})^{-1}\beta_{i-1}. && \text{(C.24)}\end{aligned}$$

After the i-th step, this set of equations describes an effective Hamiltonian for a chain with a unit cell enlarged by a factor of 2^i, with nearest-neighbor interactions α_i and β_i, and with zeroth-order Hamiltonian matrix elements ϵ_i and ϵ_{is}. In each layer of this effective chain the effects of nearest-neighbor interactions of all the previous chains are implicitly encoded. The norm of the α's and β's typically decreases with i. Once they are small enough, we have $\epsilon_i \simeq \epsilon_{i-1}$ and $\epsilon_{is} \simeq \epsilon_{i-1,s}$. In particular, the right-hand side of Eq. (C.18) becomes $\simeq \mathbb{1}$ and we can finally solve for the surface Green's function,

$$G_S \equiv G_{00}(\omega) \simeq (\omega - \epsilon_{is})^{-1}. \tag{C.25}$$

Thus, we have obtained a good approximation for G_{00}. The Green's function of the dual (or opposite) surface can be obtained be exchanging the role of α_i and β_i. In practice, one usually wishes to determine the retarded or advanced Green's function. For that, one simply replaces ω by $\omega \mp i\eta$, with $\eta \in \mathbb{R}$ sufficiently small, in the iterative scheme.

The great advantage of this scheme is its fast convergence. Typically, one achieves $\beta_i \simeq 0$, $\alpha_i \simeq 0$ to numerical accuracy in fewer than 10 iterations.

List of publications

7. **Synthesizing Weyl semimetals in weak topological insulator and topological crystalline insulator multilayers**
   A. Lau, and C. Ortix
   Physical Review B **96**, 081411(R) (2017)

   Abstract: We propose a different route to time-reversal invariant Weyl semimetals employing multilayer heterostructures comprising ordinary "trivial" insulators and nontrivial insulators with *pairs* of protected Dirac cones on the surface. We consider both the case of weak topological insulators, where surface Dirac cones are pinned to time-reversal invariant momenta, and of topological crystalline insulators with unpinned surface Dirac cones. For both realizations we explain phenomenologically how the proposed construction leads to the emergence of a Weyl semimetal phase. We further formulate effective low-energy models for which we prove the existence of semimetallic phases with four isolated Weyl points. Finally, we discuss how the proposed design can be realized experimentally with state-of-the-art technologies.

   A large part of this publication has been included in Chapter 5 of this dissertation.

6. **Generic coexistence of Fermi arcs and Dirac cones on the surface of time-reversal invariant Weyl semimetals**
   A. Lau, K. Koepernik, J. van den Brink, and C. Ortix
   Physical Review Letters **119**, 076801 (2017)

   Abstract: The hallmark of Weyl semimetals is the existence of open constant-energy contours on their surface – the so-called Fermi arcs – connecting Weyl points. Here, we show that for time-reversal symmetric realizations of Weyl semimetals these Fermi arcs in many cases coexist with closed Fermi pockets originating from surface Dirac cones pinned to time-reversal invariant momenta. The existence of Fermi pockets is required for certain Fermi-arc connectivities due to additional restrictions imposed by the six $\mathbb{Z}_2$ topological invariants characterizing a generic time-reversal invariant Weyl semimetal. We show that a change of the Fermi-arc connectivity generally leads to a different topology of the surface Fermi surface, and identify the half-Heusler compound LaPtBi under in-plane compressive strain as a material that realizes this surface Lifshitz transition. We also discuss universal features of this coexistence in quasi-particle interference spectra.

A large part of this publication has been included in Chapter 5 of this dissertation.

5. **Topological mirror insulators in one dimension**
   A. Lau, J. van den Brink, and C. Ortix
   Physical Review B **94**, 165164 (2016)

   Abstract: We demonstrate the existence of topological insulators in one dimension protected by mirror and time-reversal symmetries. They are characterized by a nontrivial $\mathbb{Z}_2$ topological invariant defined in terms of the "partial" polarizations, which we show to be quantized in presence of a one-dimensional mirror point. The topological invariant determines the generic presence or absence of integer boundary charges at the mirror-symmetric boundaries of the system. We check our findings against spin-orbit coupled Aubry-André-Harper models that can be realized, e.g., in cold-atomic Fermi gases loaded in one-dimensional optical lattices or in density- and Rashba spin-orbit-modulated semiconductor nanowires. In this setup, in-gap end-mode Kramers doublets appearing in the topologically non-trivial state effectively constitute a double-quantum-dot with spin-orbit coupling.

   A large part of this publication has been included in Chapter 4 of this dissertation.

4. **Topological edge states with zero Hall conductivity in a dimerized Hofstadter model**
   A. Lau, C. Ortix, and J. van den Brink
   Physical Review Letters **115**, 216805 (2015)

   Abstract: The Hofstadter model is a simple yet powerful Hamiltonian to study quantum Hall physics in a lattice system, manifesting its essential topological states. Lattice dimerization in the Hofstadter model opens an energy gap at half-filling. Here we show that even if the ensuing insulator has a Chern number equal to *zero*, concomitantly a doublet of edge states appear that are pinned at specific momenta. We demonstrate that these states are topologically protected by inversion symmetry in specific one-dimensional cuts in momentum space, define and calculate the corresponding invariants and identify a platform for the experimental detection of these novel topological states.

A large part of this publication has been included in Chapter 2 of this dissertation.

3. **One-dimensional Dirac electrons on the surface of weak topological insulators**
   A. Lau, C. Ortix, and J. van den Brink
   Physical Review B **91**, 085106 (2015)

   Abstract: We show that a class of weak three-dimensional topological insulators feature one-dimensional Dirac electrons on their surfaces. Their hallmark is a line-like energy dispersion along certain directions of the surface Brillouin zone. These one-dimensional Dirac line degeneracies are topologically protected by a symmetry that we refer to as *in-plane time-reversal invariance.* We show how this invariance leads to Dirac lines in the surface spectrum of stacked Kane-Mele systems and more general models for weak three-dimensional topological insulators.

   A large part of this publication has been included in Chapter 3 of this dissertation.

2. **Topological surface states and Andreev bound states in superconducting iron pnictides**
   A. Lau, and C. Timm
   Physical Review B **90**, 024517 (2014)

   Abstract: The nontrivial topology of the electronic structure of iron pnictides can lead to the appearance of surface states. We study such states in various strip geometries with a focus on the superconducting phase. In the presence of unconventional superconducting pairing with $s_{\pm}$-wave gap structure, the topological states are quite robust and partly remain in the superconducting gap. Furthermore, Andreev bound states appear, which coexist with the topological states for small superconducting gaps and merge with them for larger gap values. The bulk and surface dispersions are obtained from exact diagonalization for two-orbital and five-orbital models in strip geometries.

   This publication has not been included in this dissertation.

1. **Topological surface states in paramagnetic and antiferromagnetic iron pnictides**
   A. Lau, and C. Timm
   Physical Review B **88**, 165402 (2013)

Abstract: The electronic structure of iron pnictides is topologically nontrivial, leading to the appearance of Dirac cones in the band structure for the antiferromagnetic phase. Motivated by the analogy with Dirac cones in graphene, we explore the possible existence of topologically protected surface states. Surprisingly, bands of surface states exist even in the paramagnetic state. A realistic five-orbital model predicts two such bands. In the antiferromagnetic phase, these surface bands survive but split. We obtain the bulk and surface dispersion from exact diagonalization of two- and five-orbital models in a strip geometry and discuss the results based on topology.

This publication has not been included in this dissertation.

Bibliography

[1] K. v. Klitzing, G. Dorda, and M. Pepper, *New method for high-accuracy determination of the fine-structure constant based on quantized Hall resistance*, Phys. Rev. Lett. **45**, 494 (1980).

[2] J. E. Moore, *The birth of topological insulators*, Nature **464**, 194 (2010).

[3] M. Z. Hasan and C. L. Kane, *Colloquium: Topological insulators*, Rev. Mod. Phys. **82**, 3045 (2010).

[4] X.-L. Qi and S.-C. Zhang, *Topological insulators and superconductors*, Rev. Mod. Phys. **83**, 1057 (2011).

[5] E. H. Hall, *On a new action of the magnet on electric currents*, Am. J. Math. **2**, 287 (1879).

[6] A. Bohm *et al.*, *The geometric phase in quantum systems*, *Texts and monographs in physics* (Springer, Berlin, 2003).

[7] J. Singleton, *Band theory and electronic properties of solids*, *Oxford Master Series in Condensed Matter Physics* (OUP Oxford, Oxford, 2001).

[8] K. He, Y. Wang, and Q.-K. Xue, *Quantum anomalous Hall effect*, National Science Review **1**, 38 (2013).

[9] D. C. Tsui, H. L. Stormer, and A. C. Gossard, *Two-dimensional magnetotransport in the extreme quantum limit*, Phys. Rev. Lett. **48**, 1559 (1982).

[10] S. C. Zhang, *The Chern-Simons-Landau-Ginzburg theory of the fractional quantum Hall effect*, Int. J. Mod. Phys. B **06**, 803 (1992).

[11] A. Stern, *Anyons and the quantum Hall effect: A pedagogical review*, Ann. Phys. **323**, 204 (2008).

[12] Note set: *"Avanced Quantum Mechanics 2"* by Niels Walet, `http://oer.physics.manchester.ac.uk/AQM2/Notes/Notes-4.4.html`, accessed: 2017-05-25.

[13] A. H. C. Neto *et al.*, *The electronic properties of graphene*, Rev. Mod. Phys. **81**, 109 (2009).

[14] D. J. Thouless, M. Kohmoto, M. P. Nightingale, and M. den Nijs, *Quantized Hall conductance in a two-dimensional periodic potential*, Phys. Rev. Lett. **49**, 405 (1982).

[15] M. Kohmoto, *Topological invariant and the quantization of the Hall conductance*, Ann. Phys. **160**, 343 (1985).

[16] B. Bernevig and T. Hughes, *Topological insulators and topological superconductors* (Princeton University Press, Princeton, 2013).

[17] R. B. Laughlin, *Quantized Hall conductivity in two dimensions*, Phys. Rev. B **23**, 5632 (1981).

[18] B. I. Halperin, *Quantized Hall conductance, current-carrying edge states, and the existence of extended states in a two-dimensional disordered potential*, Phys. Rev. B **25**, 2185 (1982).

[19] K. S. Novoselov *et al.*, *Room-temperature quantum Hall effect in graphene*, Science **315**, 1379 (2007).

[20] F. D. Parmentier *et al.*, *Quantum Hall effect in epitaxial graphene with permanent magnets*, Sci. Rep. **6**, 38393 (2016).

[21] F. D. M. Haldane, *Model for a quantum Hall effect without Landau levels: Condensed-matter realization of the parity anomaly*, Phys. Rev. Lett. **61**, 2015 (1988).

[22] X.-L. Qi, T. L. Hughes, and S.-C. Zhang, *Topological field theory of time-reversal invariant insulators*, Phys. Rev. B **78**, 195424 (2008).

[23] R. Yu *et al.*, *Quantized anomalous Hall effect in magnetic topological insulators*, Science **329**, 61 (2010).

[24] C.-Z. Chang *et al.*, *Experimental observation of the quantum anomalous Hall effect in a magnetic topological insulator*, Science **340**, 167 (2013).

[25] M. Nakahara, *Geometry, topology and physics*, *Graduate student series in physics* (Hilger, Bristol, 1990).

[26] A. Kitaev, V. Lebedev, and M. Feigel'man, *Periodic table for topological insulators and superconductors*, AIP Conference Proceedings **1134**, 22 (2009).

[27] A. P. Schnyder *et al.*, *Classification of topological insulators and superconductors*, AIP Conference Proceedings **1134**, 10 (2009).

[28] A. W. W. Ludwig, *Topological phases: Classification of topological insulators and superconductors of non-interacting fermions, and beyond*, Phys. Scripta **T168**, 014001 (2015).

[29] T. Fukui, Y. Hatsugai, and H. Suzuki, *Chern numbers in discretized Brillouin zone: Efficient method of computing (spin) Hall conductances*, J. Phys. Soc. Jpn. **74**, 1674 (2005).

[30] M. R. Zirnbauer, *Riemannian symmetric superspaces and their origin in random-matrix theory*, J. Math. Phys. **37**, 4986 (1996).

[31] A. Altland and M. R. Zirnbauer, *Nonstandard symmetry classes in mesoscopic normal-superconducting hybrid structures*, Phys. Rev. B **55**, 1142 (1997).

[32] P. Heinzner, A. Huckleberry, and M. R. Zirnbauer, *Symmetry classes of disordered fermions*, Commun. Math. Phys **257**, 725 (2005).

[33] A. P. Schnyder, S. Ryu, A. Furusaki, and A. W. W. Ludwig, *Classification of topological insulators and superconductors in three spatial dimensions*, Phys. Rev. B **78**, 195125 (2008).

[34] S. Ryu, A. P. Schnyder, A. Furusaki, and A. W. W. Ludwig, *Topological insulators and superconductors: Tenfold way and dimensional hierarchy*, New J. Phys. **12**, 065010 (2010).

[35] R. Kates and F. Schwabl, *Quantum mechanics*, *Advanced Texts in Physics* (Springer Berlin Heidelberg, Berlin, 2013).

[36] D. R. Hofstadter, *Energy levels and wave functions of Bloch electrons in rational and irrational magnetic fields*, Phys. Rev. B **14**, 2239 (1976).

[37] D. Weiss, *Solid-state physics: The butterfly emerges*, Nat. Phys. **9**, 395 (2013).

[38] D. Osadchy and J. E. Avron, *Hofstadter butterfly as quantum phase diagram*, J. Math. Phys. **42**, 5665 (2001).

[39] A. Lau, C. Ortix, and J. van den Brink, *Topological edge states with zero Hall conductivity in a dimerized Hofstadter model*, Phys. Rev. Lett. **115**, 216805 (2015).

[40] L. Fu and C. L. Kane, *Topological insulators with inversion symmetry*, Phys. Rev. B **76**, 045302 (2007).

[41] P. Marra, R. Citro, and C. Ortix, *Fractional quantization of the topological charge pumping in a one-dimensional superlattice*, Phys. Rev. B **91**, 125411 (2015).

[42] L.-J. Lang, X. Cai, and S. Chen, *Edge states and topological phases in one-dimensional optical superlattices*, Phys. Rev. Lett. **108**, 220401 (2012).

[43] S. Ganeshan, K. Sun, and S. Das Sarma, *Topological zero-energy modes in gapless commensurate Aubry-André-Harper models*, Phys. Rev. Lett. **110**, 180403 (2013).

[44] Y. E. Kraus and O. Zilberberg, *Topological equivalence between the Fibonacci quasicrystal and the Harper model*, Phys. Rev. Lett. **109**, 116404 (2012).

[45] A. Y. Kitaev, *Unpaired Majorana fermions in quantum wires*, Phys. Usp. **44**, 131 (2001).

[46] W. P. Su, J. R. Schrieffer, and A. J. Heeger, *Solitons in polyacetylene*, Phys. Rev. Lett. **42**, 1698 (1979).

[47] Y.-M. Lu and D.-H. Lee, *Inversion symmetry protected topological insulators and superconductors*, arXiv:1403.5558 (2014).

[48] T. L. Hughes, E. Prodan, and B. A. Bernevig, *Inversion-symmetric topological insulators*, Phys. Rev. B **83**, 245132 (2011).

[49] M. J. Rice and E. J. Mele, *Elementary excitations of a linearly conjugated diatomic polymer*, Phys. Rev. Lett. **49**, 1455 (1982).

[50] M. Ezawa, Y. Tanaka, and N. Nagaosa, *Topological phase transition without gap closing*, Sci. Rep. **42**, 2790 (2013).

[51] L. A. Ponomarenko *et al.*, *Cloning of Dirac fermions in graphene superlattices*, Nature **497**, 594 (2013).

[52] C. R. Dean *et al.*, *Hofstadter's butterfly and the fractal quantum Hall effect in moiré superlattices*, Nature **497**, 598 (2013).

[53] B. Hunt *et al.*, *Massive Dirac fermions and Hofstadter butterfly in a van der Waals heterostructure*, Science **340**, 1427 (2013).

[54] I. Bloch, *Ultracold quantum gases in optical lattices*, Nat. Phys. **1**, 23 (2005).

[55] I. Bloch, J. Dalibard, and S. Nascimbene, *Quantum simulations with ultracold quantum gases*, Nat. Phys. **8**, 267 (2012).

[56] N. Goldman, J. C. Budich, and P. Zoller, *Topological quantum matter with ultracold gases in optical lattices*, Nat. Phys. **12**, 639 (2016).

[57] V. Galitski and I. B. Spielman, *Spin-orbit coupling in quantum gases*, Nature **494**, 49 (2013).

[58] H. Zhai, *Degenerate quantum gases with spin-orbit coupling: A review*, Rep. Prog. Phys. **78**, 026001 (2015).

[59] M. Aidelsburger *et al.*, *Realization of the Hofstadter Hamiltonian with ultracold atoms in optical lattices*, Phys. Rev. Lett. **111**, 185301 (2013).

[60] H. Miyake *et al.*, *Realizing the Harper Hamiltonian with laser-assisted tunneling in optical lattices*, Phys. Rev. Lett. **111**, 185302 (2013).

[61] M. Aidelsburger *et al.*, *Measuring the Chern number of Hofstadter bands with ultracold bosonic atoms*, Nat. Phys. **11**, 162 (2015).

[62] Y. Lahini *et al.*, *Observation of a localization transition in quasiperiodic photonic lattices*, Phys. Rev. Lett. **103**, 013901 (2009).

[63] Y. E. Kraus *et al.*, *Topological states and adiabatic pumping in quasicrystals*, Phys. Rev. Lett. **109**, 106402 (2012).

[64] V. Giovannetti, S. Lloyd, and L. Maccone, *Advances in quantum metrology*, Nat. Photon. **5**, 222 (2011).

[65] K. v. Klitzing, *Physics and application of the quantum Hall effect*, Physica B **204**, 111 (1995).

[66] B. Jeckelmann and B. Jeanneret, *The quantum Hall effect as an electrical resistance standard*, Rep. Prog. Phys. **64**, 1603 (2001).

[67] J. E. Moore and L. Balents, *Topological invariants of time-reversal-invariant band structures*, Phys. Rev. B **75**, 121306 (2007).

[68] S. Murakami, N. Nagaosa, and S.-C. Zhang, *Dissipationless quantum spin current at room temperature*, Science **301**, 1348 (2003).

[69] B. A. Bernevig and S.-C. Zhang, *Quantum spin Hall effect*, Phys. Rev. Lett. **96**, 106802 (2006).

[70] D. N. Sheng, Z. Y. Weng, L. Sheng, and F. D. M. Haldane, *Quantum spin-Hall effect and topologically invariant Chern numbers*, Phys. Rev. Lett. **97**, 036808 (2006).

[71] B. A. Bernevig, T. L. Hughes, and S.-C. Zhang, *Quantum spin Hall effect and topological phase transition in HgTe quantum wells*, Science **314**, 1757 (2006).

[72] M. König *et al.*, *Quantum spin Hall insulator state in HgTe quantum wells*, Science **318**, 766 (2007).

[73] T. Fukui and Y. Hatsugai, *Topological aspects of the quantum spin-Hall effect in graphene: $\mathbb{Z}_2$ topological order and spin Chern number*, Phys. Rev. B **75**, 121403 (2007).

[74] C. L. Kane and E. J. Mele, *$\mathbb{Z}_2$ topological order and the quantum spin Hall effect*, Phys. Rev. Lett. **95**, 146802 (2005).

[75] L. Fu and C. L. Kane, *Time reversal polarization and a $\mathbb{Z}_2$ adiabatic spin pump*, Phys. Rev. B **74**, 195312 (2006).

[76] C. L. Kane and E. J. Mele, *Quantum spin Hall effect in graphene*, Phys. Rev. Lett. **95**, 226801 (2005).

[77] Y. Yao *et al.*, *Spin-orbit gap of graphene: First-principles calculations*, Phys. Rev. B **75**, 041401 (2007).

[78] P. Vogt *et al.*, *Silicene: Compelling experimental evidence for graphenelike two-dimensional silicon*, Phys. Rev. Lett. **108**, 155501 (2012).

[79] M. E. Dávila *et al.*, *Germanene: a novel two-dimensional germanium allotrope akin to graphene and silicene*, New J. Phys. **16**, 095002 (2014).

[80] F. feng Zhu *et al.*, *Epitaxial growth of two-dimensional stanene*, Nat. Mater. **14**, 1020 (2015).

[81] A. Acun *et al.*, *Germanene: the germanium analogue of graphene*, J. Phys. Condens. Matter **27**, 443002 (2015).

[82] M. Ezawa, *Monolayer topological insulators: Silicene, germanene, and stanene*, J. Phys. Soc. Jpn. **84**, 121003 (2015).

[83] Y. Xu *et al.*, *Large-gap quantum spin Hall insulators in tin films*, Phys. Rev. Lett. **111**, 136804 (2013).

[84] L. Fu, C. L. Kane, and E. J. Mele, *Topological insulators in three dimensions*, Phys. Rev. Lett. **98**, 106803 (2007).

[85] R. Roy, *Topological phases and the quantum spin Hall effect in three dimensions*, Phys. Rev. B **79**, 195322 (2009).

[86] M. Hasan, *Berry's phase and quantization in topological insulators*, Physics **3**, 62 (2010).

[87] H. Nielsen and M. Ninomiya, *Absence of neutrinos on a lattice: (I). Proof by homotopy theory*, Nucl. Phys. B **185**, 20 (1981).

[88] H. Nielsen and M. Ninomiya, *Absence of neutrinos on a lattice: (II). Intuitive topological proof*, Nucl. Phys. B **193**, 173 (1981).

[89] F. S. Nogueira, Z. Nussinov, and J. van den Brink, *Josephson currents induced by the Witten effect*, Phys. Rev. Lett. **117**, 167002 (2016).

[90] Y. L. Chen *et al.*, *Experimental realization of a three-dimensional topological insulator,* Bi_2Te_3, Science **325**, 178 (2009).

[91] D. Hsieh *et al.*, *Observation of unconventional quantum spin textures in topological insulators*, Science **323**, 919 (2009).

[92] Y. Xia *et al.*, *Observation of a large-gap topological-insulator class with a single Dirac cone on the surface*, Nat. Phys. **5**, 398 (2009).

[93] Y. Ando, *Topological insulator materials*, J. Phys. Soc. Jpn. **82**, 102001 (2013).

[94] H. Obuse, S. Ryu, A. Furusaki, and C. Mudry, *Spin-directed network model for the surface states of weak three-dimensional $\mathbb{Z}_2$ topological insulators*, Phys. Rev. B **89**, 155315 (2014).

[95] Z. Ringel, Y. E. Kraus, and A. Stern, *Strong side of weak topological insulators*, Phys. Rev. B **86**, 045102 (2012).

[96] T. Morimoto and A. Furusaki, *Stability of surface states of weak $\mathbb{Z}_2$ topological insulators and superconductors*, Phys. Rev. B **89**, 035117 (2014).

[97] B. Rasche *et al.*, *Stacked topological insulator built from bismuth-based graphene sheet analogues*, Nat. Mater. **12**, 422 (2013).

[98] C. Pauly *et al.*, *Subnanometre-wide electron channels protected by topology*, Nat. Phys. **11**, 338 (2015).

[99] M. Eschbach *et al.*, *Bi_1Te_1 is a dual topological insulator*, Nat. Commun. **8**, 14976 (2017).

[100] Q. D. Gibson *et al.*, *Quasi one dimensional Dirac electrons on the surface of Ru_2Sn_3*, Sci. Rep. **4**, 5168 (2014).

[101] C. Fang, Y. Chen, H.-Y. Kee, and L. Fu, *Topological nodal line semimetals with and without spin-orbital coupling*, Phys. Rev. B **92**, 081201 (2015).

[102] C. Fang, H. Weng, X. Dai, and Z. Fang, *Topological nodal line semimetals*, Chin. Phys. B **25**, 117106 (2016).

[103] N. P. Armitage, E. J. Mele, and A. Vishwanath, *Weyl and Dirac semimetals in three dimensional solids*, arXiv:1705.01111 (2017).

[104] A. Lau, C. Ortix, and J. van den Brink, *One-dimensional Dirac electrons on the surface of weak topological insulators*, Phys. Rev. B **91**, 085106 (2015).

[105] L. Cano-Cortés, C. Ortix, and J. van den Brink, *Fundamental differences between quantum spin Hall edge states at zigzag and armchair terminations of honeycomb and ruby nets*, Phys. Rev. Lett. **111**, 146801 (2013).

[106] C.-X. Liu, X.-L. Qi, and S.-C. Zhang, *Half quantum spin Hall effect on the surface of weak topological insulators*, Physica E **44**, 906 (2012).

[107] H. Zhang *et al.*, *Topological insulators in* Bi_2Se_3*,* Bi_2Te_3 *and* Sb_2Te_3 *with a single Dirac cone on the surface*, Nat. Phys. **5**, 438 (2009).

[108] B. Li, Z.-H. Yu, and S.-M. Fei, *Geometry of quantum computation with qutrits*, Sci. Rep. **3**, 2594 (2013).

[109] Private communication with Christian Pauly, coauthor of Ref. [98].

[110] L. Fu, *Topological crystalline insulators*, Phys. Rev. Lett. **106**, 106802 (2011).

[111] Y. Ando and L. Fu, *Topological crystalline insulators and topological superconductors: From concepts to materials*, Annu. Rev. Condens. Matter Phys. **6**, 361 (2015).

[112] T. H. Hsieh *et al.*, *Topological crystalline insulators in the SnTe material class*, Nat. Commun. **3**, 982 (2012).

[113] C.-K. Chiu, H. Yao, and S. Ryu, *Classification of topological insulators and superconductors in the presence of reflection symmetry*, Phys. Rev. B **88**, 075142 (2013).

[114] A. Alexandradinata, C. Fang, M. J. Gilbert, and B. A. Bernevig, *Spin-orbit-free topological insulators without time-reversal symmetry*, Phys. Rev. Lett. **113**, 116403 (2014).

[115] A. Lau, J. van den Brink, and C. Ortix, *Topological mirror insulators in one dimension*, Phys. Rev. B **94**, 165164 (2016).

[116] Z. Wang, A. Alexandradinata, R. J. Cava, and B. A. Bernevig, *Hourglass fermions*, Nature **532**, 189 (2016).

[117] C.-X. Liu, R.-X. Zhang, and B. K. VanLeeuwen, *Topological nonsymmorphic crystalline insulators*, Phys. Rev. B **90**, 085304 (2014).

[118] K. Shiozaki, M. Sato, and K. Gomi, $\mathbb{Z}_2$ *topology in nonsymmorphic crystalline insulators: Möbius twist in surface states*, Phys. Rev. B **91**, 155120 (2015).

[119] K. Shiozaki, M. Sato, and K. Gomi, *Topology of nonsymmorphic crystalline insulators and superconductors*, Phys. Rev. B **93**, 195413 (2016).

[120] R.-J. Slager, A. Mesaros, V. Juričić, and J. Zaanen, *The space group classification of topological band-insulators*, Nat. Phys. **9**, 98 (2012).

[121] J. Kruthoff *et al.*, *Topological classification of crystalline insulators through band structure combinatorics*, arXiv:1612.02007 (2016).

[122] H. C. Po, A. Vishwanath, and H. Watanabe, *Complete theory of symmetry-based indicators of band topology*, Nat. Commun. **8**, 50 (2017).

[123] B. J. Wieder *et al.*, *Wallpaper fermions and the topological Dirac insulator*, arXiv:1705.01617 (2017).

[124] C. Fang, M. J. Gilbert, and B. A. Bernevig, *New class of topological superconductors protected by magnetic group symmetries*, Phys. Rev. Lett. **112**, 106401 (2014).

[125] R.-X. Zhang and C.-X. Liu, *Topological magnetic crystalline insulators and corepresentation theory*, Phys. Rev. B **91**, 115317 (2015).

[126] H. Watanabe, H. C. Po, and A. Vishwanath, *Structure and topology of band structures in the 1651 magnetic space groups*, arXiv:1707.01903 (2017).

[127] J. C. Y. Teo, L. Fu, and C. L. Kane, *Surface states and topological invariants in three-dimensional topological insulators: Application to $Bi_{1-x}Sb_x$*, Phys. Rev. B **78**, 045426 (2008).

[128] K. Shiozaki and M. Sato, *Topology of crystalline insulators and superconductors*, Phys. Rev. B **90**, 165114 (2014).

[129] S. Kettle, *Symmetry and structure* (Wiley, Chichester, 1989).

[130] Y. Tanaka *et al.*, *Experimental realization of a topological crystalline insulator in SnTe*, Nat. Phys. **8**, 800 (2012).

[131] J. Zak, *Berry's phase for energy bands in solids*, Phys. Rev. Lett. **62**, 2747 (1989).

[132] R. D. King-Smith and D. Vanderbilt, *Theory of polarization of crystalline solids*, Phys. Rev. B **47**, 1651 (1993).

[133] R. Resta, *Macroscopic polarization in crystalline dielectrics: The geometric phase approach*, Rev. Mod. Phys. **66**, 899 (1994).

[134] R. Resta, *Manifestations of Berry's phase in molecules and condensed matter*, J. Phys. Condens. Matter **12**, R107 (2000).

[135] P. G. Harper, *Single band motion of conduction electrons in a uniform magnetic field*, Proc. Phys. Soc. London, Sec. A **68**, 874 (1955).

[136] S. Aubry and G. André, Ann. Isr. Phys. Soc. **3**, 133 (1980).

[137] L. W. Cheuk *et al.*, *Spin-injection spectroscopy of a spin-orbit coupled Fermi gas*, Phys. Rev. Lett. **109**, 095302 (2012).

[138] P. Wang *et al.*, *Spin-orbit coupled degenerate Fermi gases*, Phys. Rev. Lett. **109**, 095301 (2012).

[139] M. Mancini *et al.*, *Observation of chiral edge states with neutral fermions in synthetic Hall ribbons*, Science **349**, 1510 (2015).

[140] M. Leder *et al.*, *Real-space imaging of a topologically protected edge state with ultracold atoms in an amplitude-chirped optical lattice*, Nat. Commun. **7**, 13112 (2016).

[141] X.-J. Liu, Z.-X. Liu, and M. Cheng, *Manipulating topological edge spins in a one-dimensional optical lattice*, Phys. Rev. Lett. **110**, 076401 (2013).

[142] D. L. Campbell, G. Juzeliūnas, and I. B. Spielman, *Realistic Rashba and Dresselhaus spin-orbit coupling for neutral atoms*, Phys. Rev. A **84**, 025602 (2011).

[143] M. L. Wall *et al.*, *Synthetic spin-orbit coupling in an optical lattice clock*, Phys. Rev. Lett. **116**, 035301 (2016).

[144] D. Cocks *et al.*, *Time-reversal-invariant Hofstadter-Hubbard model with ultracold fermions*, Phys. Rev. Lett. **109**, 205303 (2012).

[145] P. P. Orth *et al.*, *Correlated topological phases and exotic magnetism with ultracold fermions*, J. Phys. B **46**, 134004 (2013).

[146] J.-H. Park *et al.*, *Fractional boundary charges in quantum dot arrays with density modulation*, Phys. Rev. B **94**, 075416 (2016).

[147] S. Pandey and C. Ortix, *Topological end states due to inhomogeneous strains in wrinkled semiconducting ribbons*, Phys. Rev. B **93**, 195420 (2016).

[148] S. Nadj-Perge, S. M. Frolov, E. P. A. M. Bakkers, and L. P. Kouwenhoven, *Spin-orbit qubit in a semiconductor nanowire*, Nature **468**, 1084 (2010).

[149] R. Li and J. Q. You, *Anisotropic exchange coupling in a nanowire double quantum dot with strong spin-orbit coupling*, Phys. Rev. B **90**, 035303 (2014).

[150] A. A. Burkov, *Topological semimetals*, Nat. Mater. **15**, 1145 (2016).

[151] P. A. M. Dirac, *The quantum theory of the electron*, Proc. R. Soc. A **117**, 610 (1928).

[152] E. Majorana, *Teoria simmetrica dell'elettrone e del positrone*, Il Nuovo Cimento (1924-1942) **14**, 171 (2008).

[153] H. Weyl, *Gravitation and the electron*, Proc. Natl. Acad. Sci. USA **15**, 323 (1929).

[154] L. M. Brown, *The idea of the neutrino*, Phys. Today **31**, 23 (1978).

[155] C. L. Cowan *et al.*, *Detection of the free neutrino: A confirmation*, Science **124**, 103 (1956).

[156] T. Kajita, *Nobel lecture: Discovery of atmospheric neutrino oscillations*, Rev. Mod. Phys. **88**, 030501 (2016).

[157] A. B. McDonald, *Nobel lecture: The Sudbury neutrino observatory: Observation of flavor change for solar neutrinos*, Rev. Mod. Phys. **88**, 030502 (2016).

[158] X. Wan, A. M. Turner, A. Vishwanath, and S. Y. Savrasov, *Topological semimetal and Fermi-arc surface states in the electronic structure of pyrochlore iridates*, Phys. Rev. B **83**, 205101 (2011).

[159] A. A. Burkov and L. Balents, *Weyl semimetal in a topological insulator multilayer*, Phys. Rev. Lett. **107**, 127205 (2011).

[160] A. A. Zyuzin, S. Wu, and A. A. Burkov, *Weyl semimetal with broken time reversal and inversion symmetries*, Phys. Rev. B **85**, 165110 (2012).

[161] T. Ojanen, *Helical Fermi arcs and surface states in time-reversal invariant Weyl semimetals*, Phys. Rev. B **87**, 245112 (2013).

[162] A. A. Soluyanov *et al.*, *Type-II Weyl semimetals*, Nature **527**, 495 (2015).

[163] R. Okugawa and S. Murakami, *Dispersion of Fermi arcs in Weyl semimetals and their evolutions to Dirac cones*, Phys. Rev. B **89**, 235315 (2014).

[164] E. Witten, *Three lectures on topological phases of matter*, La Rivista del Nuovo Cimento **39**, 313 (2016).

[165] J. von Neumann and E. Wigner, *Über das Verhalten von Eigenwerten bei adiabatischen Prozessen*, Phys. Z. **30**, 467 (1929).

[166] Z. Wang *et al.*, *Time-reversal-breaking Weyl fermions in magnetic Heusler alloys*, Phys. Rev. Lett. **117**, 236401 (2016).

[167] S.-M. Huang *et al.*, *A Weyl fermion semimetal with surface Fermi arcs in the transition metal monopnictide TaAs class*, Nat. Commun. **6**, 7373 (2015).

[168] H. Weng *et al.*, *Weyl semimetal phase in noncentrosymmetric transition-metal monophosphides*, Phys. Rev. X **5**, 011029 (2015).

[169] B. Q. Lv *et al.*, *Experimental discovery of Weyl semimetal TaAs*, Phys. Rev. X **5**, 031013 (2015).

[170] B. Q. Lv *et al.*, *Observation of Weyl nodes in TaAs*, Nat. Phys. **11**, 724 (2015).

[171] S.-Y. Xu *et al.*, *Discovery of a Weyl fermion semimetal and topological Fermi arcs*, Science **349**, 613 (2015).

[172] S.-Y. Xu *et al.*, *Discovery of a Weyl fermion state with Fermi arcs in niobium arsenide*, Nat. Phys. **11**, 748 (2015).

[173] N. Xu *et al.*, *Observation of Weyl nodes and Fermi arcs in tantalum phosphide*, Nat. Commun. **7**, 11006 (2016).

[174] Y. Sun *et al.*, *Prediction of Weyl semimetal in orthorhombic* $MoTe_2$, Phys. Rev. B **92**, 161107 (2015).

[175] S. Murakami, *Phase transition between the quantum spin Hall and insulator phases in 3D: Emergence of a topological gapless phase*, New J. Phys. **9**, 356 (2007).

[176] H. Nielsen and M. Ninomiya, *The Adler-Bell-Jackiw anomaly and Weyl fermions in a crystal*, Phys. Lett. B **130**, 389 (1983).

[177] K.-Y. Yang, Y.-M. Lu, and Y. Ran, *Quantum Hall effects in a Weyl semimetal: Possible application in pyrochlore iridates*, Phys. Rev. B **84**, 075129 (2011).

[178] J. Gooth *et al.*, *Experimental signatures of the mixed axial–gravitational anomaly in the Weyl semimetal NbP*, Nature **547**, 324 (2017).

[179] A. G. Grushin, J. W. F. Venderbos, and J. H. Bardarson, *Coexistence of Fermi arcs with two-dimensional gapless Dirac states*, Phys. Rev. B **91**, 121109 (2015).

[180] S. Juergens and B. Trauzettel, *Exotic surface states in hybrid structures of topological insulators and Weyl semimetals*, Phys. Rev. B **95**, 085313 (2017).

[181] A. Lau, K. Koepernik, J. van den Brink, and C. Ortix, *Generic coexistence of Fermi arcs and Dirac cones on the surface of time-reversal invariant Weyl semimetals*, Phys. Rev. Lett. **119**, 076801 (2017).

[182] G. Chang *et al.*, *Kramers theorem-enforced Weyl fermions: Theory and materials predictions (Ag_3BO_3, $TlTe_2O_6$ and Ag_2Se related families)*, arXiv:1611.07925 (2016).

[183] C.-K. Chiu, J. C. Y. Teo, A. P. Schnyder, and S. Ryu, *Classification of topological quantum matter with symmetries*, Rev. Mod. Phys. **88**, 035005 (2016).

[184] G. E. Volovik, *Topological Lifshitz transitions*, Low Temp. Phys. **43**, 47 (2017).

[185] A. Varlet *et al.*, *Tunable Fermi surface topology and Lifshitz transition in bilayer graphene*, arXiv:1508.02922 (2015).

[186] P. G. Derry, A. K. Mitchell, and D. E. Logan, *Quasiparticle interference from magnetic impurities*, Phys. Rev. B **92**, 035126 (2015).

[187] S. Kourtis *et al.*, *Universal signatures of Fermi arcs in quasiparticle interference on the surface of Weyl semimetals*, Phys. Rev. B **93**, 041109 (2016).

[188] G. Chang *et al.*, *Signatures of Fermi arcs in the quasiparticle interferences of the Weyl semimetals TaAs and NbP*, Phys. Rev. Lett. **116**, 066601 (2016).

[189] R. Batabyal *et al.*, *Visualizing weakly bound surface Fermi arcs and their correspondence to bulk Weyl fermions*, Sci. Adv. **2**, e1600709 (2016).

[190] H. Zheng *et al.*, *Atomic-scale visualization of quantum interference on a Weyl semimetal surface by scanning tunneling microscopy*, ACS Nano **10**, 1378 (2016).

[191] L. Simon, F. Vonau, and D. Aubel, *A phenomenological approach of joint density of states for the determination of band structure in the case of a semi-metal studied by FT-STS*, J. Phys. Condens. Matter **19**, 355009 (2007).

[192] J. Ruan *et al.*, *Symmetry-protected ideal Weyl semimetal in HgTe-class materials*, Nat. Commun. **7**, 11136 (2016).

[193] D. Xiao *et al.*, *Half-Heusler compounds as a new class of three-dimensional topological insulators*, Phys. Rev. Lett. **105**, 096404 (2010).

[194] K. Koepernik and H. Eschrig, *Full-potential nonorthogonal local-orbital minimum-basis band-structure scheme*, Phys. Rev. B **59**, 1743 (1999).

[195] A. Lau and C. Ortix, *Synthesizing Weyl semimetals in weak topological insulator and topological crystalline insulator multilayers*, arXiv:1705.08692 (2017).

[196] R. S. K. Mong, J. H. Bardarson, and J. E. Moore, *Quantum transport and two-parameter scaling at the surface of a weak topological insulator*, Phys. Rev. Lett. **108**, 076804 (2012).

[197] R. Yu *et al.*, *Equivalent expression of $\mathbb{Z}_2$ topological invariant for band insulators using the non-Abelian Berry connection*, Phys. Rev. B **84**, 075119 (2011).

[198] G. C. Thiang, K. Sato, and K. Gomi, *Fu-Kane-Mele monopoles in semimetals*, Nucl. Phys. B **923C**, 107 (2017).

[199] J. W. F. Venderbos and L. Fu, *Interacting Dirac fermions under a spatially alternating pseudomagnetic field: Realization of spontaneous quantum Hall effect*, Phys. Rev. B **93**, 195126 (2016).

[200] M. P. L. Sancho, J. M. L. Sancho, and J. Rubio, *Highly convergent schemes for the calculation of bulk and surface Green functions*, J. Phys. F **15**, 851 (1985).

[201] M. Sato and Y. Ando, *Topological superconductors*, arXiv:1608.03395 (2016).

[202] A. P. Schnyder and P. M. R. Brydon, *Topological surface states in nodal superconductors*, J. Phys. Condens. Matter **27**, 243201 (2015).

[203] M. Leijnse and K. Flensberg, *Introduction to topological superconductivity and Majorana fermions*, Semicond. Sci. Technol. **27**, 124003 (2012).

[204] J. Alicea, *New directions in the pursuit of Majorana fermions in solid state systems*, Rep. Prog. Phys. **75**, 076501 (2012).

[205] D. I. Pikulin, C.-K. Chiu, X. Zhu, and M. Franz, *Interaction-enabled topological phases in topological insulator–superconductor heterostructures*, Phys. Rev. B **92**, 075438 (2015).

[206] A. Chen and M. Franz, *Superconducting proximity effect and Majorana flat bands at the surface of a Weyl semimetal*, Phys. Rev. B **93**, 201105 (2016).

[207] V. Mourik *et al.*, *Signatures of Majorana fermions in hybrid superconductor-semiconductor nanowire devices*, Science **336**, 1003 (2012).

[208] P. M. R. Brydon, A. P. Schnyder, and C. Timm, *Helical spin texture of surface states in topological superconductors*, New J. Phys. **17**, 013016 (2015).

[209] R. Queiroz and A. P. Schnyder, *Helical Majorana surface states of strongly disordered topological superconductors with time-reversal symmetry*, Phys. Rev. B **91**, 014202 (2015).

[210] D. Lee and A. P. Schnyder, *Structure of vortex-bound states in spin-singlet chiral superconductors*, Phys. Rev. B **93**, 064522 (2016).

[211] A. M. Turner, F. Pollmann, and E. Berg, *Topological phases of one-dimensional fermions: An entanglement point of view*, Phys. Rev. B **83**, 075102 (2011).

[212] M. Levin and A. Stern, *Fractional topological insulators*, Phys. Rev. Lett. **103**, 196803 (2009).

[213] M. Dzero, J. Xia, V. Galitski, and P. Coleman, *Topological Kondo insulators*, Annu. Rev. Condens. Matter Phys. **7**, 249 (2016).

[214] S. Raghu, X.-L. Qi, C. Honerkamp, and S.-C. Zhang, *Topological Mott insulators*, Phys. Rev. Lett. **100**, 156401 (2008).

[215] A. A. Soluyanov and D. Vanderbilt, *Smooth gauge for topological insulators*, Phys. Rev. B **85**, 115415 (2012).

Acknowledgements

The end of this thesis also represents the end of nine wonderful years in Dresden. This time has been a very influential part of my life and I want to thank all the people who have accompanied me on this way, especially my friends.

I want to express my gratitude to my scientific advisors Prof. Jeroen van den Brink and Dr. Carmine Ortix for giving me the opportunity to work on so many different and interesting topics during my PhD, for giving me the possibility to develop and contribute my own research ideas, for encouraging me to attend and to be involved in summer schools, workshops and conferences, and, most importantly, for their invaluable counsel and support.

Many thanks go to all the members of the Institute for Theoretical Solid State Physics (ITF), who have made my time at the IFW Dresden a most enjoyable one. This includes discussion groups, movie nights, Scotch Fridays, IFW events, summer schools, and, of course, the many lunch and coffee breaks with countless discussions about anything and everything. In particular, I want to thank all my office mates, Dr. Vamshi Katukuri, Nikolay Bogdanov, Katja Pärschke, Andrei Pavlov and Cliò Agrapidis, but also Dr. Frank Kirtschig, Dr. Flavio Nogueira, Dr. Rajyavardhan Ray, and Dr. Cosma Fulga for their nice company and for many fruitful discussions. Special thanks also go to the ITF secretary Grit Rötzer for her patience and help with all bureaucratic matters.

Most importantly, I am deeply grateful to my family, especially to my parents and grandparents, who have always believed in me, who have always supported me and who have always been there for me. Finally, I also express my gratitude to my girlfriend Cliò for her endless patience and support.

Eidesstattliche Erklärung

Hiermit versichere ich, dass ich die vorliegende Arbeit ohne unzulässige Hilfe Dritter und ohne Benutzung anderer als der angegebenen Hilfsmittel angefertigt habe; die aus fremden Quellen direkt oder indirekt übernommenen Gedanken sind als solche kenntlich gemacht. Die Arbeit wurde bisher weder im Inland noch im Ausland in gleicher oder ähnlicher Form einer anderen Prüfungsbehörde vorgelegt.

Die vorliegende Dissertation wurde vom 01.04.2014 bis 17.10.2017 am Leibniz-Institut für Festkörper- und Werkstoffforschung Dresden (IFW Dresden), Institut für theoretische Festkörperphysik (ITF), unter der Betreuung von Prof. Dr. Jeroen van den Brink und Dr. Carmine Ortix angefertigt.

Es haben keine erfolglosen Promotionsverfahren in der Vergangenheit stattgefunden. Die aktuelle Promotionsordnung der Fakultät Mathematik und Naturwissenschaften der Technischen Universität Dresden wird anerkannt.

Alexander Lau
Dresden, 17.10.2017